Presenting a novel higher-order bounded convection scheme for simulation of multiphase flows and convection heat transfer

***International Journal of Heat and Mass Transfer*. Elsevier**

Faroogh Garoosi[*,a], Tew-Fik Mahdi[b]

[a,b]Department of Civil, Geological and Mining Engineering, Polytechnique Montreal, Montreal, Quebec, Canada

Corresponding author: faroogh.garoosi@polymtl.ca

Second author: tewfik.mahdi@polymtl.ca

Abstract

The primary aim of the current study is to enhance the stability and accuracy of the Volume-Of-Fluid (VOF) method for modeling free-surface flows with large topological changes and high density ratio. For accurate capturing of fluid interfaces, a novel higher-order bounded convection scheme is first constructed based on the total variation diminishing (TVD) concept and is then employed for the discretization of convection terms in Navier-Stokes, energy and transport equations. In the second step, the classical PISO algorithm is modified according to the two-step projection method (Chorin's model) and the combined model (PISOC) is then applied for the treatment of the pressure-velocity coupling. Moreover, the second-order accurate piecewise-linear interface reconstruction technique (PLIC-ELVIRA) is used for determining the normal direction and curvature of the interface. The robustness and accuracy of the proposed models in handling multiphase flows with interface rupture and coalescence are verified against several experimental and numerical benchmark solutions such as: dam break, Rayleigh-Taylor instability, bubble rising, rotation of a slotted disk (Zalesak's problem), deformation of a 2D disk and pure convection of a step profile. The results show that, the proposed third-order TVD flux-limiter scheme can considerably reduce the false-diffusion errors and ensure the boundedness of

the volume fraction while retaining the sharpness and shape of the interface. Furthermore, it is found that the proposed PISOC algorithm has strong stability and convergence characteristics in strongly coupled multiphase problems and is less susceptible to divergence when larger pressure under-relaxation factor is used. The performance and effectiveness of the proposed modifications are further demonstrated by analyzing transient entropy generation due to conjugate natural convection heat transfer in two different canonical test cases (i.e. Differentially Heated Cavity and Rayleigh-Bénard Convection) and good agreements are found with previously published works.

Keywords: *Third-order TVD flux-limiter scheme; Improved PISO algorithm; Multiphase flows*; *PLIC;VOF method*; *ELVIRA scheme*

Nomenclature

A	surface area per unit depth $A = 2(L+H)$, m
Be	Bejan number
C_p	specific heat, $J\ kg^{-1}\ K^{-1}$
F_b	Body force
g	Gravitational acceleration, ms^{-2}
h	Smoothing length, m
H	enclosure height, m
k	thermal conductivity, $Wm^{-1}K^{-1}$
L	Length of the enclosure (m)
$\overline{Nu}$	Average Nusselt number on the active walls
p	pressure, Nm^{-2}
P	dimensionless pressure

Pr	Prandtl number ($=\nu_f / \alpha_f$)
r	distance
Ra	Rayleigh number ($=g\beta(T_h - T_c)H^3 / \alpha\nu$)
S	Total entropy generation (W/m^{3}K)
S_F	Entropy generation due to viscous dissipation
S_T	Entropy generation due to heat transfer
t	time (s)
t^*	dimensionless time, ($t\alpha/H^2$)
T	temperature, K
T_0	Bulk temperature, ($\frac{T_h + T_c}{2}$), K
u,v	velocity components, ms^{-1}
U, V	Dimensionless velocity components
x,y	Cartesian coordinates, m
x_{ij}	Distance between particle i and j in x-direction ($x_{ij} = x_j - x_i$)
y_{ij}	Distance between particle i and j in y-direction ($y_{ij} = y_j - y_i$)
X, Y	Dimensionless Cartesian coordinates

Greek symbols

α	thermal diffusivity, m^2s^{-1}
β	Thermal expansion coefficient, K^{-1}
θ	dimensionless temperature
μ	dynamic viscosity, kg m^{-1} s^{-1}
ν	kinematic viscosity, m^{2}s^{-1}
ρ	density, kg m^{-3}
k	curvature of interface
ψ	stream function($=-\int_{Y_0}^{Y} U\partial Y + \psi(X, Y_0)$)

φ Irreversibility ratio ($\frac{\mu T_0 \alpha^2}{kH^2(T_h - T_c)^2}$) or general dependent variable

Subscripts

c cold wall

f fluid

h hot wall

Total (tot) summation over the domain

1. Introduction

The topic of conjugate conduction and natural convection heat transfer in closed enclosures has received considerable scholarly attention in the last decade owing to its wide range of engineering applications, including building insulation, designing nuclear reactor and solar energy collectors, heat exchangers, double pane windows and microelectronic cooling devices [1–4]. It is well-known that, the presence of internal conductive obstacles in the case of buoyancy driven flows causes significant alteration in the flow and heat transfer characteristics of the thermal systems [5]. Over the past decade, extensive effort has been devoted to analyzing and optimizing conjugate natural convection heat transfer inside closed cavities. In a pioneering work, Amine et al. [6] experimentally and numerically investigated flow structure and heat transfer characteristics of natural convection in a parallelepipedic cavity containing several solid blocks and concluded that the number and arrangement of conductive bodies have a significant impact on the flow intensity within the enclosure. Similar observations were reported by Zhang et al. [7], Ren et al. [8], Raji et al. [9] and Garoosi et al. [10,11] who numerically analyzed the influence of the block's fragmentation upon the heat transfer rate and direction of the fluid motion inside the square cavity. They found that the subdivision of the conductive obstacle into

the smaller segments tends to suppress the fluid motion and delay the onset of natural convection. In the same context, Hu et al. [12], Miroshnichenko et al. [13], Selimefendigil et al. [14], Wang et al. [15] and Zargartalebi et al. [16] systematically examined the influences of pertinent parameters such as Prandtl number (*Pr*), Rayleigh number (*Ra*), inclination angles of the enclosure, the relative thermal conductivity and thickness of the solid wall on the flow pattern, temperature distribution and heat transfer rate, for the case of conjugate natural convection in different geometries (square cavity and partitioned horizontal annulus). They showed that, an increase in the wall-to-fluid thermal conductivity ratio leads to an intensification of convective circulation and thereby heat transfer enhancement while thickness of the conductive wall has a minor impact on the average Nusselt number especially at high *Ra*.

Generally, from the applied thermal boundary conditions point of view, natural convection mechanism in closed enclosure can be classified into two different groups: (a) enclosure with differentially heated vertical walls (DHC) [17] where direction of the buoyancy force is perpendicular to temperature gradient, and (b) enclosure with differentially heated horizontal walls where temperature gradient and gravity force are parallel but act in opposite directions (Rayleigh-Bénard convection) [18]. The study of convection heat transfer in the semi concentric annulus such as C-shaped cavity is of great interest among researchers because it involves the combination of two aforementioned groups. Kalidasan et al. [19], Rahimi et al. [20], Makulati et al. [21] and Mliki et al. [22] numerically investigated the hydrodynamic and thermal behavior of Rayleigh-Bénard convection in a two-dimensional C-shaped enclosure. They proved that the onset of Rayleigh Bénard convection strongly depends upon the *Ra* and aspect ratio of the cold obstacle. However, although the first-law analysis of thermodynamic can provide useful information about flow structures and heat distribution within the system, minimizing the total

rate of entropy generation is necessary for maximizing the overall energy efficiency of the thermal systems. The basic concept of Entropy Generation Minimization (EGM) was first introduced by Bejan [23,24] who mathematically demonstrated that irreversibilities due to fluid friction (viscous dissipation) and heat transfer (temperature gradients) are two main sources of entropy generation and exergy loss (destruction of available work) in thermal systems. Al-Rashed et al. [25], Pordanjani et al. [26], Alkanhal et al. [27], Sivaraj et al. [28] and Magherbi et al. [29] applied second law of thermodynamics to investigate the effects of *Ra* on the entropy generation during the natural convection heat transfer inside the square cavity with and without internal heating. They found that as the *Ra* enhances, both average Nusselt number and entropy generation augment, significantly. A comprehensive review of latest efforts on the analysis of entropy generation and natural convection heat transfer within various enclosures can be found in works of Das et al. [30] and Biswal et al. [31].

The principles of convection heat transfer and entropy generation are reasonably well understood and documented, however, modeling the hydrodynamics of multiphase flow with strong discontinuities is another challenging issue faced by the Computational Fluid Dynamic (CFD) community. Since, multiphase flows with moving and deformable interfaces are ubiquitous in various modern engineering technologies with different length scales such as coal gasification in molten slag [32], fluidized beds [33–35], solidification-melt dynamics [36], combustion systems [37], atomization of liquid jets [38–40] and droplet impact [41,42], considerable research efforts have been devoted to developing robust numerical approach for simulation of such flows. Generally, simulation of multiphase flows can be accomplished through two different main frameworks, namely Eulerian and Lagrangian descriptions [43]. To date, most of the successful methods for investigations of multi-fluid and multiphase flows are designed based on Eulerian

mesh-dependent techniques which in turn have their own pros and cons. Among a large variety of numerical approaches in the class of Eulerian description, Volume-of-Fluid (VOF) [44], Level-Set (LS) [45], Front Tracking model [46] and Two-Fluid approach [47] are four top-ranking methods which have been widely used for computation of multiphase flows with moving free surface. Recent applications of the VOF and the level set methods for simulating bubble rising and dam-break flows involving several obstacles can be found in works of Malgarinos et al. [48], Issakhov et al. [49,50] and Gu et al. [51]. Their results demonstrated that, although two aforementioned methods can satisfactorily predict the pressure distribution of gas-liquid two phase flows, excessive growth in the thickness of the interface (or blurring of the free surface) is still one of the main difficulties associated with these models. To overcome this shortcoming, over the last two decades, several researchers have focused on developing a robust and accurate Interface-Sharpening Algorithm for treatment of the material interfaces in immiscible multiphase flows. Regardless of the numerical approach used for simulation, the problem of preserving interface resolution, in general, can be classified into three major groups, namely (I) implementing high resolution differencing schemes for discretization of the convective term [52], (II) artificial compression schemes to suppress the growth of interface thickness [53], and (III) Adaptive Mesh Refinement (AMR) technique to handle large topology changes of the interface [54].

The first class of methods attempts to define a set of rules with trade off precision-boundedness and its use in the simultaneous reduction of numerical diffusion and unphysical oscillations with a rapid, efficient, and cost-effective one-step composite procedure. Pioneering work in this direction was carried out by Leonard [52] through introducing the principle of the Normalized Variable diagram (NVD). He constructed a new higher-order bounded convection scheme to

mitigate false-diffusion errors and suppress spurious oscillations (undershoots or overshoots that leads to non-physical negative value of density) near discontinuities where strong gradients of variables exist. In the light of the aforementioned study, Hill et al. [55], Denner et al. [56], Ling et al. [57], Deng et al. [58] and Das et al. [59] applied different high order monotonicity-preserving schemes such as: CICSAM, Hyper-C, Semi-Implicit Skewness Correction (SISC), MUSCL, HRIC and SMART to maintain the shape and sharpness of the interface in the complex convection dominated problems including those of the rising bubble and melting with natural convection. Their results showed that, implementing high-resolution bounded convective scheme in transport equation plays a crucial role for determining accurate topology features of the surface dynamics in the coalescence and breakup processes. A comprehensive review and comparison of the behavior between eight widely-used oscillation-free convection schemes in a number of benchmark cases can be found in works of Alves et al. [60] and Choi et al. [61]. Referring to the second approach, Heyns et al. [53] introduced the concept of *Artificial Compression Velocity* to remove false-diffusion errors and restrict the thickness of the interface zone to the minimum possible number of computational grids. Pozzetti et al. [62], Cifani et al. [63], Nguyen et al. [64,65], So et al. [66] and Akhlaghi et al. [67] extended former work and combined the anti-diffusion and artificial compression velocity techniques to control the interface layer thickness between the lighter and heavier mediums. They solved an additional partial differential equation for volume fraction field and concluded that the aforementioned technique can considerably prevent blurring and wrinkling of moving interface, thereby reducing excessive numerical dissipation in that area. Another alternative approach to deal with the excessive smearing of interface is to use an Adaptive Mesh Refinement and coarsening (AMR). A local AMR algorithm as a third-principle tool was originally proposed by Berger et al. [54] for

solving hyperbolic systems of conservation laws. This technique was employed later by Hua et al. [68], Tan et al. [69], Ngo et al. [70], and Antepara et al. [71] to further minimize non-physical smearing of the interface in modeling of rising bubble and droplet dynamics. However, the results of Chen et al. [72], Schmidmayer et al. [73] and Li et al. [74] showed that improper management of unnecessary elements in the dynamic grid refinement/coarsening process can remarkably increase computational effort and even jeopardize convergence of non-linear solvers. These findings were also supported by Das et al. [59] and Harvie et al. [75] who stated that embedding higher order differencing schemes (i.e. 5th order WENO) in local AMR technique without precaution can lead to unphysical velocities around the interface and substantial reduction of mass conservation accordingly.

Based on the above literature review, the primary objective of the present study is to enhance the accuracy and stability of Volume-Of-Fluid (VOF) model for simulation of multiphase flows with high density ratios. For this purpose, the third-order accurate flux-limiter function is first constructed based on the TVD constraint and then employed for discretization of the convection terms and transport equation. To enhance the convergence rate and consistency of the iterative solution procedure, the classical PISO algorithm is combined with the two-step projection method (Chorin's model) and the proposed hybrid model (PISOC) is then implemented for the treatment of the pressure-velocity coupling. To preserve a high level of numerical accuracy, the ELVIRA scheme is utilized for estimating the interface normal and curvature. The proposed modifications are validated against several benchmark test cases including dam break, Rayleigh-Taylor instability, bubble rising, rotation of a slotted disk (Zalesak's problem), deformation of a 2D disk, pure convection of a step profile and transient entropy generation due to conjugate natural convection heat transfer in square enclosures.

1. Problem statement and governing equations

Schematic diagram of the physical models considered in this paper along with the corresponding boundary conditions are shown in Fig. 1 where cases 1 to 6 are employed for validation and verification of the proposed models in dealing with the multiphase flow problems, whereas cases 7 and 8 are considered for analysis of transient entropy generation due to conjugate conduction-convection heat transfer in square enclosures filled with air (Pr=0.71). In all cases, the unsteady flow is assumed to be two-dimensional and laminar. The thermo-physical properties of the fluid are taken to be constant except for the density in cases 7 and 8 which varies linearly with the temperature in accordance to the Oberbeck-Boussinesq approximation. The set of governing equations including continuity, momentum, energy and volume fraction for incompressible Newtonian fluids can be written in the following dimensional forms [76,77]:

$$\frac{\partial \rho}{\rho \partial t}+\frac{\partial u}{\partial x}+\frac{\partial v}{\partial y}=0, \tag{1}$$

$$\frac{\partial \rho_m u}{\partial t}+\frac{\partial \rho_m uu}{\partial x}+\frac{\partial \rho_m vu}{\partial y}=-\frac{\partial p}{\partial x}+[\frac{\partial}{\partial x}\mu_m(\frac{\partial u}{\partial x})+\frac{\partial}{\partial y}\mu_m(\frac{\partial u}{\partial y})]+F_{ST} \tag{2}$$

$$\frac{\partial \rho_m v}{\partial t}+\frac{\partial \rho_m uv}{\partial x}+\frac{\partial \rho_m vv}{\partial y}=-\frac{\partial p}{\partial y}+[\frac{\partial}{\partial x}\mu_m(\frac{\partial v}{\partial x})+\frac{\partial}{\partial y}\mu_m(\frac{\partial v}{\partial y})]+F_g+F_{ST} \tag{3}$$

$$\rho C_p(\frac{\partial T}{\partial t}+u\frac{\partial T}{\partial x}+v\frac{\partial T}{\partial y})=k(\frac{\partial^2 T}{\partial x^2}+\frac{\partial^2 T}{\partial y^2}), \tag{4}$$

$$\frac{\partial \varphi}{\partial t}+\frac{\partial \varphi u}{\partial x}+\frac{\partial \varphi v}{\partial y}+\nabla\cdot(\varphi(1-\varphi)\mathbf{u}_R)=0 \tag{5}$$

The energy balance equation for pure solid region in cases 7 and 8 can be expressed as:

$$\frac{\partial T}{\partial t}=\alpha_r(\frac{\partial^2 T}{\partial x^2}+\frac{\partial^2 T}{\partial y^2}) \tag{6}$$

In the above equations, u and v are the mixture velocities in x and y-directions and C_p, α_r and k denote specific heat capacity, thermal diffusivity ratio ($\alpha_r = \alpha_s / \alpha_f$) and thermal conductivity, respectively. ρ_m and μ_m are the mixture density and viscosity of working fluids which can be computed via the volume-weighted average of the phases occupying each computational grid ($0 < \varphi < 1$) [78]:

$$\rho_m = \varphi \rho_1 + (1-\varphi)\rho_2 \tag{7}$$

$$\mu_m = \varphi \mu_1 + (1-\varphi)\mu_2 \tag{8}$$

where subscripts 1 and 2 refer to the primary and secondary phases, respectively. The term F_g in Navier-Stokes equations is the body force which would be the gravity force ($F_g = \rho_m g$) in the multiphase flow problems (cases 1 to 3) or buoyancy force ($F_g = \rho g \beta (T - T_c)$) in conjugate free convection problems (cases 7 and 8) with T_c being reference temperature. F_{ST} is the volumetric surface tension force which acts on the interface region based on the Brackbill's model [79] as:

$$F_{ST} = \sigma k \nabla \varphi \tag{9}$$

where σ represents the interfacial tension coefficient between phases and k denotes the curvature of interface defined as:

$$k = -\nabla \cdot \mathbf{n} = \frac{1}{|\vec{n}|}\left[\left(\frac{\vec{n}}{|\vec{n}|} \cdot \nabla\right)|\vec{n}| - (\nabla \cdot \vec{n})\right] \tag{10}$$

$$\mathbf{n} = \frac{\vec{n}}{|\vec{n}|},\ \vec{n} = \nabla \varphi \tag{11}$$

with $\mathbf{n}$ standing for the interface normal vector. The additional term $\nabla \cdot (\varphi(1-\varphi)\mathbf{u}_R)$ in the phase advection equation is *Artificial Compression* [53] which helps in lessening the smearing of the interface and retaining the sharpness of the interface region. Note that, the presence of $\varphi(1-\varphi)$

term in Eq. (5) allows the *Interface Compression* to be activated only in close vicinity of the interface area. $\mathbf{u}_R$ is the artificial compressive velocity which is given by:

$$\mathbf{u}_R = C_\varphi \left|\vec{u}\right| \mathbf{n} = C_\varphi \left|\vec{u}\right| \frac{\nabla \varphi}{|\nabla \varphi|} \tag{12}$$

C_φ is a constant coefficient used to control the strength of the compression velocity with the recommended value of unity [67]. Once the temperature and velocity fields are determined, the total entropy generation (S_{tot}) per unit volume for cases 7 and 8 can be calculated via the second law of thermodynamics as follows [80]:

$$S_{tot} = S_T + S_F = \frac{k}{T_0^2}\left[\left(\frac{\partial T}{\partial x}\right)^2 + \left(\frac{\partial T}{\partial y}\right)^2\right] + \frac{\mu}{T_0}\left[2\left(\frac{\partial u}{\partial x}\right)^2 + 2\left(\frac{\partial v}{\partial y}\right)^2 + \left(\frac{\partial u}{\partial y} + \frac{\partial v}{\partial x}\right)^2\right] \tag{13}$$

where S_T and S_F are two main detrimental irreversibilities induced by thermal dissipation and fluid friction, respectively. By defining the following pertinent parameters, Eq. (13) can be transformed into the non-dimensional form as [81]:

$$X = \frac{x}{H}, \qquad Y = \frac{y}{H}, \qquad U = \frac{uH}{\alpha}, \qquad V = \frac{vH}{\alpha}, \qquad P = \frac{pH^2}{\rho\alpha^2}, \qquad \theta = \frac{T - T_c}{T_h - T_c}.$$
$$t^* = \frac{t\alpha}{H^2}, \qquad Ra = \frac{g\beta(T_h - T_c)H^3}{\alpha\nu}, \qquad \mathrm{Pr} = \frac{\nu}{\alpha}. \qquad \lambda = \frac{\mu T_0 \alpha^2}{kH^2(T_h - T_c)^2}, \tag{14}$$

$$S_T = \left[\left(\frac{\partial \theta}{\partial X}\right)^2 + \left(\frac{\partial \theta}{\partial Y}\right)^2\right] \tag{15}$$

$$S_F = \lambda\left[2\left(\frac{\partial U}{\partial X}\right)^2 + 2\left(\frac{\partial V}{\partial Y}\right)^2 + \left(\frac{\partial U}{\partial y} + \frac{\partial V}{\partial X}\right)^2\right] \tag{16}$$

In Eq. (16), λ is the ratio between the viscous and thermal dissipation which is set equal to 10^{-4} similar to works of Das et al. [81] and Ilis et al. [82]. The average total entropy generation ($\overline{S}_{tot}$) is then obtained via integrating the local entropy generation rates over the entire computational domain as:

$$\overline{S}_T = \frac{1}{V}\int S_T dX\, dY \qquad \overline{S}_F = \frac{1}{V}\int S_F dX\, dY \qquad \overline{S}_{tot} = \overline{S}_T + \overline{S}_F \tag{17}$$

The relative dominance of thermal dissipation to fluid friction irreversibility can be mathematically quantified using the local and average Bejan numbers defined as:

$$Be = \frac{S_T}{S_T + S_F} \qquad \overline{Be} = \frac{1}{V}\int Be\, dX\, dY \tag{18}$$

Therefore, according to the above definition, one can conclude that for the values of $0 \le Be < 0.5$ the fluid friction irreversibility is dominant ($S_T < S_F$) whereas $0.5 < Be \le 1$ indicates dominance of thermal dissipation ($S_F < S_T$). For the particular case of $Be = 0.5$, entropy generation due to both factors are identical ($S_F = S_T$). Meanwhile, the global heat transfer rate within the thermal systems can be quantified through the average Nusselt number along the heated/cooled walls as follows:

$$Nu = \frac{hH}{k} = -\frac{\partial\theta}{\partial\vec{n}} \qquad \overline{Nu} = \frac{1}{H}\int_0^H \frac{\partial\theta}{\partial n} dn \tag{19}$$

As depicted in Fig. 1, the related initial and boundary conditions for the present problems can be specified as follows:

$u = v = 0$	On the rigid walls of the enclosures in all cases
$\theta = 1$	On the heated walls of the enclosures in cases 7 and 8
$\theta = 0$	On the cooled walls of the enclosures in cases 7 and 8
$\frac{\partial\theta}{\partial\vec{n}} = 0$	On the adiabatic walls of the enclosures in cases 7 and 8
$k_f\left(\frac{\partial\theta}{\partial\vec{n}}\right)_f = k_s\left(\frac{\partial\theta}{\partial\vec{n}}\right)_s$	On the walls of the conductive obstacle in cases 7 and 8
$\frac{\partial p^{n+1}}{\partial\vec{n}} = 0$	On the rigid walls of the enclosures in all cases

(20)

The initial conditions (at $t = 0$) inside the enclosures are based on the assumptions that the cold working fluid is motionless ($\theta = 0, u = v = 0$) under the zero-pressure filed ($p = 0$). It is worth

mentioning that, although the governing equations are discretized on the staggered-grid system but to close the Pressure Poisson Equation (PPE) in the two-step projection part of the algorithm, the homogeneous Neumann condition for the pressure ($\partial p^{n+1} / \partial \vec{n} = 0$) is imposed on the rigid walls during each time step.

2. Numerical methodology

The system of governing partial differential equations together with corresponding boundary conditions is discretized on a staggered grid system by means of a control-volume method where the pressure nodes are sited at the cell centroids while the velocity components are located on the midpoints of control volume faces, as depicted in Fig. 2 [83]. A novel hybrid PISO-Two-step projection algorithm (PISOC) is first developed and then employed for handling pressure-velocity coupling between the mass and momentum equations. A more detailed discussion and derivation procedure of the pressure-based coupled algorithm associated with the newly developed hybrid PISOC method are provided in appendix A.

The classical second-order central difference scheme is used for discretization of the diffusion terms while the proposed third-order TVD bounded scheme is utilized for the treatment of the convection terms in momentum, energy and volume fraction equations. To further improve the performance and accuracy of the VOF model, the ELVIRA technique pioneered by Pilliod et al. [84] is applied for material interface reconstruction and its curvature calculation.

2.1. A novel Third-order TVD Bounded scheme

In this subsection, a new third-order oscillation-free flux-limiter function is developed based on the TVD constraint for convection discretization and the suppression of the interface smearing in

dealing with multifluid and multi-material flow problems. In order to simplify the derivation process of higher-order monotone convection scheme in the finite-volume description, the general convection-diffusion equation in Cartesian framework without the pressure and transient terms is considered here as:

$$\frac{d}{dx}(\rho u\phi)+\frac{d}{dy}(\rho v\phi)=\frac{d}{dx}[\eta\frac{d\phi}{dx}]+\frac{d}{dy}[\eta\frac{d\phi}{dy}] \tag{21}$$

where the scalar (T,φ) and vector quantities (u, v) in Eqs. (2) to (5) are replaced by the general transport variable ϕ. By integrating Eq. (21) over a two-dimensional control volume (CV) as sketched in Fig. 2 and applying the Gauss's divergence theorem in conjunction with the classical central differencing scheme for diffusion term, the following discretized equation can be derived:

$$\begin{aligned}&F_e\phi_e-F_w\phi_w+F_n\phi_n-F_s\phi_s=\\&D_e(\phi_E-\phi_P)-D_w(\phi_P-\phi_W)+D_n(\phi_N-\phi_P)-D_s(\phi_P-\phi_S)\end{aligned} \tag{22}$$

where $F_i=(\rho u)_i\Delta A_i$ with $\Delta A_i=\Delta x=\Delta y$ and $D_i=\eta_i\Delta y/\Delta x=\eta_i\Delta x/\Delta y$ stand for the convection flux and diffusion conductance cross the cell boundaries, respectively. By defining the flux-limiter function ($\psi(r)$) and taking into account the flow direction ($\mathbf{u}^+>0$ or $\mathbf{u}^-<0$), the values of the property ϕ across the cell faces (ϕ_e, ϕ_w, ϕ_n and ϕ_s) can be approximated as follows:

$$\begin{cases}\phi_e=\phi_P+\frac{1}{2}\psi(r_e^+)(\phi_E-\phi_P), & r_e^+=(\phi_P-\phi_W)/(\phi_E-\phi_P)\\ \phi_w=\phi_W+\frac{1}{2}\psi(r_w^+)(\phi_P-\phi_W), & r_w^+=(\phi_W-\phi_{WW})/(\phi_P-\phi_W)\\ \phi_n=\phi_P+\frac{1}{2}\psi(r_n^+)(\phi_N-\phi_P), & r_n^+=(\phi_P-\phi_S)/(\phi_N-\phi_P)\\ \phi_s=\phi_S+\frac{1}{2}\psi(r_s^+)(\phi_P-\phi_S), & r_s^+=(\phi_S-\phi_{SS})/(\phi_P-\phi_S)\end{cases} \quad \mathbf{u}^+>0 \tag{23}$$

$$\begin{cases} \phi_e = \phi_P + \dfrac{1}{2}\psi(r_e^-)(\phi_P - \phi_E), \quad r_e^- = (\phi_E - \phi_{EE})/(\phi_P - \phi_E) \\ \phi_w = \phi_P + \dfrac{1}{2}\psi(r_w^-)(\phi_W - \phi_P), \quad r_w^- = (\phi_P - \phi_E)/(\phi_W - \phi_P) \\ \phi_n = \phi_N + \dfrac{1}{2}\psi(r_n^-)(\phi_P - \phi_N), \quad r_n^- = (\phi_N - \phi_{NN})/(\phi_P - \phi_N) \\ \phi_s = \phi_P + \dfrac{1}{2}\psi(r_s^-)(\phi_S - \phi_P), \quad r_s^- = (\phi_P - \phi_N)/(\phi_S - \phi_P) \end{cases} \quad \mathbf{u}^- < 0 \tag{24}$$

where $r_i^{\pm}$ stands for the ratio of upwind-side gradient to downwind-side gradient as described by Versteeg et al. [83]. More precisely, for the positive flow direction, the gradient ratio of r_w^+ on the West cell face is evaluated by $r_{i-1/2}^+ = (\phi_{i-1} - \phi_{i-2})/(\phi_i - \phi_{i-1})$ (or $r_{i-1/2}^+ = (\phi_W - \phi_{WW})/(\phi_P - \phi_W)$) whereas in the case of negative flow direction, this ratio would be equal to $r_{i-1/2}^- = (\phi_i - \phi_{i+1})/(\phi_{i-1} - \phi_i)$. In Eqs. (23) and (24), the term $\psi(r)$ is known as a flux-limiter function which is designed by the combination of two piecewise non-linear functions as:

$$\psi(r) = \begin{cases} \dfrac{(r + |r|) \times (r+3)}{3r^2 + 2r + 3} & r \le 1 \\ \dfrac{2r+2}{r+3} & r > 1 \end{cases} \tag{25}$$

To construct the above third-order accurate scheme, the necessary and sufficient criteria suggested by Sweby [85], Zijlema et al. [86], Leonard [52], Gao et al. [87], Waterson et al. [88] and Alves et al. [60] are utilized to retain the monotonicity-preserving properties of TVD scheme. It is evident from Fig. 2 that, the newly developed limiter is positive ($\psi(r) \ge 0$) and lies within the shaded area in the TVD diagram which guarantees both the boundedness (monotonicity) of the solution and at least first-order accuracy of the discretization scheme [85]. Moreover, similar to Van Leer limiter function ($\psi(r) = (r + |r|)/(1 + r)$) [89], the proposed model passes through the points $\psi(0) = 0$ and $\psi(1) = 1$ which fulfills consistency requirement for second

order accuracy [88]. It is also easy to show that the slope of the limiter function at the intersection point (1,1) is the same as that of the classical QUICK scheme ($\psi(r)=(r+3)/4$, $\left.\frac{d\psi(r)}{dr}\right|_{r=1}=\frac{1}{4}$) which in turn fulfills the desired third-order accuracy [52,86,90]. Furthermore, it can be seen from Fig. 2 that unlike the Minmod and Superbee models [91] (as the lower and upper borders of the TVD region) which switch between linear schemes with different slopes, the proposed model is smooth, finite and continuous over the entire range of *r*. In this context, it is relevant to mention that, both sub-functions of the proposed limiter reach the point (1,1) with the same slope of magnitude ($\left.\frac{d\psi(r)}{dr}\right|_{r=1}=\frac{1}{4}$) which in turn respects the convective stability criterion and fulfills *Smooth Region Condition*, accordingly. The effects of this crucial criterion on the consistency of the convection scheme were systematically investigated by Alves et al. [60] and Gao et al. [87] who mathematically proved that, the sudden alteration in the slope of limiter function near the critical point (1,1) can lead to spurious pressure oscillation near the material discontinuities in the multiphase flows. Before proceeding further, it is worth to mention that in order to prevent or minimize excessive use of *"IF"* in computer programming process and to avoid singularity of the denominator of subdomains ($r\le 1,\ r>1$) in Eq. (25), special treatment should be applied to each sub-domain of the limiter. For this purpose, by multiplying the numerator and denominator of gradient ratio (*r*) with the value of its denominator (e.g. $r=A/B=A\times B/B^2$), the following relationships can be drawn:

$$r_w^{\pm}=\begin{cases} r_{i-1/2}^{+}=r_w^{+}=\dfrac{(\phi_{i-1}-\phi_{i-2})}{(\phi_i-\phi_{i-1})}=\dfrac{(\phi_{i-1}-\phi_{i-2})}{(\phi_i-\phi_{i-1})}\times\dfrac{(\phi_i-\phi_{i-1})}{(\phi_i-\phi_{i-1})}=\dfrac{(\phi_{i-1}-\phi_{i-2})\times(\phi_i-\phi_{i-1})}{(\phi_i-\phi_{i-1})^2} \\ r_{i-1/2}^{-}=r_w^{-}=\dfrac{(\phi_i-\phi_{i+1})}{(\phi_{i-1}-\phi_i)}=\dfrac{(\phi_i-\phi_{i+1})}{(\phi_{i-1}-\phi_i)}\times\dfrac{(\phi_{i-1}-\phi_i)}{(\phi_{i-1}-\phi_i)}=\dfrac{(\phi_i-\phi_{i+1})\times(\phi_{i-1}-\phi_i)}{(\phi_{i-1}-\phi_i)^2} \end{cases} \tag{26}$$

By applying the above technique on the West cell face and considering the flow direction, the sub-domains of the limiter can be rewritten as follows:

$$
\begin{cases}
r>1 \begin{cases} r^{+}_{i-1/2}>1, & \dfrac{(\phi_{i-1}-\phi_{i-2})\times(\phi_i-\phi_{i-1})}{(\phi_i-\phi_{i-1})^2}>1, \quad (\phi_{i-1}-\phi_{i-2})\times(\phi_i-\phi_{i-1})>(\phi_i-\phi_{i-1})^2 \\ r^{-}_{i-1/2}>1, & \dfrac{(\phi_i-\phi_{i+1})\times(\phi_{i-1}-\phi_i)}{(\phi_{i-1}-\phi_i)^2}>1, \quad (\phi_i-\phi_{i+1})\times(\phi_{i-1}-\phi_i)>(\phi_{i-1}-\phi_i)^2 \end{cases} \\
r\le 1 \begin{cases} r^{+}_{i-1/2}\le 1, & \dfrac{(\phi_{i-1}-\phi_{i-2})\times(\phi_i-\phi_{i-1})}{(\phi_i-\phi_{i-1})^2}\le 1, \quad (\phi_{i-1}-\phi_{i-2})\times(\phi_i-\phi_{i-1})\le(\phi_i-\phi_{i-1})^2 \\ r^{-}_{i-1/2}\le 1, & \dfrac{(\phi_i-\phi_{i+1})\times(\phi_{i-1}-\phi_i)}{(\phi_{i-1}-\phi_i)^2}\le 1, \quad (\phi_i-\phi_{i+1})\times(\phi_{i-1}-\phi_i)\le(\phi_{i-1}-\phi_i)^2 \end{cases}
\end{cases}
\tag{27}
$$

Note that, the similar procedure should be applied to other three faces of computational cell ($r_e^{\pm}$, $, r_n^{\pm}$ and $r_s^{\pm}$) by considering the related neighboring grid points. Finally, since the high-resolution schemes are typically prone to a numerical instability owing to the appearance of negative main coefficients, the proposed model can be generalized and reformulated by incorporating the notation of upwind differencing scheme into the discretized equation as follows:

$$
\begin{aligned}
&a_P\phi_P = a_W\phi_W + a_E\phi_E + a_S\phi_S + a_N\phi_N + S_u \\
&a_W = D_w + \max(F_w, 0) \\
&a_E = D_e + \max(-F_e, 0) \\
&a_S = D_s + \max(F_s, 0) \\
&a_N = D_n + \max(-F_n, 0) \\
&a_P = a_W + a_E + a_S + a_N + (F_e - F_w) + (F_n - F_s)
\end{aligned}
\tag{28}
$$

One of the main advantages of the above format of discretization is that the main coefficient (a_P) is always positive which can effectively satisfy the needs for conservativeness and transportiveness. S_u on the right-hand side of equations is called *deferred correction* which can be expressed as:

$$
\begin{aligned}
S_u &= \frac{1}{2}F_e[(1-\gamma_e)\psi(r_e^-)-\gamma_e\psi(r_e^+)](\phi_E-\phi_P)\\
&+\frac{1}{2}F_w[-(1-\gamma_w)\psi(r_w^-)+\gamma_w\psi(r_w^+)](\phi_P-\phi_W)\\
&+\frac{1}{2}F_n[(1-\gamma_n)\psi(r_n^-)-\gamma_n\psi(r_n^+)](\phi_N-\phi_P)\\
&+\frac{1}{2}F_s[-(1-\gamma_s)\psi(r_s^-)+\gamma_s\psi(r_s^+)](\phi_P-\phi_S)
\end{aligned}
\tag{29}
$$

where γ_i is the constant parameter which depends on the flow direction as:

$$
\begin{aligned}
&\gamma_e = 1 \text{ if } F_e > 0, \quad \gamma_e = 0 \text{ if } F_e < 0\\
&\gamma_w = 1 \text{ if } F_w > 0, \quad \gamma_w = 0 \text{ if } F_w < 0\\
&\gamma_n = 1 \text{ if } F_n > 0, \quad \gamma_n = 0 \text{ if } F_n < 0\\
&\gamma_s = 1 \text{ if } F_s > 0, \quad \gamma_s = 0 \text{ if } F_s < 0
\end{aligned}
\tag{30}
$$

To provide deeper insight into the computer programming of proposed model, the FORTRAN code in term of *subroutine* is developed and documented as a supplementary material which can assist the user of a CFD code in constructing and implementing such a TVD scheme.

2.2. Interface reconstruction scheme (ELVIRA algorithm)

The programming process of ELVIRA technique pioneered by Pilliod et al. [84] is elaborated in this subsection. Generally, in the PLIC-ELVIRA model, the interface is approximated by a straight line segment ($y = m_i x + d$) where six possible gradients of the color function (φ) generated by the forward, central and backward finite-difference schemes in the *x* and *y*-directions are used to determine the interface slope. As depicted in Fig. 3, the first three possible angular coefficients of the straight line in the *x*-direction can be mathematically calculated by:

$$
\begin{aligned}
m_{x,f} &= \pm\left|\varphi_{EN}+\varphi_E+\varphi_{ES}-\varphi_N-\varphi_P-\varphi_S\right|\\
m_{x,c} &= \pm\left|\varphi_{EN}+\varphi_E+\varphi_{ES}-\varphi_{WN}-\varphi_W-\varphi_{WS}\right|\times 0.5\\
m_{x,b} &= \pm\left|\varphi_N+\varphi_P+\varphi_S-\varphi_{WN}-\varphi_W-\varphi_{WS}\right|
\end{aligned}
\tag{31}
$$

The other three underlying interface slopes can be computed by rotating the gradients of row sums by 90 degrees given by:

$$m_{y,f} = \frac{\pm 1}{\left|\varphi_{WN} + \varphi_{N} + \varphi_{EN} - \varphi_{W} - \varphi_{P} - \varphi_{E}\right|}$$
$$m_{y,c} = \frac{\pm 2}{\left|\varphi_{WN} + \varphi_{N} + \varphi_{EN} - \varphi_{WS} - \varphi_{S} - \varphi_{ES}\right|} \tag{32}$$
$$m_{y,b} = \frac{\pm 1}{\left|\varphi_{W} + \varphi_{P} + \varphi_{E} - \varphi_{WS} - \varphi_{S} - \varphi_{ES}\right|}$$

It is important to note that in the above equations, the symbol (±, plus-minus sign) should be interpreted based on the table 1 and Fig. 3. Take as an illustration, for cases A1, A2, C1 and C2 only the positive ($+m_i$) values of Eqs (31) and (32) should be used for interface reconstruction whereas for cases B1, B2, D1 and D2 the negative ones ($-m_i$) are regarded as potential slope candidates. Fig. 3 demonstrates various possible cases of interface orientation with the corresponding fluid position within the uniform stencil of 3×3 cells which can be easily distinguished from each other by defining the following two pertinent parameters:

$$n_x = (\varphi_{EN} + 2\varphi_{E} + \varphi_{ES}) - (\varphi_{WN} + 2\varphi_{W} + \varphi_{WS}) \tag{33}$$

$$n_y = (\varphi_{WN} + 2\varphi_{N} + \varphi_{EN}) - (\varphi_{WS} + 2\varphi_{S} + \varphi_{ES}) \tag{34}$$

It is interesting to mention that, n_x and n_y in the above equations are very analogous to the Youngs's model [92] who initially introduced the concept of the PLIC technique for linear reconstruction of material interfaces. It is evident from table 1 and Fig. 3 that, depending on the signs of n_x, n_y and the absolute values of the interface slope ($\left|m_i\right|$), the twelve different interface configurations are likely to emerge within the main cell. Furthermore, it is apparent that, each of the given position (except for horizontal and vertical orientations) consists of three subgroups of interface shapes (i.e. triangle, trapezoid or pentagon) which should be determined through an

iterative method until a desired response is achieved. This stage in the literature is commonly referred to as *Determination of Line Constant* [93] where the line segment ($y = m_i x + d$) is displaced iteratively within the stencil while keeping its alignment constant until the volume fraction enclosed by the reconstructed interface line becomes equal to the actual volume fraction predicted by transport equation. When the exact location of the interface line is identified, the constructed line is then extended across the 3×3 block to determine the volume fraction (φ) in each of the surrounding 8 grids. In the last stage, any candidate slopes that can minimize the following discrete error is regarded as the solution:

$$E_{i,j}(m_i) = \sum_{k,l=-1}^{1} \left| \varphi_{i+k,j+l}(m_i) - \varphi_{i+k,j+l} \right| \tag{35}$$

Where $E_{i,j}(m_i)$ is the total error between the actual volume fractions obtained from the transport equation ($\varphi_{i+k,j+l}$) and those predicted by the interface reconstruction ($\varphi_{i+k,j+l}(m_i)$). To shed further light on the structure of computer programming of the ELVIRA model, an analytical example is given here where the linear function with formula $y = 0.3x + 1.225$ intersects the vertical sides of the nine-point cell stencil. The volume fractions generated by this straight line is portrayed in Fig. 3 where the upper half of the stencil is filled by the primary phase. As a first step of the algorithm, the six possible interface slopes are calculated through Eqs. (31) and (32) namely: ($m_{x,f} = \pm 3/10$, $m_{x,c} = \pm 3/10$, $m_{x,b} = \pm 3/10$, $m_{y,f} = \pm 480/947$, $m_{y,c} = \pm 384/571$ and $m_{y,b} = \pm 960/961$). In the second step, the interface orientation and position of the heavier fluid are determined using Eqs. (33) and (34). It can be seen from Table 1 that, according to the values of $n_x = -1127/960 < 0$ and $n_y = 763/192 > 0$ (irrespective of $|m_i|$), the existing cases for the test problem would be C1 and C2 which in turn indicate that only positive values of interface slopes

should be considered for the interface reconstruction process namely: $m_{x,f}=+3/10$, $m_{x,c}=+3/10$ $m_{x,b}=+3/10$, $m_{y,f}=+480/947$, $m_{y,c}=+384/571$ and $m_{y,b}=+960/961$. For the first attempt, $m_{x,f}=+3/10$ is chosen as the angular coefficient of the straight line ($y_{Interface}=0.3x+d$). Meanwhile, by taking into account the role of $\left|m_{x,f}\right|<1$ as a third condition along with $n_x<0$ and $n_y>0$ in Table 1, the possible interface mode is reduced to case C2. In the next stage, the shape of the fluid polygon among the three possible cases (i.e. triangle, trapezoid or a pentagon) should be identified. To accomplish this, the area of the biggest possible fluid triangle and trapezoid enclosed in the central cell are first calculated and then compared with the actual value of volume fraction. It can be seen from Fig. 3 that the volume fraction obtained by the exact solution is positioned between the volume fraction of the biggest possible triangle and trapezoid ($\varphi_{\text{Triangle}}<\varphi_{Actual}<\varphi_{\text{Trapezoid}}$) which implies that the interface polygon has a shape of trapezoid. In the fourth stage, the linear function should be calibrated within the main grid to reproduce the correct volume fraction ($\left|\varphi_{Actual}-\varphi_{Interface}\right|\le 10^{-10}$). As mentioned earlier, this stage is equivalent of finding the line constant (*d*). From Fig. 3 one can conclude that, according to $\varphi_{\text{Triangle}}<\varphi_{Actual}<\varphi_{\text{Trapezoid}}$, the line constant of interface should be located between *y*-intercepts of the largest possible triangle and trapezoid polygons ($0.7\le d\le 1.4$) created with the formulas $y_{Triangle}=0.3x+1.4$ and $y_{Trapezoid}=0.3x+0.7$, respectively. Hence, the arithmetic average of the highest and lowest *y*-intercepts ($d_{Trial1}=(1.4+0.7)/2=1.05$) is taken as the first trial in the iterative process. However, it is evident from Fig. 3 that the volume fraction produced by the new interface line ($y_{Interface}=0.3x+1.05$) is still lower than that of the actual one which implies that the second iteration is needed to reach a desired solution. Since, $\varphi_{\text{Trial1}}<\varphi_{Actual}$, the lowest

value of *y*-intercept is first replaced by the guessed one computed from the previous iteration, and then the averaging process ($d_{Trial\,2} = (1.4+1.05)/2 = 1.225$) is repeated. It should be mentioned that, in the case of $\varphi_{\text{Trial1}} > \varphi_{Actual}$, the highest value of line constant should be replaced by the guessed value obtained from the previous trial. It can be seen from Fig. 3 that, the newly constructed interface line ($y_{Trial\,2} = 0.3x + 1.225$) can successfully reproduce the correct volume fraction. Having determined the true line constant, the volume fractions in the neighboring nodes can be estimated as depicted in Fig. 3. The above procedure should be applied to the other five remaining slopes and the one that can minimize the following residual is the winner:

$$m_i = \min\left\{E_{i,j}(m_{x,f}), E_{i,j}(m_{x,c}), E_{i,j}(m_{x,b}), E_{i,j}(m_{y,f}), E_{i,j}(m_{y,c}), E_{i,j}(m_{y,b})\right\} \tag{36}$$

Once the optimal interface line is determined, its normal vector ($n_y y + n_x x = d$) can be calculated as follows:

$$m_i y + x = m_i d \tag{37}$$

where $n_y = m_i$ and $n_x = 1$ are the components of normal vector. Finally, similar to the previous sections, in order to provide deeper insight into the computer programming of ELVIRA technique, the FORTRAN code is developed and documented as supplementary material.

3. Results and discussion

In this section, eight different canonical test cases are employed to demonstrate the accuracy and reliability of the proposed modifications in handling convection heat transfer and non-hydrostatic free surface flow with complex interface morphologies and topological changes. A classical 2D dam-break problem (case 1) is first adopted to verify the capability of the enhanced VOF model in capturing moving free surfaces involving severe interfacial deformation, coalescence and

breaking-up events associated with water re-entry, impact pressure and splashing. To further assess the performance of the proposed third-order TVD bounded convection scheme in suppressing false diffusion errors and spurious numerical smearing (i.e. smearing of the interface thickness), the nonlinear development of 2D Rayleigh-Taylor instability is analyzed as the second benchmark test problem (case 2) where two immiscible fluids are evolved under the combined action of viscous and buoyancy forces. Simulation of a single gas bubble rising in a liquid column (case 3) is conducted to validate the effectiveness of the ELVIRA technique in accurate estimation of surface tension force and its corresponding interface curvature. The classical Rotation of a slotted disk (case 4), deformation of a 2D disk (case 5) and pure convection of a step profile (case 6) are chosen to demonstrate the capability of the newly-developed TVD bounded convection scheme in capturing steep gradients. The robustness and stability of the newly proposed semi-iterative PISOC-algorithm in dealing with the velocity-pressure coupling problem is further demonstrated through analysis of transient entropy generation due to conjugate natural convection heat transfer in square enclosures (cases 7 and 8).

3.1.Dam break (case 1)

The schematic diagram of the dam break model is given in Fig. 1. In this numerical test, the rectangular water column ($\rho_W = 997\,Kg/m^3$ and $\mu_W = 855\times10^{-6}\,Pa.s$) with width and height of the $W = 0.25\,m$ and $H = 0.5\,m$ in hydrostatic equilibrium is initially installed on the LHS of the square container with dimensions of $[1m,1m]$. The rest of the enclosure is occupied by air ($\rho_A = 1Kg/m^3$ and $\mu_A = 185\times10^{-7}\,Pa.s$) as the outer medium (second phase) and the surface tension force ($\sigma = 71.1\times10^{-3}\,N/m$) is taken into account. The simulation is conducted on 350×350 grid resolution and time sequence of the collapsing water column in terms of the

volume fraction fields together with the pressure contours are plotted in Fig. 4 at different dimensionless time instants ($t^* = t\sqrt{\mathbf{g}/H}$). Generally, the dynamic evolution of the dam failure can be classified into four distinct stages. The first stage encompasses the destruction of the vertical gate and propagation of the wave front over the dry-deck until the surge front reaches the downstream rigid wall ($0 \le t^* \le 1.5$). From Fig. 6 one can observe that, the water level height at the dam site ($l_1 = 0.1m$) monotonically lessens which implies that the conversion between potential and kinetic energy takes place primarily at this stage. The second stage involves the formation of the shock pressure due to impact of water toe with the opposite vertical wall which in turn is accompanied by the development of the ascending fluid jet and semi-hydrostatic pressure distribution on the bottom right corner of the enclosure ($1.5 < t^* \le 2.26$). A close inspection of Fig. 6 (c) shows that, the maximum impact pressure recorded by sensors 2 ($h_2 = 0.025m$) at $t^* = 1.59$ s is approximately equal to $p^* = 2.057$ which is in accordance with previously published measurements [94,95]. Furthermore, it can be seen that, the maximum run up of the liquid jet in the vicinity of the right wall exceeds twice the initial water column height which is compatible with the numerical findings of Colagrossi et al. [96]. However, as time progresses ($2.26 < t^* \le 3.42$), due to the oncoming fluid flow and retarding effect of the gravity force, the fluid acceleration declines and subsequently the thickness of the upward-moving jet increases. This process corresponds to the continuous reduction in the pressure shock loading and establishment of the stagnation point (fluid trapping) on the corner of the enclosure. The third stage takes into account the appearance of the plunging breaking wave where, due to the restoring action of gravity and the fluid-solid interaction adjacent to the right wall, the rising water jet begins to overturn backwards and eventually hits the underlying moving wetted deck, thereby forming the closed air-cushion structure and second shock pressure scenario ($t^* = 4.3$,

$p^* = 0.704$) within the container ($3.42 < t^* \leq 4.42$). Finally, in the last stage, the newly generated flying jet starts to travel towards the upstream left wall where the water splash-up process and interface fragmentation/breaking are likely to occur on the tip of the second plunging jet ($t^* < 4.42$).

Qualitative and quantitative comparison of the predicted results with numerical works of Xu et al. [94] and Zheng et al. [95] in Figs. 5 and 6 show that, the trajectory of the tip of the plunging jet and air entrapment phenomenon (closed cell structure) are well captured and reproduced by the present model. The close-up snapshots of the interface before and after wave breaking in Fig. 6 (a) clearly demonstrate that the sharpness (thickness) of the interface is well controlled and confined to a maximum of 2-3 grid stencil which in turn highlights the robustness of the proposed non-linear flux limiter scheme (Eq. (25)) in eliminating interface smearing and numerical diffusion errors. In order to better quantify the accuracy of the numerical model, the time variations of the water front (X_{front}), non-dimensional values of water level height (h/H) at three different sections and pressure time histories recorded at six different sampling points (h_i) on the left and right vertical walls are presented in Fig. 6. It is evident that the predicted results are smooth without non-physical oscillations and are in excellent agreement with those obtained by reference numerical solutions [94,95]. However, there are some small discrepancy between the results which can be partially attributed to neglecting the surface tension or due to the occurrence of the so-called tensile instability problem and its consequent particle clustering in the Lagrangian particle methods which trigger pressure oscillations in published results of [94,95].

3.2.Rayleigh-Taylor instability (case 2)

As schematically shown in Fig. 1, the simulation is carried out in the rectangular enclosure with dimension of the $[1m, 2m]$ where a denser fluid with physical properties of $\rho_H = 1.8\,Kg/m^3$ and $\mu_H = 0.018\,Pa.s$ lies on top of a lighter fluid ($\rho_H = 1Kg/m^3, \mu_H = 0.01\,Pa.s$) at $t = 0\,s$ with a locally perturbed interface of $y = 1 - 0.15 \times \sin(2\pi x)$. The instability is governed by the Reynolds and Atwood numbers of $\mathrm{Re} = \rho_H H\sqrt{H\mathbf{g}}/\mu_H = 420$ and $At = (\rho_R - 1)/(\rho_R + 1) = 2/7$ where $H = 1m$ denotes the width of the enclosure and $\sqrt{H\mathbf{g}}$ stands for the reference velocity with $\mathbf{g}$ being the gravitational acceleration. Initially, the system is at rest ($\mathbf{u} = 0\,m/s$) and no-slip boundary condition is imposed on all rigid walls. Similar to works of Rezavand et al. [97], Pahar et al. [98] and Li et al. [99], owing to the relatively large radius of interface curvature, the influence of the surface tension force is neglected. The computations are conducted on a 200×400 grid resolution and predicted results are presented in Figs. 7 and 8 at various non-dimensional time ($T = t\sqrt{\mathbf{g}/H}$) instants. Generally, due to buoyancy/gravity forces and initial distortion, the dynamics of the RTI problem is characterized by falling of the denser fluid as a spike along the left wall and upward movement of the lighter fluid as a bubble, which lead to the appearance of the mushroom-like structure within the enclosure. Inspection of Figs. 7 and 8 reveals that, during the early stages of the RTI development ($T \le 2$), the contours of the velocity components and shapes of the bubble/spike fronts remain entirely symmetrical with respect to the center of the enclosure which implies that morphology and the growth of the instability are primarily governed by the viscous force. As time goes on ($2 < T \le 4$), the heavy fluid penetrates further into the less dense fluid and consequently the intensity of the transverse velocity augments and exceeds the critical value (see also $|u_{\max}|$ in Fig. 8 (d)). At this stage, the interface

evolves into an asymmetric shape and undergoes severe morphological deformation which signifies that shear velocity and Kelvin-Helmholtz instability are coming into the picture [100]. This process is also accompanied by the formation of the four secondary recirculating zones along the wings of the ascending and descending plumes which causes the interface to roll up, resulting in the significant twisting and distortion of the interface. Towards the end of the calculation ($4 < T \leq 6$), due to the imposition of the no-slip and impermeable boundary conditions, more and more eddies are generated at the tails of the roll-ups and magnitude of the velocity field progressively lessens which indicates that the RTI evolution enters into the strongly nonlinear regime. In this circumstance, the major portion of the nonlinear spike advances with the vortex shedding and curvature effects of the ring eddies, leading to the development of the jet-like circulation and complex flow structure in the lower part of the container. Qualitative comparison of obtained results with previously published data [97–99] in Fig. 7 vividly confirms the capability of the modified VOF model in handling multi-fluid flows with large deformations and topological changes. It is evident that the interface between two fluids is smooth and successfully captured without any smearing. The time history of the bubble front and spike tip is depicted in Fig. 8 (c) and good agreement is found with reference numerical measurements [98].

3.3.Bubble rising (case 3)

To further evaluate the performance of the ELVIRA technique in calculating the interface-normal vector and its corresponding surface-tension force (Eq. (10)), the hydrodynamic characteristics of a single rising bubble in quiescent liquid is examined in this subsection. As graphically shown in Fig. 1, the simulation is carried out in a rectangular duct with geometrical dimensions of $[4H, 6.48H]$ where the circular bubble ($\rho_L = 1 Kg/m^3$ and $\mu_L = \sqrt{2}/200\, Pa.s$) with

nominal radius of $H = 0.25m$ is initially immersed in a stationary heavy fluid ($\rho_H = 100\,Kg/m^3$ and $\mu_H = \sqrt{2}/2\,Pa.s$) which occupies the entire enclosure. No-slip and impermeable boundary conditions are imposed on all rigid walls and calculations are performed on the 200×324 uniform mesh which is fine enough to capture large deformation and breakup of the interface. Similar to work of Zhao et al. [101], the Reynolds number ($Re = D\sqrt{2Hg}/\upsilon_H$) based on the reference velocity ($\sqrt{2Hg}$) and characteristic length ($D = 2H$) is set to $Re = 100$ where $\upsilon_H = \upsilon_L$ denote the kinematic viscosity of the denser and lighter fluids. The Weber number ($We = \rho_H g(2H)^2/\sigma$) based on the properties of the surrounding liquid is chosen as 200, corresponding to the surface tension coefficient $\sigma = 0.5\,N/m$. The components of the initial velocity vector and background pressure are set to zero ($p_0 = 0$ and $\mathbf{u}_0 = 0\,ms^{-1}$) and the obtained results in terms of the temporal evolution of the bubble trajectory with associated velocity contours are presented in Figs. 9 and 10. It can be seen that, due to the existence of the density gradient between two phases, the buoyancy force causes the air bubble to float up along the centerline of the enclosure while the heavy fluid sinks to the lower section at the vicinity of the vertical walls, creating a pair of counter-rotating streamwise vortices on both sides of the bubble. However, during the floating process, owing to the downwelling motion of the denser fluid and shedding of two vortices from the main body, the cores of the primary eddies are dragged towards the lower portion of the enclosure and subsequently the bubble shape begins to evolve into the horseshoe-like structure ($2 \le t^* \le 4.5$). Fig. 10 reveals that this interface stretching/twisting process is also accompanied by significant enhancement in the flow intensity and the development of the wake structure in the rear of the gas phase which causes the tails of the bubble to fold inward and elongate in the *y* axis. This mechanism signifies that the effects of

the shearing-velocity become more prominent as time advances. Note that this stage corresponds to maximum rate of bubble deformation such that the bubble shape is reconfigured to the cap-like structure with terminal velocity ($|V_{\max}| = 3.69$). However, Fig. 9 shows that, during the deceleration stage ($4.5 < t^* \le 5$), the bubble motion and its rate of deformation abruptly slow down and remain nearly constant, indicating that the fluid attached to the vertical walls is likely to be in the regime of creeping flow [102,103]. Meanwhile, the shearing-stress in conjunction with surface tension force starts to stretch the interface into thin layer. It is evident that during this sequence ($4 < t^* \le 5$), the bubble skirts become progressively squeezed and thinner, resulting in the occurrence of bubbles detachment and interface rupture behind the ascending bubble. Finally, in the last stage ($5 < t^* \le 6$), due to both drift and lift forces generated by vortex shedding (wake-induced forces), two detached bubbles are directed towards the vertical cross-section and begin to follow the convection path of the rolled-up vortices. The corresponding velocity fields at this moment resemble approximately dipole-shaped pattern which in turn manifest the formation of some secondary recirculating eddies inside the rising bubble.

A comparison of calculated results with the previously published data based on the VOF solution on unstructured triangular grids with adaptive mesh refinement [101] in Figs. 9 and 10 demonstrates that, despite the negligible differences between the two numerical outcomes, the hydrodynamic behavior of rising bubble including wake generation, interface filamentation/fragmentation together with the bubbles detachment process is well reproduced by the enhanced VOF method.

3.4. Rotation of a slotted disk (Zalesak's problem)

To further demonstrate the accuracy and robustness of the proposed third-order bounded convection scheme in suppressing false-diffusion error and maintaining the sharpness of the interface, the solid-body rotation case of Zalesak [104] (case 4) is considered here as a fourth benchmark test problem. As schematically shown in Fig. 1, the calculation is performed in a square enclosure ($H = 1m$) with 200×200 grid resolution where the notched disk with nominal radius of $R = 0.15m$ is initially centered at $(0.5, 0.75)$. The width and the length of the slot are set equal to $W = 0.05m$ and $L = 0.25m$ similar to works of Owkes et al. [105] and Ming-Jian Li [106]. The notched disk is subjected to a counter-clockwise rotating eddy given by:

$$\begin{aligned} u &= -2\pi(y - 0.5) \\ u &= +2\pi(x - 0.5) \end{aligned} \tag{38}$$

The transient evolution of volume-fraction field at various time instants is depicted in Fig. 11. It is evident that, the general shape of the slotted circle is successfully preserved after one full rotation. The qualitative and quantitative comparisons of the obtained results with previously published data in terms of the final shape of the slotted disk and accumulated error ($\mathrm{E}_{\mathrm{Zalesak}} = \sum_{i=1,j=1}^{N} \left| \varphi_{i,j} - \overline{\varphi}_{i,j} \right| \Big/ \sum_{i=1,j=1}^{N} \overline{\varphi}_{i,j}$) are presented in Fig. 11 and table 2. It can be seen that, despite a little smoothing on the sharp edges, the proposed improved VOF model can accurately maintain the initial configuration and outperformed four other existing Eulerian models tested by Cifani et al. [63] and Ming-Jian Li [106]. Finally, from table 2 one can deduce that, the predicted results in the current work is more consistent with Lagrangian methods suggested by Scardovelli et al. [93].

3.5. Deformation of a 2D disk (case 5)

The transient deformation of a weightless liquid circular disk with nominal radius of $R = 0.15m$ centered at $(0.5, 0.75)$ within a unit square domain ($H = 1m$) is examined in this subsection as fifth canonical test case where due to the presence of non-uniform vorticity field (shearing flow), the initially circular disk begins to evolve into a spiral structure with maximum distortion. The simulation is carried out on 256×256 uniform grid system and periodic boundary condition is imposed on all enclosure walls. As sketched in Fig. 1, the computational domain is subjected to a single vortex described by [105]:

$$\begin{aligned} u &= -2\sin^2(\pi x)\sin(\pi y)\cos(\pi y)\cos(\frac{\pi t}{T}) \\ v &= +2\sin^2(\pi y)\sin(\pi x)\cos(\pi x)\cos(\frac{\pi t}{T}) \end{aligned} \tag{39}$$

where u and v denote velocity components in x and y-directions. The term t is time and T=8.0 represents the period of the velocity field. The sequential evolution of rotating disk at various time instants is portrayed in Fig. 12. It can be observed that contrary to previous test case (Zalesak's disk), due to the imposition of the solenoidal velocity field, the circular fluid body is progressively stretched and dragged towards the centre of the recirculating zone, giving rise to the development of the thin continuous spiral-shaped filament within the enclosure at $t = T/2 = 4s$. However, owing to the existence of cosinusoidal temporal factor ($\cos(\pi t/T)$), the fluid flow starts moving backwards in a counterclockwise direction ($T/2 < t$) until the elongated disk returns to its equilibrium (initial) position at T=8.0. The comparison of the predicted results with numerical works of Cifani et al. [63], Owkes et al. [105] and Ming-Jian Li [106] in Fig. 13 and table 3 illustrates that, in spite of severe topological change of rotating disk during its evolution, mass conservation and the thickness of the thin filament are effectively preserved by

the proposed model. Furthermore, Fig. 13 illustrates that, in contrast to the well-known Upwind and Minmod schemes, the newly-proposed convection scheme (Eq. (25)) vividly demonstrates excellent overall performance in terms of accuracy and eliminating false diffusion errors. Similar observation was also reported by Zhang et al. [107] who investigated the performance, accuracy and stability of nine different composite high-resolution convective schemes in dealing with the multiphase flows with material discontinuities.

3.6. Pure convection of a step profile (case 6)

The superiority and capability of the proposed non-oscillatory TVD flux-limiter scheme over the five classical monotone convection schemes in minimizing false-diffusion errors are further verified via simulation of the advective transport of a step profile in an oblique velocity field [107]. As shown in Fig. 1, the calculations are performed in a square cavity where Dirichlet boundary conditions are applied to the left ($\varphi = 1.0$) and bottom ($\varphi = 0$) sides of the domain while homogeneous Neumann boundary conditions are imposed on the right ($\partial\varphi/\partial x = 0$) and top ($\partial\varphi/\partial y = 0$) walls. The computational domain is subjected to the uniform velocity field ($u = v = 1.0$), oblique to the grid system at an angle of 45 degree with respect to the horizontal direction. The governing conservation equation of the problem is:

$$\frac{\partial \varphi}{\partial t} + \frac{\partial \varphi u}{\partial x} + \frac{\partial \varphi v}{\partial y} + \nabla \cdot (\varphi(1-\varphi)\mathbf{u}_R) = 0 \tag{40}$$

where φ represents the dependent variable and u and v are the velocity components in the Cartesian framework. To be consistent with literature [90,107], a uniformly spaced grid size of 120×120 is utilized for the simulations and the first-order implicit Euler scheme is employed for the time discretization. The temporal evolution of volume fraction field using three different schemes is displayed in Fig. 14. As expected, the substantial improvement has been obtained by

implementing the proposed third-order TVD scheme whereas the first-order bounded schemes (i.e. Minmod and Upwind) are characterized by severe numerical diffusion which can be attributed to the larger truncation errors generated by these schemes. This finding is also in accordance with the conclusions drawn from the previous benchmark problem and those reported by Darwish et al. [90]. The comparison of the obtained results with five other conventional TVD schemes in term of the computational φ values along a vertical line of $x = 0.7m$ at steady state condition in Fig. 15 once again confirms the superiority and robustness of the current non-oscillatory TVD flux-limiter scheme over the existing monotone convection schemes in capturing steep gradients.

3.7. Conjugate natural convection-conduction heat transfer (cases 7 and 8)

The transient entropy generation due to buoyancy-driven conjugate thermal convection in two different horizontal annular ducts with a centered internal conducting obstacle ($L = 0.3H$) is analyzed in this subsection. As schematically shown in Fig. 1, the first benchmark problem (case 7) is strictly analogous to the classical Differentially Heated Cavity (DHC) [17] where gravity force is perpendicular to the temperature gradient. In this case, the isothermal heating and cooling are imposed on the vertical walls whereas the horizontal walls are thermally insulated. However, contrary to case 7, to induce the buoyancy force and Rayleigh-Bénard Convection (RBC) [108] in case 8, the horizontal walls of the enclosure are kept at different constant temperatures ($T_c < T_h$) while the side walls are maintained adiabatic. The spaces between the two concentric squares in both cavities are filled with air ($\mathrm{Pr} = 0.71$) as a working fluid and the thermal conductivity ratio of solid to fluid is taken as $K_r = 0.2$ similar to work of Das et al. [109]. Based on the grid independency test provided in table 4, the simulations are carried on

159×159 uniform mesh resolution and obtained results in the forms of streamlines, isotherms, local and average Bejan number, entropy generation due to heat transfer irreversibility (S_T) and viscous dissipations (S_F) are presented in Figs. 16 to 21 at various Rayleigh numbers ($10^4 \le Ra \le 10^7$).

Generally, due to the existence of temperature differences within the enclosures, the flow patterns and temperature distributions are characterized by upward movement of the heated fluid and downward motion of the cooled one, which lead to the thermal energy exchange between the two active walls. Fig. 16 reveals that, in case 7, the buoyancy force induced by differentially heated/cooled sidewalls causes the fluid to move upward along the left wall until it encounters the insulated top wall. After impinging to the top wall, the expanded fluid changes its direction and travels horizontally towards the right wall as its internal energy decreases. As the fluid approaches the downstream wall, because of its interaction with surrounding cold fluid, its temperature decreases and consequently the fluid becomes gradually colder and denser. The relatively condensed fluid eventually reaches the boundary layer of the cold wall and starts to flow down and exchange its high level of energy. Since the bottom wall is sealed, the heavy fluid moves obliquely outward towards the hot area to complete its thermal cycle. Hence, the clockwise-rotating eddy is established within the annulus. This process is repeated until no significant improvement is observed in the rate of heat transfer (steady-state condition). It can be seen that at $Ra = 10^4$, isotherms in case 7 are almost parallel to each other and evenly distributed which indicate that the flow and temperature are in the weak coupling regime and heat transfer is governed by conduction mode. However, by increasing the Rayleigh number up to 10^5, the role of the buoyancy force becomes more pronounced and subsequently isotherms start to follow the pattern of streamlines, signifying the onset of natural convection at this stage. In addition, it is

seen that due to the relative dominance of convection mode, both isotherms and streamlines are more clustered and compressed in the vicinity of the active walls and two secondary vortices are appeared in both sides of the conductive obstacle which manifests the presence of adverse pressure gradients in those regions. With further increase in the value of Rayleigh number ($Ra = 10^6$), the clustering structure becomes more prominent and distinct thermal boundary layers are established in close proximity of the vertical walls. In this circumstance, due to substantial coupling of the heat and fluid flows, the isotherms and cores of the two secondary vortices get distorted and shifted towards the sidewalls where high levels of velocity gradients occur. The horizontally oriented isotherms across the block in Fig. 16 confirm that, steep temperature gradients exist in the vertical direction, signifying the high level of thermal mixing within the enclosure. The absolute value of maximum stream function ($|\psi_{\max}|$) in table 5 reveals that, further increment of Rayleigh number ($Ra = 10^7$) leads to remarkable intensification of convective flow and heat exchange inside the enclosure. It can be seen from Fig. 16 that this stage is dynamically characterized by the development of small localized eddies on the corners of the cavity and significant reduction in the thermal boundary layers thickness which support the dominance of the convective regime.

However, by rotating the differentially heated vertical cavity (case 7) by 90 degree in clockwise direction, the RBC configuration (case 8) will be established where gravity force becomes parallel to an imposed horizontal temperature gradient. By examining the thermal structure and dynamics of RBC in Fig. 17 one can deduce that, at the same nominal values of Rayleigh and Prandtl numbers, RBC exhibits fundamentally different heat and momentum transport characteristics compared to DHC during its evolution. In general, according to linear stability theory [18], hydrodynamics and thermal behaviors of Rayleigh-Bénard Convection can be

classified into the three distinct regimes, namely: (a) diffusion-dominated regime where four symmetric CW and CCW eddies are formed within the enclosure and isotherms are horizontally oriented ($Ra \le Ra_{Critical}$ with $Ra_{Critical} = 1708$ being the critical Rayleigh number), (b) stable-convection-dominated regime where viscous force is strong enough to overcome the oscillatory behavior of RBC instability where the CW eddy together with two secondary CCW vortices are developed within the enclosure ($Ra_{Critical} < Ra \le 5\times10^6$) [108] and (c) unstable-convection-dominated regime where transition from laminar to turbulent flow occurs ($5\times10^6 < Ra \le 10^7$) [110]. It should be noted that in the last stage, owing to the inherent unsteady nature of the RBC, the streamlines and isotherms constantly change their topology such that oscillatory and non-stationary thermal plume structures are cyclically emerged and disappeared inside the enclosure. Based on the above discussions and information from the literature, the thermal hydraulic behavior of RBC portrayed in Fig. 17 can be qualitatively analyzed as follows.

Starting from a cold isothermal initial state at $Ra = 10^4$, it can be seen that the process consists of the development of the ascending thermal plume in the close proximity to the hot boundary which causes the fluid to move upward along the centerline of the enclosure and eventually impact on the bottom of the conductive obstacle. However, since the *Ra* is greater than the critical value, the vertical symmetry feature ultimately dies out and the clockwise recirculating eddy is created inside the enclosure. Moreover, isotherms are vertically stratified and weak thermal gradient is formed inside the obstacle which in turn supports the inception of the convection at this *Ra*. As shown in Fig. 17, the early stages of flow evolution at $Ra=10^5$ are qualitatively similar to the transient variations of temperature and velocity fields at $Ra=10^4$ where flow bifurcation occurs. As time elapses, the buoyancy force overweighs the retarding effects of the viscous force, leading to the formation of the strong CW rotating cell and two

distinct thermal boundary layers near the horizontal walls. Similar to the previous case, the significant twisting of the isotherms and streamlines are interpreted to reflect improvements in the convection heat transfer within the annulus. With increasing Rayleigh number (Ra=10^6), due to high buoyancy-to-inertia ratio, a pair of ascending thermal plume is generated in the left and right halves of the obstacle. The formation of these swaying and swirling structures of thermal plume is also responsible for the development of some secondary vortices within the enclosure. As time progressed over the period of $0.0187 \le t \le 0.0525$, two separate plumes begin to coalesce, creating two distinct recirculation zones, namely: (a) the primary clockwise vortex (Bénard cell) which occupies the major part of the enclosure and (b) two secondary counter-clockwise eddies which are spatially confined to the smaller regions near the top-left and bottom-right corners of the enclosure where isotherms are largely clustered and characterized by the heat entrapment. It is worth recalling that, similar to the work of Ouertatani et al. [108], the flow structure and temperature pattern together with the two minor convective cells are completely symmetric with respect to the center of the cavity. It is worth noting that, such a change of flow structure is known as the symmetry-breaking bifurcation which typically occurs in the transient natural convection between two parallel plates with a heated horizontal base and cooled upper walls [111,112]. It is evident that as the time increases ($0.0525 < t$), the primary cell grows in size and squeezes two CCW vortices towards the corners of the enclosure until the steady-state condition is achieved. As expected, with further increase of the Rayleigh number (Ra=10^7), the strength of the convective flow augments and subsequently RBC enters into the unsteady convection regime where flow and thermal fields undergo severe distortions and structural alterations. It is evident that, at the very beginning of the transient evolution ($0 \le t \le 0.0059$), three distinct thermal plumes and unstable multi-cellular structure are formed within the

enclosure. As time goes on ($0.0059 < t \leq 0.0637$), the buoyancy force begins to disrupt the symmetrical pattern of the vortices, leading to the initiation of convective instability and the occurrence of vortex breakdown, accordingly.

The time-evolution of the local Bejan number and entropy generation due to heat transfer irreversibility associated with cases 7 and 8 at various Rayleigh number are displayed in Figs. 18 and 19. A detailed examination of Fig. 20 reveals that, at low Rayleigh number (Ra=10^4) due to diffusion-dominated regime and weak convection effects, the local Bejan number values in most parts of the enclosure in both cavities are close to unity which implies that most of the exergy destruction takes place as a results of the heat transfer irreversibility ($S_F < S_T$). The corresponded local entropy generation due to thermal dissipation in Fig. 19 shows that the active zones of S_T in case 7 are more confined to the small regions near the bottom-left and top-right corners of the enclosure where maximum heat transfer rate occurs. In contrast, S_T is almost trivial in middle portions of the adiabatic walls where isotherms are smooth curves and uniformly scattered due to insignificant heat flow in those areas. It is interesting to note that, this course of the event also takes place in case 8 but in revers manner such that due to considerable amount of heat flow along the horizontal walls, heat transfer irreversibility (S_T) is found to be maxima in the bottom-left and top-right junctions of the isothermal-adiabatic walls whereas vertical walls have negligible contributions to S_T. Table 5 illustrates that, as the Ra enhances, entropy generation due to both factors (S_T, S_F) augment whereas a reverse trend is found in the values of average Bejan number. This behavior can be attributed to the fact that, by increasing the Ra, the thickness of the thermal boundary layer decreases and intensity of the convection flow and recirculation patterns augment. The reduction in the thermal boundary layer thickness and augmentation in the compression of temperature profiles are interpreted to reflect the intensification of temperature

gradient, heat transfer rate and S_T. On the other hand, an increase in the buoyancy force promotes the fluid motion and elevates velocity gradients, leading to significant enhancement in the fluid friction irreversibility according to Eq. (16). However, since, entropy generation due to fluid friction irreversibility (S_F) grows much faster compared to the thermal dissipation (S_T), the local and average Bejan number decline rapidly and become less than half ($\overline{Be} < 0.5$) which indicates that the dominant source of irreversibility is shifted toward the viscous dissipation. This trend is continued or even accentuated as the *Ra* increases. This assertion is well borne out by Fig. 18 where due to the existence of flow separation and weak fluid circulation in the left and right portions of the conductive obstacle in case 7, the fluid movement is restrained and thereby the local Bejan number becomes greater than half in those areas. However, the situation gets worst in case 8. As deduced from the magnitude of streamlines in table 5 ($|\psi_{\max}|$), because of high intense fluid circulation cells, the entire enclosure in Rayleigh-Bénard Convection (RBC) acts as an active site of the entropy generation due to friction irreversibility (compare also the values of $|\psi_{\max}|$ between cases 7 and 8 in table 5). Further inspection of table 5 also reveals that the optimal situation based on the highest heat transfer rate and lowest entropy generation also takes place in case 7. Take as example, the ratios of average Nusselt number over that of total entropy generation ($\overline{Nu}/\overline{S}_{tot}$) in case 7 at $Ra = 10^4$, 10^5, 10^6 and 10^7 are equal to 0.68, 0.2, 0.027 and 0.0031 while these ratios for case 8 are approximately 0.64, 0.12, 0.014 and 0.0016, respectively. In fact, these outcomes convey that Differentially Heated Cavity (DHC) outperformed the RBC from the viewpoints of optimal design, energy saving and minimization of entropy generation. Similar observations were also reported by Anandalakshmi et al. [113] who examined the effects of the *Ra* on the entropy generation during free convection heat transfer in rhombic enclosures with various inclination angles. Furthermore, it is apparent from Figs. 18 and 19 that, similar to

velocity and temperature fields, the contours plots of local *Be* and S_T in both cases are symmetrical with respect to the center of the enclosure which can be regarded as an extra validation from the standpoints of energy balance and mass conservation. By comparing Figs. 18 and 19 one can conclude that, although the maximum entropy generation due to heat transfer ($S_{T,\max}$) still occurs near the heated surfaces where the isotherms are largely compressed, but due to imposition of the no-slip boundary conditions and enhanced convection effect at Ra=10^6, the significant velocity gradients are also generated in close vicinity of the rigid walls (S_T □ S_F), leading to the notable reduction in the values of local Bejan number in those areas ($Be < 0.5$). Finally, at Ra=10^7 due to high velocity gradients generated by the buoyancy force, viscous dissipation increases immensely and covers the more part of the domain which implies that at this stage the substantial amount of available work (exergy) might be utilized to overcome the energy losses induced by frictional irreversibility.

For getting further insight into the effects of Rayleigh number on the performance of thermal systems in cases 7 and 8, time histories of the average Nusselt number ($\overline{Nu}$), total entropy generation ($\overline{S}_{tot}$) due to both factors ($\overline{S}_T$, $\overline{S}_F$) and average Bejan number ($\overline{Be}$) are depicted in Fig. 20. As expected for all cavities, both heat transfer rate ($\overline{Nu}$) and overall entropy generation augment with increasing Rayleigh number while a reverse trend is observed in the values of $\overline{Be}$. As stated before, an increase of *Ra* improves buoyancy force and consequently the heat flow effects, hence, the values of both $\overline{S}_T$ and $\overline{S}_F$ increase. However, since fluid fiction irreversibility is more sensitive than the thermal dissipation to any alteration in *Ra*, the average Bejan number drops immensely. It can be seen that, at $Ra = 10^4$, the value of the $\overline{Be}$ is greater than half, which indicates that total entropy generation ($\overline{S}_{tot}$) is more influenced by $\overline{S}_T$ rather than viscous

dissipation ($\overline{S}_{tot} \approx \overline{S}_T$). This conjecture is well reflected in Fig. 20 where the variations of $\overline{S}_{tot}$ have the same pattern of alteration with $\overline{S}_T$. As Rayleigh number approaches the flow-transition value ($Ra = 10^5$), the fluid flow becomes stronger and consequently the contribution of $\overline{S}_F$ to $\overline{S}_{tot}$ is invigorated dramatically so that total entropy generation begins to follow the transient behavior of the fluid friction irreversibility ($\overline{S}_{tot} \approx \overline{S}_F$). This enhancement mechanism also manifests itself in form of the decreasing trend in the profiles of average Bejan number in both cavities. It can be seen that the degradation in the values of $\overline{Be}$ is accelerated and intensified as the flow enters into the convection-dominated regime ($Ra \geq 10^6$).

However, before closing this section, there are some other interesting points that can be drawn from Fig. 20. It is apparent that, at low Rayleigh number ($Ra = 10^4$), the aforementioned pertinent parameters tend to reach the constant value with the small-amplitude fluctuation around the state of equilibrium while, at high Rayleigh numbers (particularly beyond the critical value of $Ra_{Critical} = 5200$), the oscillatory behavior starts to emerge in their profiles [29]. This physical behavior can be attributed to the strong interaction between hot and cold fluids at high *Ra* which causes the induction of high-frequency internal waves and hydraulic jump in the velocity and temperature fields. These observations are in accordance with numerical findings of Magherbi et al. [29] and Schladow [114] who discussed that for $Ra_{Critical} < Ra$, when the initial condition is somewhat far from the equilibrium state, fluid flow and heat transfer are likely to undergo nonlinear oscillation around the steady-state condition. Another interesting feature is that in both cavities due to assigning zero-temperature initial condition ($\theta = 0$), the average Nusselt number along the hot and cold walls decreases and increases asymptotically and reaches the identical value which implies that the amount of the heat released from the hot surface is totally absorbed

by the cold wall which in turn demonstrates the accuracy of the proposed model from the first law of thermodynamics viewpoint. Finally, as pointed up earlier, by increasing the Rayleigh number from 10^6 to 10^7, the flow pattern in the Rayleigh-Bénard Convection (RBC) is evolved directly from the unicellular steady regime to the multi-cellular oscillatory solution. This mechanism is also accompanied by the formation of a symmetry/asymmetry *Hopf* bifurcation structure (Pitchfork bifurcation) [115,116] and vortex breakdown which leads to the striking fluctuations in the heat transfer rate within the enclosure. To bring this point out more clearly, the enlarged view of time-distributions of $\overline{Nu}$ with associated streamlines and isotherms snapshots are re-plotted in Fig. 21. The weakly turbulent flow at $Ra=10^7$ manifests itself through the emergence of semi-periodic thermal plumes and unsteady minor vortices. It is evident that during the advection process ($0 \le t \le 0.8$), the direction and position of the flow circulation and travelling wave are constantly changing (and internally displaced towards the downstream and upstream end walls) within the enclosure, meaning that the internal waves and perturbations generated by the initial conditions cannot be suppressed by the boundary layer. Figure 22 shows the comparison of the predicted results with numerical outcomes of Das et al. [109], for the case of Differentially Heated Cavity with internal conductive obstacle ($K_r = 0.2$ and $L = 0.5H$). It is apparent that the obtained results in terms of streamlines, isotherms and average Nusselt number are in excellent agreement with previously published data.

4. Conclusion

In this study, a modified version of the Volume-Of-Fluid model was introduced for simulation of multiphase and free-surface flows with high density contrast. To circumvent the difficulties regarding the physical discontinuities at the material interface, a novel third-order bounded flux-

limiter function was first constructed based on the TVD constraints and then employed for discretization of the convection terms in the momentum, energy and volume fraction equations. To further enhance the performance of the proposed model, the classical PISO algorithm was first modified based on the Two-step projection (PISOC) method and then was used for the treatment of the velocity-pressure coupling. To deal with the surface tension at the interface, the procedure for implementing the ELVIRA technique was first described in detail and then adopted to calculate the interface normal vector and its corresponding curvature. The accuracy and robustness of the improved VOF model were verified against eight different canonical test cases including: dam break, Rayleigh-Taylor instability, bubble rising, rotation of a slotted disk (Zalesak's problem), deformation of a 2D disk, pure convection of a step profile and transient entropy generation due to conjugate natural convection heat transfer in square enclosures. Based on the obtained results, the main conclusions of present study can be summarized as follows:

- It was found that, the newly proposed bounded convection scheme can successfully suppress false diffusion error and maintain sharpness of the interface.
- The results revealed that, the proposed non-linear flux-limiter function can successfully control and maintain the thickness of the interface to a maximum of 2-3 grid stencils.
- It was found that, the combination of the two classical PISO and Two-step projection method (PISOC) ensures that the mixed velocity in the vicinity of the material discontinuity is free of spurious spatial oscillations.
- It was found that, the proposed PISOC algorithm can effectively accelerate the convergence rate of numerical solution without introducing unphysical pressure fluctuations.

- It was found that the newly developed semi-iterative hybrid PISOC algorithm is robust and consistent with superior convergence characteristics to the standard iterative PISO algorithm.
- It was shown that, the enhanced VOF model can robustly handle large topological changes of complex multiphase flows involving interface rupture and coalescence.
- It was mathematically shown that, the ELVIRA technique can exactly reproduce any arbitrary linear interfaces.
- The results revealed that, the improved VOF model outperformed the existent conventional VOF method available in the OpenFoam® platform.
- The results revealed that, from the Entropy Generation Minimization (EGM) and optimal design viewpoints, the Differentially Heated Cavity (DHC) outperformed the Rayleigh-Bénard Convection (RBC) in terms of the highest heat transfer rate and lowest rate of entropy generation.

Acknowledgments

This work is financially supported by the Merit scholarship program for foreign students (PBEEE) of the Ministère de l'Éducation et de l'Enseignement supérieur du Québec (MEES) (Grant No. 263222), (Programme V1-Groupe: G2-20431).

Conflict of interest

The authors declared that there is no conflict of interest.

Supplementary material

For more details about the transient flow patterns in all simulated cases please refers to animations 1 to 14 in supplementary material.

Appendix A (Combination of the PISO and Two-step projection algorithms for the treatment of the pressure-velocity coupling)

Along this Appendix, a novel implicit pressure-based numerical algorithm is introduced using the combination of the classical PISO algorithm [117] and Two-step projection (Chorin's model) [118] method, aiming to obtain a robust and consistent unsteady state solver for modeling multiphase flows with complex topology changes on the staggered grid arrangement. Fundamentally speaking, the concept of the Two-step projection method and PISO algorithm is to establish a Pressure-Poisson equation by enforcing the velocity-divergence-free condition over each computational grid to satisfy the requirement for continuity equation. As shown in Fig. 2, in the staggered grid system, all scalar quantities (i.e. pressure, temperature, viscosity, density, volume fraction, etc) are located at nodes inside each cell while velocity components are sited on the cell faces. As stated in section 2, the convection terms in the present work are treated by means of the newly developed third-order TVD bounded scheme whereas the second-order central differencing scheme is employed for the approximation of the diffusion terms. Meanwhile, the pressure gradient term is estimated using the linear interpolation between the two immediate nodes sited on the momentum cell faces. The algebraic system of equations resulting from this integration process can be written as follows:

$$a_{ip}\mathbf{u}_p = \sum a_{np}\mathbf{u}_{np} + S_u + S_t - A_p(p_p - p_{np}) \tag{A1}$$

where the subscript *nb* denotes the neighboring velocity nodes and S_u represents the volumetric source term which would be the surface tension force ($S_u = F_{ST}\Delta x\Delta y$), gravitational force ($S_u = \rho\mathbf{g}\Delta x\Delta y$) or buoyancy force ($S_u = Ra\,\mathrm{Pr}\,\Delta x\Delta y$) in the present study. The parameter a_{ip} involves the implicit representation of the convection and diffusion variables together with the

transient term of $\partial\rho\mathbf{u}/\partial t$. It should be noted that, in order to further enhance the accuracy and performance of the numerical solution, the second-order implicit backward scheme proposed by Kim et al. [119] is employed in the current work for time discretization as:

$$\frac{\partial\rho\mathbf{u}}{\partial t}=\frac{3(\rho\mathbf{u})_p^{n+1}-4(\rho\mathbf{u})_p^{n}+(\rho\mathbf{u})_p^{n-1}}{2\Delta t} \tag{A2}$$

By incorporating the term arising from temporal discretization into Eq. (A1), the central coefficient a_{ip} and source term S_t for unsteady flow take the form:

$$a_{ip}=a_p+\frac{3\rho_p^{n+1}}{2\Delta t}\Delta x\Delta y \tag{A3}$$

$$S_t=\frac{4(\rho\mathbf{u})_p^{n}-(\rho\mathbf{u})_p^{n-1}}{2\Delta t}\Delta x\Delta y \tag{A4}$$

where a_p is the central coefficient associated with the steady-state formulation (see Eq. (28)). To start the PISOC algorithm, the initial guessed value of $\mathbf{u}^*$ is used for velocity components. Ideally, the discretized momentum equations based on the guessed velocity fields and correct pressure field (p^{n+1}) can produce the correct velocity fields as [83]:

$$\mathbf{u}_p^{n+1}=\frac{\sum a_{np}\mathbf{u}_{np}^{*}+S_u+S_t}{a_{ip}}-\frac{A_p(p_p^{n+1}-p_{np}^{n+1})}{a_{ip}} \tag{A5}$$

By introducing the intermediate velocity field ($\mathbf{u}$) without the pressure gradient term, the first part of the algorithm related to the Chorin's model (two-step projection model) can be accomplished as [120]:

$$\mathbf{u}=\frac{\sum a_{np}\mathbf{u}_{np}^{*}+S_u+S_t}{a_{ip}} \tag{A6}$$

$$\mathbf{u}_p^{n+1}=\mathbf{u}-\frac{2d_{ip}\nabla p^{n+1}}{3} \tag{A7}$$

where $d_{ip} = A_p / a_{ip}$. By taking the divergence on both sides of Eq. (A7) ($\nabla \cdot \mathbf{u}_p^{n+1} = \nabla \cdot \mathbf{u} - \nabla \cdot (2 d_{ip} \nabla p^{n+1} / 3)$) and substituting it into the discretized continuity equation, the following partial differential equation for the pressure can be obtained [121]:

$$\nabla d_{ip} \nabla p^{n+1} = \frac{3 \nabla \cdot \mathbf{u}}{2} - \frac{3}{2} \left(\frac{3\rho_p^{n+1} - 4\rho_p^{n} + \rho_p^{n-1}}{2\Delta t \rho_p^{n+1}} \right) \tag{A8}$$

The integration of Eq. (A8) over the computational domain yields:

$$\begin{aligned} & a_{i,j} P_{i,j}^{n+1} = a_{i+1,j} P_{i+1,j}^{n+1} + a_{i-1,j} P_{i-1,j}^{n+1} + a_{i,j+1} P_{i,j+1}^{n+1} + a_{i,j-1} P_{i,j-1}^{n+1} + \frac{3}{2} b_{i,j} - \frac{3}{2} \left(\frac{3\rho_p^{n+1} - 4\rho_p^{n} + \rho_p^{n-1}}{2\Delta t \rho_p^{n+1}} \Delta x \Delta y \right) \\ & a_{i,j} = a_{i+1,j} + a_{i-1,j} + a_{i,j+1} + a_{i,j-1} \\ & a_{i+1,j} = d_{i+1,j} \Delta y, \quad a_{i-1,j} = d_{i,j} \Delta y \\ & a_{i,j+1} = d_{i,j+1} \Delta x, \quad a_{i,j-1} = d_{i,j} \Delta x \\ & b_{i,j} = u_{i,j} \Delta y - u_{i+1,j} \Delta y + \hat{v}_{i,j} \Delta x - \hat{v}_{i,j+1} \Delta x \end{aligned} \tag{A9}$$

where $b_{i,j}$ represents the mass imbalance arising from the incorrect velocity field. Having determined the pressure field, the auxiliary velocity field can be modified using Eq. (A7). It should be noted that, although the present algorithm is non-iterative in nature, but for the strongly coupled nonlinear multiphase flows or Fluid-Structure Interaction (FSI) problems, the minimum number of ten iterations may be needed to achieve a specific error with known confidence levels of accuracy for pressure and velocity fields (similar to the classical two-step projection model). However, contrary to the iterative version of the PISO-algorithm, in order to reduce the computation cost, the iteration process can only be applied on Eq. (A9) instead of extending it to the whole algorithm. To proceed, one can assume that the pressure and velocity fields obtained from Eqs. (A7) and (A9) still cannot ensure the continuity condition after one or a prescribed number of iterations. As a result, the superscript on the pressure and velocity variables

is changed from (p^{n+1}, u^{n+1}) to (p^{*}, u^{**}). By substituting the semi-corrected values of p^{*} and u^{**} into the momentum equation (Eq. (A1)), the new velocity field ($\mathbf{u}^{**}$) can be obtained as:

$$a_{ip}\mathbf{u}_p^{**} = \sum a_{np}\mathbf{u}_{np}^{**} + S_u + S_t - A_p(p_p^{*} - p_{np}^{*}) \tag{A10}$$

By subtracting Eq. (A10) from (A1) and defining the incremental pressure (p') and velocity variables ($\mathbf{u}'$) as the difference between semi-corrected and true values, the following relationship can be derived:

$$a_{ip}(\mathbf{u}_p - \mathbf{u}_p^{**}) = \sum a_{np}(\mathbf{u}_{np} - \mathbf{u}_{np}^{**}) - A_p\nabla[(p_p - p_p^{*}) - (p_{np} - p_{np}^{*})] \tag{A11}$$

$$p = p^{*} + p' \tag{A12}$$

$$\mathbf{u} = \mathbf{u}^{**} + \mathbf{u}'$$

$$a_{ip}(\mathbf{u}'_p) = -A_p\nabla(p'_p - p'_{np}) \tag{A13}$$

$$\mathbf{u} = \mathbf{u}^{**} + \mathbf{u}'_p = \mathbf{u}^{**} - \frac{A_p\nabla(p'_p - p'_{np})}{a_{ip}} \tag{A14}$$

Note that, similar to the standard SIMPLE algorithm, the summation over the neighboring grid points is dropped here for simplicity ($\sum a_{np}(\mathbf{u}_{np} - \mathbf{u}_{np}^{*}) = \sum a_{np}(\mathbf{u}'_{np}) \approx 0$). Substituting Eq. (A14) into the discretized continuity equation yields the first system of discrete pressure-correction equation as:

$$a_{i,j}P'_{i,j} = a_{i+1,j}P'_{i+1,j} + a_{i-1,j}P'_{i-1,j} + a_{i,j+1}P'_{i,j+1} + a_{i,j-1}P'_{i,j-1} + b_{i,j} - \frac{3\rho_p^{n+1} - 4\rho_p^{n} + \rho_p^{n-1}}{2\Delta t\,\rho_p^{n+1}}\Delta x\Delta y \tag{A15}$$

$$\begin{aligned} &a_{i,j} = a_{i+1,j} + a_{i-1,j} + a_{i,j+1} + a_{i,j-1} \\ &a_{i+1,j} = d_{i+1,j}\Delta y, \quad a_{i-1,j} = d_{i,j}\Delta y \\ &a_{i,j+1} = d_{i,j+1}\Delta x, \quad a_{i,j-1} = d_{i,j}\Delta x \\ &b_{i,j} = u_{i,j}^{**}\Delta y - u_{i+1,j}^{**}\Delta y + \tilde{v}_{i,j}^{**}\Delta x - \tilde{v}_{i,j+1}^{**}\Delta x \end{aligned} \tag{A16}$$

Once the pressure correction field is known, the correct velocity and pressure fields can be calculated via Eqs. (A12) and (A14) as:

$$p = p^{*} + \alpha_{p1} p'$$
$$\mathbf{u} = \mathbf{u}^{**} - \frac{A_p \nabla (p'_p - p'_{np})}{a_{ip}} \tag{A17}$$

In the above equation, α_{p1} stands for the under-relaxation factor which is set as unity in the present study. However, to further enhance mass conservation within each computational grid at the current time step, once again it is assumed that the improved velocity (**u**) and pressure (p) fields are not necessarily divergence free and consequently cannot satisfy the conservation of mass rigorously. Hence, before advancing to the next time level ($n+1$), the second pressure-correction step as a main part of the classical non-iterative PISO scheme is required to achieve a satisfactory degree of accuracy. To accomplish this, the superscripts of the thrice-corrected velocity and pressure fields in Eq. (A17) are altered from $\mathbf{u} \to \mathbf{u}^{***}$ and $p \to p^{**}$. Similar to the previous stage, by substituting the updated velocity and pressure distributions into the momentum equation, the second semi-corrected velocity components ($\mathbf{u}^{***}$) can be obtained as:

$$\mathbf{u}_p^{***} = \frac{\sum a_{np} \mathbf{u}_{np}^{***} + S_u + S_t}{a_{ip}} - \frac{A_p (p_p^{**} - p_{np}^{**})}{a_{ip}} \tag{A18}$$

It is worth to mention that, contrary to the original PISO algorithm, due to the use of modified velocity and pressure values in the momentum equation, the central (a_{ip}) and neighbor (a_{np}) coefficients in Eq. (A10) are replaced by the updated coefficients a_{ip} and a_{np} in Eq. (A18). Our results have revealed that, although this modification is minor but it has a remarkable influence on the stability and performance of the numerical solutions. To terminate the algorithm, it is assumed that the correct pressure field (p^{n+1}) with the aid of the newly improved velocity field ($\mathbf{u}^{***}$) can ultimately satisfy the continuity constraint given by:

$$\mathbf{u}^{n+1} = \frac{\sum a_{np}\mathbf{u}_{np}^{***} + S_u + S_t}{a_{ip}} - \frac{A_p(p_p^{n+1} - p_{np}^{n+1})}{a_{ip}} \tag{A19}$$

By subtracting Eq. (A19) from (A18) and defining the second incremental pressure variable (p''), the following equations can be derived:

$$\mathbf{u}^{n+1} - \mathbf{u}_p^{***} = \frac{\sum a_{np}\mathbf{u}_{np}^{***} + S_u + S_t}{a_{ip}} - \frac{\sum a_{np}\mathbf{u}_{np}^{***} + S_u + S_t}{a_{ip}} - \frac{A_p(p_p^{n+1} - p_{np}^{n+1})}{a_{ip}} + \frac{A_p(p_p^{**} - p_{np}^{**})}{a_{ip}} \tag{A20}$$

$$p^{n+1} = p^{**} + \alpha_{p2}p'' \tag{A21}$$

$$\mathbf{u}^{n+1} = \mathbf{u}_p^{***} + \frac{\sum a_{np}(\mathbf{u}_{np}^{***} - \mathbf{u}_{np}^{***})}{a_{ip}} - \frac{A_p(p_p'' - p_{np}'')}{a_{ip}} \tag{A22}$$

where α_{p2} represents the second under-relaxation factor which is taken as unity. Substitution of $\mathbf{u}^{n+1}$ in the discretized continuity equation yields the second incremental pressure equation as:

$$a_{i,j}P_{i,j}'' = a_{i+1,j}P_{i+1,j}'' + a_{i-1,j}P_{i-1,j}'' + a_{i,j+1}P_{i,j+1}'' + a_{i,j-1}P_{i,j-1}'' + \tilde{b}_{i,j} + \tilde{\tilde{b}}_{i,j} - \frac{3\rho_p^{n+1} - 4\rho_p^n + \rho_p^{n-1}}{2\Delta t\rho_p^{n+1}}\Delta x\Delta y \tag{A23}$$

$$\begin{aligned}
&a_{i,j} = a_{i+1,j} + a_{i-1,j} + a_{i,j+1} + a_{i,j-1} \\
&a_{i+1,j} = d_{i+1,j}\Delta y, \quad a_{i-1,j} = d_{i,j}\Delta y \\
&a_{i,j+1} = d_{i,j+1}\Delta x, \quad a_{i,j-1} = d_{i,j}\Delta x \\
&\tilde{b}_{i,j} = u_{i,j}^{***}\Delta y - u_{i+1,j}^{***}\Delta y + \tilde{v}_{i,j}^{***}\Delta x - \tilde{v}_{i,j+1}^{***}\Delta x \\
&\tilde{\tilde{b}}_{i,j} = \left(\frac{\sum a_{np}(u_{np}^{***} - u_{np}^{***})}{a_{ip}}\right)_{i,j}\Delta y - \frac{\sum a_{np}(u_{np}^{***} - u_{np}^{***})}{a_{ip}}\Big)_{i+1,j}\Delta y \\
&+ \frac{\sum \widetilde{a_{np}(v_{np}^{***} - v_{np}^{***})}}{\widetilde{a_{ip}}}\Big)_{i,j}\Delta x - \frac{\sum \widetilde{a_{np}(\mathbf{u}_{np}^{***} - \mathbf{u}_{np}^{***})}}{\widetilde{a_{ip}}}\Big)_{i,j+1}\Delta x
\end{aligned} \tag{A24}$$

Once the second pressure correction equation is solved, the exact velocity and pressure distributions can be calculated through Eqs. (A21) and (A22). Having computed the correct velocity field, the volume fraction and energy transport equations are solved and calculation is then transferred to the next time step where the updated physical quantities will be used as an initial guess of the solution in the next level. However, before ending this subsection, it is

necessary to point out that, in the standard PISO-algorithm, Issa [117] ideally assumed that the twice-improved velocity field ($\mathbf{u}^{***}$) appeared as a source term on the right hand side of Eq. (A24) is sufficiently accurate to satisfy the zero-divergence condition ($\nabla\cdot\mathbf{u}^{***}=0, \tilde{b}_{i,j}=0$). However, our results have shown that this assumption is not necessarily valid so that the strict enforcement of the continuity constraint via the direct imposition of $\nabla\cdot\mathbf{u}^{***}=0$ (or $\tilde{b}_{i,j}=0$) in Eq. (A24) can lead to spurious pressure oscillation especially in the multiphase flows problems where grid-to-flow skewness is large and fluid flow is governed by convection.

References

[1] N. Zhao, J. Yang, H. Li, Z. Zhang, S. Li, Numerical investigations of laminar heat transfer and flow performance of Al2O3-water nanofluids in a flat tube, Int. J. Heat Mass Transf. 92 (2016) 268–282. doi:10.1016/j.ijheatmasstransfer.2015.08.098.

[2] M. Chakkingal, S. Kenjereš, I. Ataei-Dadavi, M.J. Tummers, C.R. Kleijn, Numerical analysis of natural convection with conjugate heat transfer in coarse-grained porous media, Int. J. Heat Fluid Flow. 77 (2019) 48–60.

[3] A.I. Alsabery, M.A. Sheremet, A.J. Chamkha, I. Hashim, Conjugate natural convection of Al2O3–water nanofluid in a square cavity with a concentric solid insert using Buongiorno's two-phase model, Int. J. Mech. Sci. 136 (2018) 200–219.

[4] M.J. Uddin, O.A. Bég, M.N. Uddin, Energy conversion under conjugate conduction, magneto-convection, diffusion and nonlinear radiation over a non-linearly stretching sheet with slip and multiple convective boundary conditions, Energy. 115 (2016) 1119–1129.

[5] S. Pandey, Y.G. Park, M.Y. Ha, An exhaustive review of studies on natural convection in enclosures with and without internal bodies of various shapes, Int. J. Heat Mass Transf. 138 (2019) 762–795.

[6] A. Amine, J.K. Platten, M. Hasnaoui, Thermal convection around obstacles: the case of Sierpinski carpets, Exp. Fluids. 36 (2004) 717–727.

[7] D.-D. Zhang, J.-H. Zhang, D. Liu, F.-Y. Zhao, H.-Q. Wang, X.-H. Li, Inverse conjugate heat conduction and natural convection inside an enclosure with multiple unknown wall heating fluxes, Int. J. Heat Mass Transf. 96 (2016) 312–329.

[8] Q. Ren, C.L. Chan, Natural convection with an array of solid obstacles in an enclosure by lattice Boltzmann method on a CUDA computation platform, Int. J. Heat Mass Transf. 93 (2016) 273–285.

[9] A. Raji, M. Hasnaoui, M. Naïmi, K. Slimani, M.T. Ouazzani, Effect of the subdivision of an obstacle on the natural convection heat transfer in a square cavity, Comput. Fluids. 68 (2012) 1–15.

[10] F. Garoosi, F. Talebi, Numerical simulation of conjugate conduction and natural convection heat transfer of nanofluid inside a square enclosure containing a conductive partition and several disconnected conducting solid blocks using the Buongiorno's two phase model, Powder Technol. 317 (2017) 48–71.

[11] F. Garoosi, M.M. Rashidi, Two phase flow simulation of conjugate natural convection of the nanofluid in a partitioned heat exchanger containing several conducting obstacles, Int. J. Mech. Sci. 130 (2017) 282–306.

[12] J.-T. Hu, X.-H. Ren, D. Liu, F.-Y. Zhao, H.-Q. Wang, Conjugate natural convection inside a vertical enclosure with solid obstacles of unique volume and multiple morphologies, Int. J. Heat Mass Transf. 95 (2016) 1096–1114.

[13] I. V Miroshnichenko, M.A. Sheremet, Radiation effect on conjugate turbulent natural convection in a cavity with a discrete heater, Appl. Math. Comput. 321 (2018) 358–371.

[14] F. Selimefendigil, H.F. Öztop, Conjugate natural convection in a nanofluid filled partitioned horizontal annulus formed by two isothermal cylinder surfaces under magnetic field, Int. J. Heat Mass Transf. 108 (2017) 156–171.

[15] L. Wang, Y. Zhao, X. Yang, B. Shi, Z. Chai, A lattice Boltzmann analysis of the conjugate natural convection in a square enclosure with a circular cylinder, Appl. Math. Model. 71 (2019) 31–44.

[16] H. Zargartalebi, M. Ghalambaz, K. Khanafer, I. Pop, Unsteady conjugate natural convection in a porous cavity boarded by two vertical finite thickness walls, Int. Commun. Heat Mass Transf. 81 (2017) 218–228.

[17] G. De Vahl Davis, Natural convection of air in a square cavity: A bench mark numerical solution, Int. J. Numer. Methods Fluids. 3 (1983) 249–264. doi:10.1002/fld.1650030305.

[18] P.H. Kao, R.J. Yang, Simulating oscillatory flows in Rayleigh-Bénard convection using the lattice Boltzmann method, Int. J. Heat Mass Transf. 50 (2007) 3315–3328. doi:10.1016/j.ijheatmasstransfer.2007.01.035.

[19] K. Kalidasan, R. Velkennedy, P.R. Kanna, Laminar natural convection of Copper-Titania/Water hybrid nanofluid in an open ended C-shaped enclosure with an isothermal block, J. Mol. Liq. 246 (2017) 251–258.

[20] A. Rahimi, A.D. Saee, A. Baghban, A. Kasaeipoor, H. Ashrafi, E.H. Malekshah, Double-MRT lattice Boltzmann simulation of natural convection in a C-shaped heat exchanger, Powder Technol. 336 (2018) 465–480.

[21] N. Makulati, A. Kasaeipoor, M.M. Rashidi, Numerical study of natural convection of a water–alumina nanofluid in inclined C-shaped enclosures under the effect of magnetic field, Adv. Powder Technol. 27 (2016) 661–672.

[22] B. Mliki, M.A. Abbassi, A. Omri, Z. Belkacem, Lattice Boltzmann analysis of MHD natural convection of CuO-water nanofluid in inclined C-shaped enclosures under the effect of nanoparticles Brownian motion, Powder Technol. 308 (2017) 70–83.

[23] A. Bejan, Entropy generation through heat and fluid flow, Wiley, 1982.

[24] A. Bejan, Entropy generation minimization: The new thermodynamics of finite-size devices and finite-time processes, J. Appl. Phys. 79 (1996) 1191–1218.

[25] A.A.A.A. Al-Rashed, Investigating the effect of alumina nanoparticles on heat transfer and entropy generation inside a square enclosure equipped with two inclined blades under magnetic field, Int. J. Mech. Sci. 152 (2019) 312–328.

[26] A.H. Pordanjani, S. Aghakhani, A.A. Alnaqi, M. Afrand, Effect of alumina nano-powder on the convection and the entropy generation of water inside an inclined square cavity subjected to a magnetic field: Uniform and non-uniform temperature boundary conditions, Int. J. Mech. Sci. 152 (2019) 99–117.

[27] T.A. Alkanhal, M. Sheikholeslami, A. Arabkoohsar, R. ul Haq, A. Shafee, Z. Li, I. Tlili, Simulation of convection heat transfer of magnetic nanoparticles including entropy generation using CVFEM, Int. J. Heat Mass Transf. 136 (2019) 146–156. doi:10.1016/j.ijheatmasstransfer.2019.02.095.

[28] C. Sivaraj, M.A. Sheremet, MHD natural convection and entropy generation of ferrofluids in a cavity with a non-uniformly heated horizontal plate, Int. J. Mech. Sci. 149 (2018) 326–337.

[29] M. Magherbi, H. Abbassi, A. Ben Brahim, Entropy generation at the onset of natural convection, Int. J. Heat Mass Transf. 46 (2003) 3441–3450.

[30] D. Das, M. Roy, T. Basak, Studies on natural convection within enclosures of various (non-square) shapes–A review, Int. J. Heat Mass Transf. 106 (2017) 356–406.

[31] P. Biswal, T. Basak, Entropy generation vs energy efficiency for natural convection based energy flow in enclosures and various applications: A review, Renew. Sustain. Energy Rev. 80 (2017) 1412–1457. doi:10.1016/j.rser.2017.04.070.

[32] W. Duan, Y. Gao, Q. Yu, T. Wu, Z. Wang, Numerical simulation of coal gasification in molten slag: Gas-liquid interaction characteristic, Energy. 183 (2019) 1233–1243.

[33] X. Li, M. Liu, Y. Ma, T. Dong, D. Yao, Experiments and meso-scale modeling of phase holdups and bubble behavior in gas-liquid-solid mini-fluidized beds, Chem. Eng. Sci. 192 (2018) 725–738.

[34] A. Tschöpe, M. Wyrwoll, M. Schneider, K. Mandel, M. Franzreb, A Magnetically Induced Fluidized-bed Reactor for Intensification of Electrochemical Reactions, Chem. Eng. J. (2019) 123845.

[35] T. Wang, T. Tang, Q. Gao, Z. Yuan, Y. He, Experimental and numerical investigations on the particle behaviours in a bubbling fluidized bed with binary solids, Powder Technol.

362 (2020) 436–449.

[36] J. Yan, W. Yan, S. Lin, G.J. Wagner, A fully coupled finite element formulation for liquid–solid–gas thermo-fluid flow with melting and solidification, Comput. Methods Appl. Mech. Eng. 336 (2018) 444–470.

[37] J. Zhao, W. Liu, J. Zhao, L. Grekhov, Numerical investigation of gas/liquid two-phase flow in nozzle holes considering the fuel compressibility, Int. J. Heat Mass Transf. 147 (2020) 118991.

[38] H. Ström, S. Sasic, O. Holm-Christensen, L.J. Shah, Atomizing industrial gas-liquid flows–development of an efficient hybrid vof-lpt numerical framework, Int. J. Heat Fluid Flow. 62 (2016) 104–113.

[39] F. Giussani, F. Piscaglia, G. Saez-Mischlich, J. Hèlie, A three-phase VOF solver for the simulation of in-nozzle cavitation effects on liquid atomization, J. Comput. Phys. (2019) 109068.

[40] J. Huang, X. Zhao, Numerical simulations of atomization and evaporation in liquid jet flows, Int. J. Multiph. Flow. 119 (2019) 180–193.

[41] Z. Wang, R. Chen, X. Zhu, Q. Liao, D. Ye, B. Zhang, X. He, L. Jiao, Dynamic behaviors of the coalescence between two droplets with different temperatures simulated by the VOF method, Appl. Therm. Eng. 131 (2018) 132–140.

[42] F. Yeganehdoust, R. Attarzadeh, I. Karimfazli, A. Dolatabadi, A numerical analysis of air entrapment during droplet impact on an immiscible liquid film, Int. J. Multiph. Flow. 124 (2020) 103175.

[43] G. Tryggvason, R. Scardovelli, S. Zaleski, Direct numerical simulations of gas–liquid multiphase flows, Cambridge University Press, 2011.

[44] C.W. Hirt, B.D. Nichols, Volume of fluid (VOF) method for the dynamics of free boundaries, J. Comput. Phys. 39 (1981) 201–225. doi:10.1016/0021-9991(81)90145-5.

[45] M. Sussman, P. Smereka, S. Osher, A level set approach for computing solutions to incompressible two-phase flow, J. Comput. Phys. 114 (1994) 146–159.

[46] G. Tryggvason, B. Bunner, A. Esmaeeli, D. Juric, N. Al-Rawahi, W. Tauber, J. Han, S. Nas, Y.-J. Jan, A front-tracking method for the computations of multiphase flow, J. Comput. Phys. 169 (2001) 708–759.

[47] M. Ishii, T. Hibiki, Thermo-fluid dynamics of two-phase flow, Springer Science & Business Media, 2010.

[48] I. Malgarinos, N. Nikolopoulos, M. Gavaises, Coupling a local adaptive grid refinement technique with an interface sharpening scheme for the simulation of two-phase flow and free-surface flows using VOF methodology, J. Comput. Phys. 300 (2015) 732–753.

[49] A. Issakhov, Y. Zhandaulet, A. Nogaeva, Numerical simulation of dam break flow for

various forms of the obstacle by VOF method, Int. J. Multiph. Flow. 109 (2018) 191–206.

[50] A. Issakhov, M. Imanberdiyeva, Numerical simulation of the movement of water surface of dam break flow by VOF methods for various obstacles, Int. J. Heat Mass Transf. 136 (2019) 1030–1051.

[51] Z.H. Gu, H.L. Wen, C.H. Yu, T.W.H. Sheu, Interface-preserving level set method for simulating dam-break flows, J. Comput. Phys. 374 (2018) 249–280.

[52] B.P. Leonard, Simple high-accuracy resolution program for convective modelling of discontinuities, Int. J. Numer. Methods Fluids. 8 (1988) 1291–1318.

[53] J.A. Heyns, A.G. Malan, T.M. Harms, O.F. Oxtoby, Development of a compressive surface capturing formulation for modelling free-surface flow by using the volume-of-fluid approach, Int. J. Numer. Methods Fluids. 71 (2013) 788–804.

[54] M.J. Berger, J. Oliger, Adaptive mesh refinement for hyperbolic partial differential equations, J. Comput. Phys. 53 (1984) 484–512.

[55] S. Hill, D. Deising, T. Acher, H. Klein, D. Bothe, H. Marschall, Boundedness-preserving implicit correction of mesh-induced errors for VOF based heat and mass transfer, J. Comput. Phys. 352 (2018) 285–300.

[56] F. Denner, B.G.M. van Wachem, Compressive VOF method with skewness correction to capture sharp interfaces on arbitrary meshes, J. Comput. Phys. 279 (2014) 127–144.

[57] K. Ling, W.-Q. Tao, A sharp-interface model coupling VOSET and IBM for simulations on melting and solidification, Comput. Fluids. 178 (2019) 113–131.

[58] X. Deng, S. Inaba, B. Xie, K.-M. Shyue, F. Xiao, High fidelity discontinuity-resolving reconstruction for compressible multiphase flows with moving interfaces, J. Comput. Phys. 371 (2018) 945–966.

[59] P. Das, H.S. Udaykumar, A sharp-interface method for the simulation of shock-induced vaporization of droplets, J. Comput. Phys. 405 (2020) 109005.

[60] M.A. Alves, P.J. Oliveira, F.T. Pinho, A convergent and universally bounded interpolation scheme for the treatment of advection, Int. J. Numer. Methods Fluids. 41 (2003) 47–75.

[61] S.K. Choi, H.Y. Nam, M. Cho, A comparison of higher-order bounded convection schemes, Comput. Methods Appl. Mech. Eng. 121 (1995) 281–301.

[62] G. Pozzetti, B. Peters, A multiscale DEM-VOF method for the simulation of three-phase flows, Int. J. Multiph. Flow. 99 (2018) 186–204.

[63] P. Cifani, W.R. Michalek, G.J.M. Priems, J.G.M. Kuerten, C.W.M. van der Geld, B.J. Geurts, A comparison between the surface compression method and an interface reconstruction method for the VOF approach, Comput. Fluids. 136 (2016) 421–435.

[64] V.-T. Nguyen, W.-G. Park, A volume-of-fluid (VOF) interface-sharpening method for two-phase incompressible flows, Comput. Fluids. 152 (2017) 104–119.

[65] V.-T. Nguyen, V.-D. Thang, W.-G. Park, A novel sharp interface capturing method for two-and three-phase incompressible flows, Comput. Fluids. 172 (2018) 147–161.

[66] K.K. So, X.Y. Hu, N.A. Adams, Anti-diffusion method for interface steepening in two-phase incompressible flow, J. Comput. Phys. 230 (2011) 5155–5177.

[67] M. Akhlaghi, V. Mohammadi, N.M. Nouri, M. Taherkhani, M. Karimi, Multi-Fluid VoF model assessment to simulate the horizontal air–water intermittent flow, Chem. Eng. Res. Des. 152 (2019) 48–59.

[68] J. Hua, D. Mortensen, A front tracking method for simulation of two-phase interfacial flows on adaptive unstructured meshes for complex geometries, Int. J. Multiph. Flow. 119 (2019) 166–179.

[69] H. Tan, An adaptive mesh refinement based flow simulation for free-surfaces in thermal inkjet technology, Int. J. Multiph. Flow. 82 (2016) 1–16.

[70] L.C. Ngo, H.G. Choi, A multi-level adaptive mesh refinement for an integrated finite element/level set formulation to simulate multiphase flows with surface tension, Comput. Math. with Appl. (2019).

[71] O. Antepara, N. Balcázar, J. Rigola, A. Oliva, Numerical study of rising bubbles with path instability using conservative level-set and adaptive mesh refinement, Comput. Fluids. 187 (2019) 83–97.

[72] X. Chen, V. Yang, Thickness-based adaptive mesh refinement methods for multi-phase flow simulations with thin regions, J. Comput. Phys. 269 (2014) 22–39.

[73] K. Schmidmayer, F. Petitpas, E. Daniel, Adaptive Mesh Refinement algorithm based on dual trees for cells and faces for multiphase compressible flows, J. Comput. Phys. 388 (2019) 252–278.

[74] H. Li, W.T. Leung, M.F. Wheeler, Sequential local mesh refinement solver with separate temporal and spatial adaptivity for non-linear two-phase flow problems, J. Comput. Phys. 403 (2020) 109074. doi:10.1016/j.jcp.2019.109074.

[75] D.J.E. Harvie, M.R. Davidson, M. Rudman, An analysis of parasitic current generation in volume of fluid simulations, Appl. Math. Model. 30 (2006) 1056–1066.

[76] E.G. Puckett, A.S. Almgren, J.B. Bell, D.L. Marcus, W.J. Rider, A high-order projection method for tracking fluid interfaces in variable density incompressible flows, J. Comput. Phys. 130 (1997) 269–282.

[77] O. Ubbink, R.I. Issa, A method for capturing sharp fluid interfaces on arbitrary meshes, J. Comput. Phys. 153 (1999) 26–50.

[78] G.Y. Soh, G.H. Yeoh, V. Timchenko, An algorithm to calculate interfacial area for multiphase mass transfer through the volume-of-fluid method, Int. J. Heat Mass Transf. 100 (2016) 573–581.

[79] J.U. Brackbill, D.B. Kothe, C. Zemach, A continuum method for modeling surface tension, J. Comput. Phys. 100 (1992) 335–354.

[80] A. Bejan, Convection heat transfer, John wiley & sons, 2013.

[81] D. Das, L. Lukose, T. Basak, Role of multiple discrete heaters to minimize entropy generation during natural convection in fluid filled square and triangular enclosures, Int. J. Heat Mass Transf. 127 (2018) 1290–1312.

[82] G.G. Ilis, M. Mobedi, B. Sunden, Effect of aspect ratio on entropy generation in a rectangular cavity with differentially heated vertical walls, Int. Commun. Heat Mass Transf. 35 (2008) 696–703.

[83] H.K. Versteeg, W. Malalasekera, An introduction to computational fluid dynamics: the finite volume method, Pearson Education, 2007.

[84] J.E. Pilliod Jr, E.G. Puckett, Second-order accurate volume-of-fluid algorithms for tracking material interfaces, J. Comput. Phys. 199 (2004) 465–502.

[85] P.K. Sweby, High resolution schemes using flux limiters for hyperbolic conservation laws, SIAM J. Numer. Anal. 21 (1984) 995–1011.

[86] M. Zijlema, On the construction of a third-order accurate monotone convection scheme with application to turbulent flows in general domains, Int. J. Numer. Methods Fluids. 22 (1996) 619–641.

[87] W. Gao, H. Li, Y. Liu, Y.-J. Jian, An oscillation-free high order TVD/CBC-based upwind scheme for convection discretization, Numer. Algorithms. 59 (2012) 29–50.

[88] N.P. Waterson, H. Deconinck, Design principles for bounded higher-order convection schemes–a unified approach, J. Comput. Phys. 224 (2007) 182–207.

[89] B. Van Leer, Towards the ultimate conservative difference scheme. II. Monotonicity and conservation combined in a second-order scheme, J. Comput. Phys. 14 (1974) 361–370.

[90] M.S. Darwish, F.H. Moukalled, Normalized variable and space formulation methodology for high-resolution schemes, Numer. Heat Transf. 26 (1994) 79–96.

[91] S. Bidadi, S.L. Rani, Quantification of numerical diffusivity due to TVD schemes in the advection equation, J. Comput. Phys. 261 (2014) 65–82.

[92] D.L. Youngs, Time-dependent multi-material flow with large fluid distortion, Numer. Methods Fluid Dyn. (1982).

[93] R. Scardovelli, S. Zaleski, Interface reconstruction with least-square fit and split Eulerian–Lagrangian advection, Int. J. Numer. Methods Fluids. 41 (2003) 251–274.

[94] X. Xu, X.-L. Deng, An improved weakly compressible SPH method for simulating free surface flows of viscous and viscoelastic fluids, Comput. Phys. Commun. 201 (2016) 43–62.

[95] X. Zheng, Q.W. Ma, W.Y. Duan, Incompressible SPH method based on Rankine source solution for violent water wave simulation, J. Comput. Phys. 276 (2014) 291–314.

[96] A. Colagrossi, M. Landrini, Numerical simulation of interfacial flows by smoothed particle hydrodynamics, J. Comput. Phys. 191 (2003) 448–475.

[97] M. Rezavand, C. Zhang, X. Hu, A weakly compressible SPH method for violent multi-phase flows with high density ratio, J. Comput. Phys. 402 (2020) 109092.

[98] G. Pahar, A. Dhar, Mixed miscible-immiscible fluid flow modelling with incompressible SPH framework, Eng. Anal. Bound. Elem. 73 (2016) 50–60.

[99] Y.L. Li, L. Wan, Y.H. Wang, C.P. Ma, L. Ren, Numerical investigation of interface capturing method by the Rayleigh-Taylor instability, dambreak and solitary wave problems, Ocean Eng. 194 (2019) 106583.

[100] X. He, S. Chen, R. Zhang, A lattice Boltzmann scheme for incompressible multiphase flow and its application in simulation of Rayleigh–Taylor instability, J. Comput. Phys. 152 (1999) 642–663.

[101] Y. Zhao, H.H. Tan, B. Zhang, A high-resolution characteristics-based implicit dual time-stepping VOF method for free surface flow simulation on unstructured grids, J. Comput. Phys. 183 (2002) 233–273.

[102] F. Denner, Wall collision of deformable bubbles in the creeping flow regime, Eur. J. Mech. 70 (2018) 36–45.

[103] M.M. Larimi, A. Ramiar, Two-dimensional bubble rising through quiescent and non-quiescent fluid: Influence on heat transfer and flow behavior, Int. J. Therm. Sci. 131 (2018) 58–71.

[104] S.T. Zalesak, Fully multidimensional flux-corrected transport algorithms for fluids, J. Comput. Phys. 31 (1979) 335–362.

[105] M. Owkes, O. Desjardins, A computational framework for conservative, three-dimensional, unsplit, geometric transport with application to the volume-of-fluid (VOF) method, J. Comput. Phys. 270 (2014) 587–612.

[106] M.-J. Li, Interaction between free surface flow and moving bodies with a dynamic mesh and interface geometric reconstruction approach, Comput. Math. with Appl. 81 (2021) 649–663.

[107] D. Zhang, C. Jiang, D. Liang, L. Cheng, A review on TVD schemes and a refined flux-limiter for steady-state calculations, J. Comput. Phys. 302 (2015) 114–154.

[108] N. Ouertatani, N. Ben Cheikh, B. Ben Beya, T. Lili, Numerical simulation of two-dimensional Rayleigh–Bénard convection in an enclosure, Comptes Rendus Mécanique. 336 (2008) 464–470.

[109] M.K. Das, K.S.K. Reddy, Conjugate natural convection heat transfer in an inclined square

cavity containing a conducting block, Int. J. Heat Mass Transf. 49 (2006) 4987–5000.

[110] J. Zhao, W. Cai, Y. Jiang, Study on frequency patterns of 2D square Rayleigh–Bénard convection filled with air, Eur. J. Mech. 74 (2019) 280–290.

[111] K.T. Yang, Transitions and bifurcations in laminar buoyant flows in confined enclosures, (1988).

[112] D. Mishra, K. Muralidhar, P. Munshi, Experimental study of Rayleigh–Benard convection at intermediate Rayleigh numbers using interferometric tomography, Fluid Dyn. Res. 25 (1999) 231.

[113] R. Anandalakshmi, T. Basak, Natural convection in rhombic enclosures with isothermally heated side or bottom wall: entropy generation analysis, Eur. J. Mech. 54 (2015) 27–44.

[114] S.G. Schladow, Oscillatory motion in a side-heated cavity, J. Fluid Mech. 213 (1990) 589–610.

[115] S.C. Saha, Y. Gu, Natural convection in a triangular enclosure heated from below and non-uniformly cooled from top, Int. J. Heat Mass Transf. 80 (2015) 529–538.

[116] Z. Alloui, P. Vasseur, M. Reggio, Natural convection of nanofluids in a shallow cavity heated from below, Int. J. Therm. Sci. 50 (2011) 385–393.

[117] R.I. Issa, Solution of the implicitly discretised fluid flow equations by operator-splitting, J. Comput. Phys. 62 (1986) 40–65.

[118] A.J. Chorin, Numerical solution of the Navier-Stokes equations, Math. Comput. 22 (1968) 745–762.

[119] S.-W. Kim, T.J. Benson, Comparison of the SMAC, PISO and iterative time-advancing schemes for unsteady flows, Comput. Fluids. 21 (1992) 435–454.

[120] Z. Nasri, A.H. Laatar, J. Balti, Natural convection enhancement in an asymmetrically heated channel-chimney system, Int. J. Therm. Sci. 90 (2015) 122–134.

[121] C. Varsakelis, M. V Papalexandris, A numerical method for two-phase flows of dense granular mixtures, J. Comput. Phys. 257 (2014) 737–756.

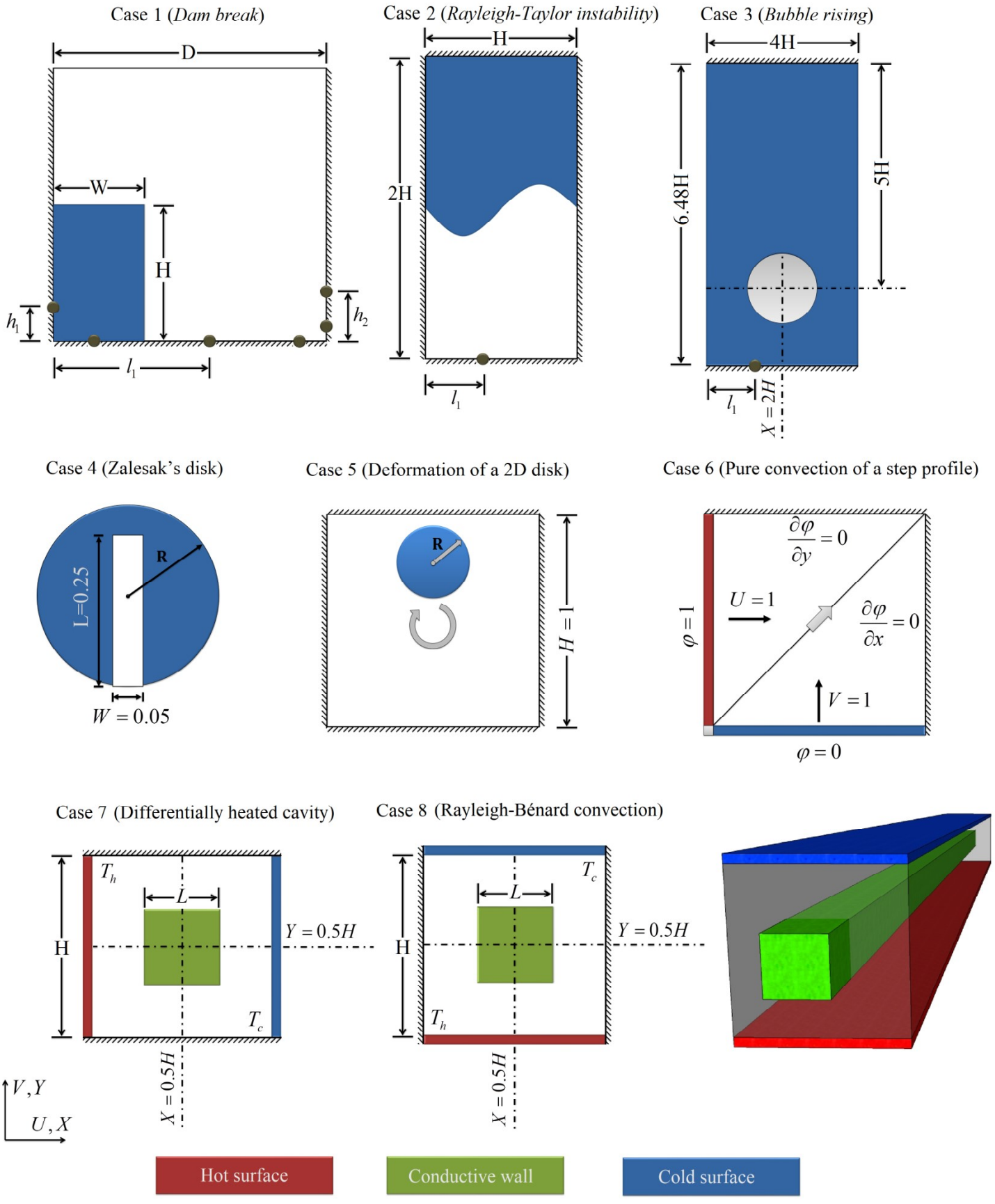

Fig. 1. Schematic diagram of eight different physical configurations under consideration with associated boundary conditions and coordinate system.

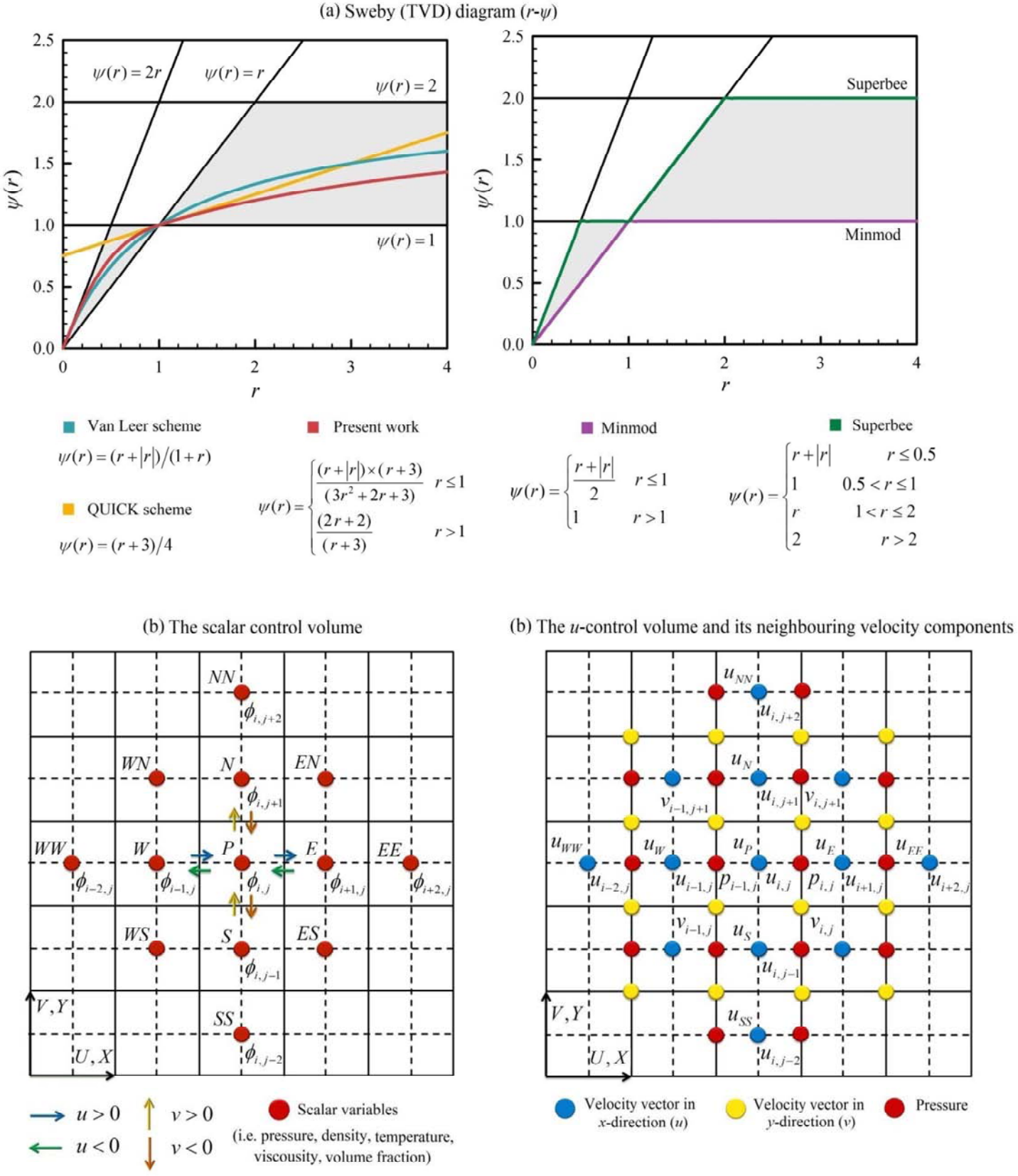

Fig. 2. (a) Sweby diagram showing the proposed model along with the four other well-known convection schemes (the shaded areas represent the the TVD region). (b) The 2D staggered grid arrangment used for discritisation of the governing equations where the scalar quantities (i.e. pressure) coincide with the cell faces of the *u*-control volume.

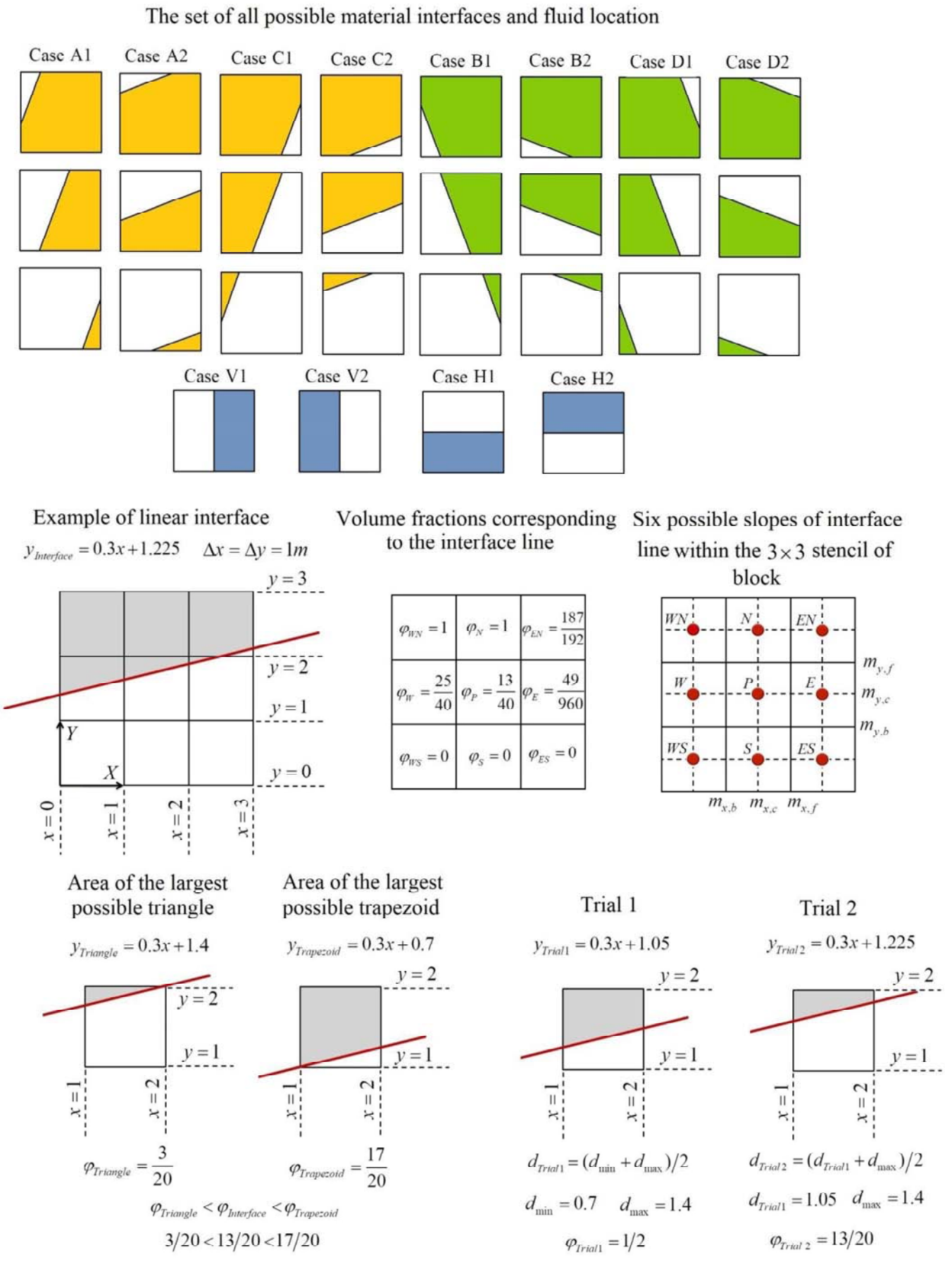

Fig. 3. Possible cases of interface orientation together with an example of interface reconstruction technique.

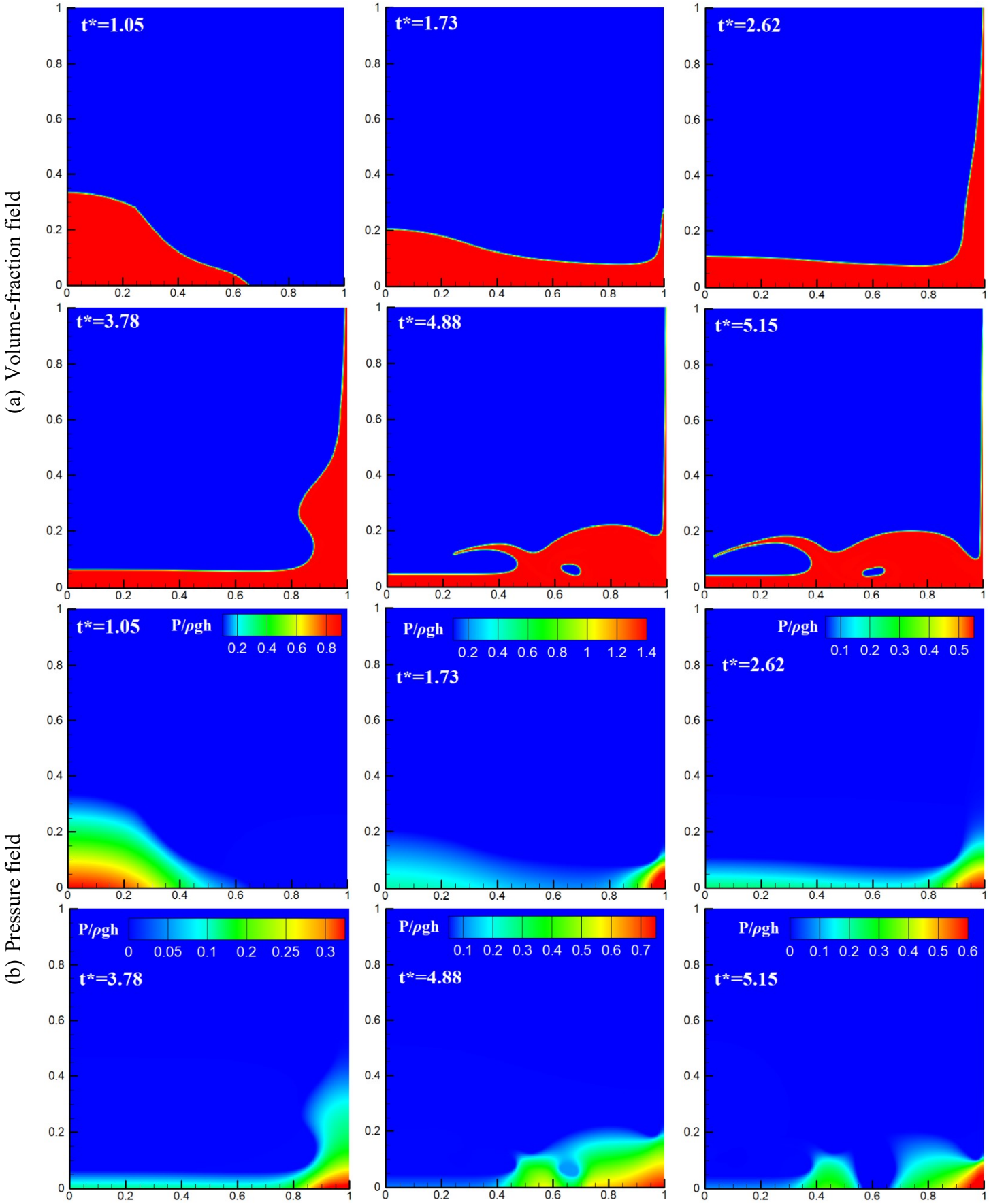

Fig. 4. Snapshots of the volume-fraction field and pressure contour with flow sequence identification simulated by the proposed model for case 1.

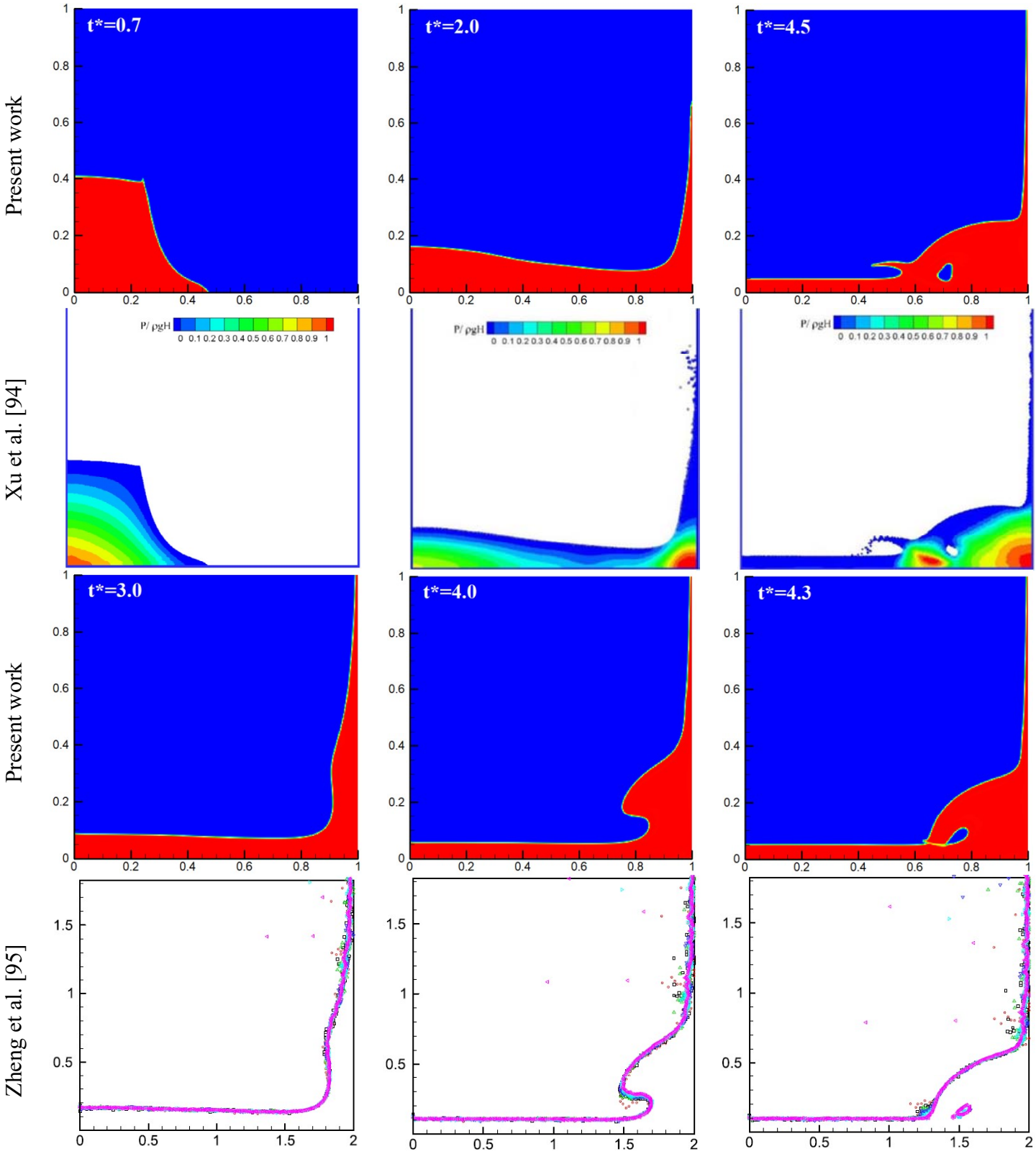

Fig. 5. Comparisons of the interfaces at different time instants between present work and numerical results of Xu et al. [94] and Zheng et al. [95].

(a) Zoomed-in views of free surface profile at three different time instants ($t^* = 4.0$, 4.5 and 5.15)

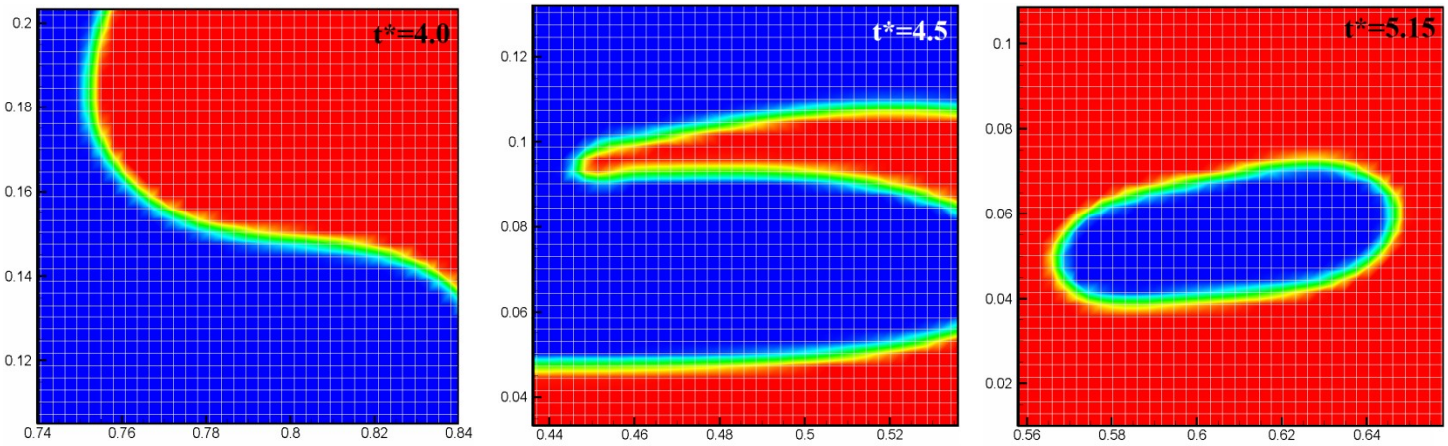

(b) Time histories of pressure variations on the left wall at h_1=0.05m

(c) Time histories of pressure variations on the right wall at h_2=0.025m

(d) Time histories of wave front position

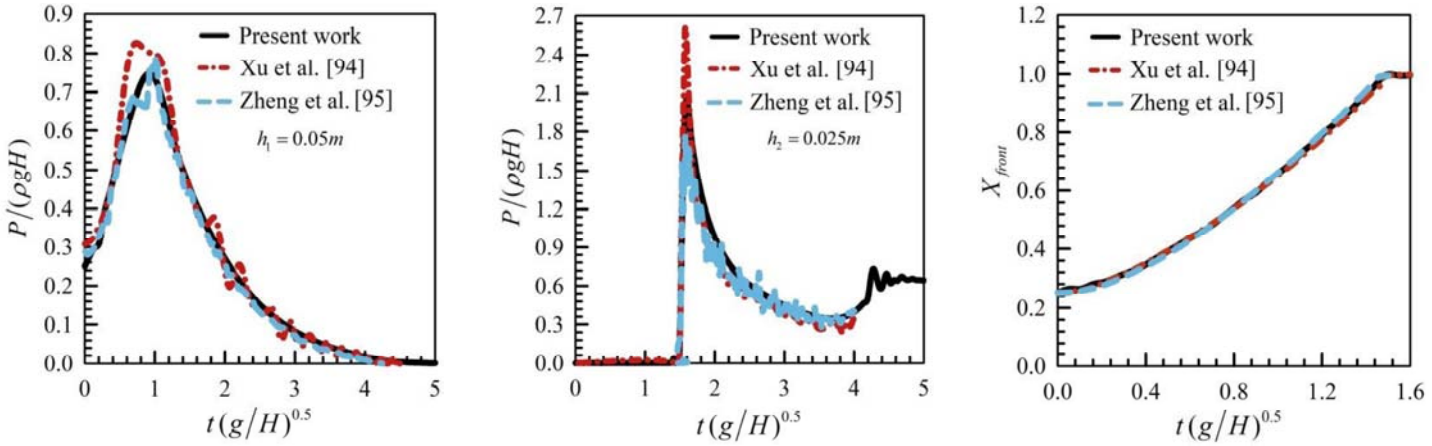

(e) Time histories of pressure signals on the left wall at h_1=0 and h_1=0.025m

(f) Time histories of pressure signals on the right wall at h_2=0 and h_2=0.05m

(g) Time histories of water column heights at three different sites

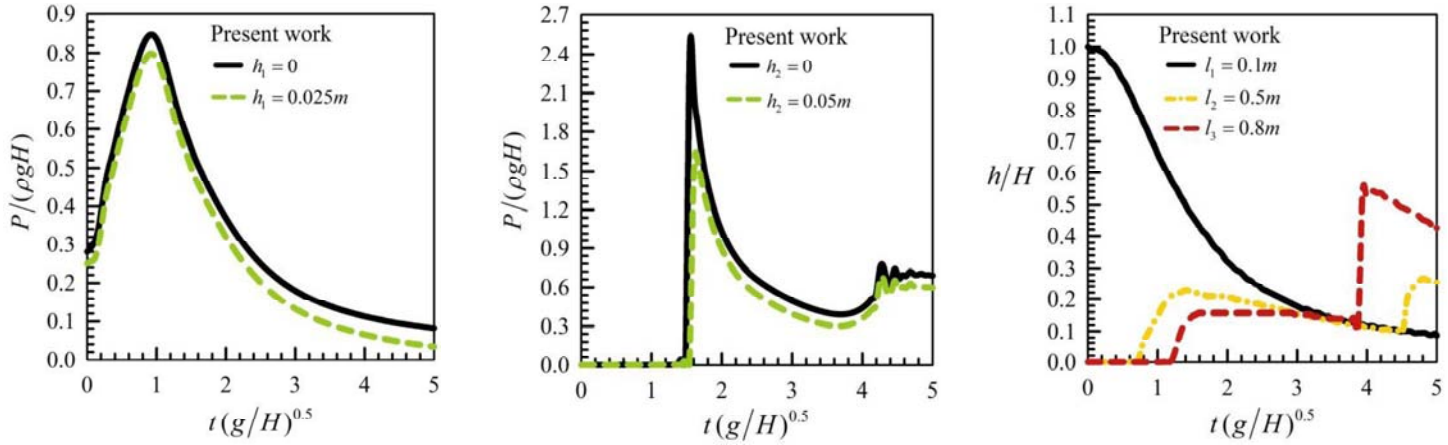

Fig. 6. Comparison of the predicted water column heights, fluid front and pressure variations on the verical walls between present study and numerical works of Xu et al. [94] and Zheng et al. [95] for case 1.

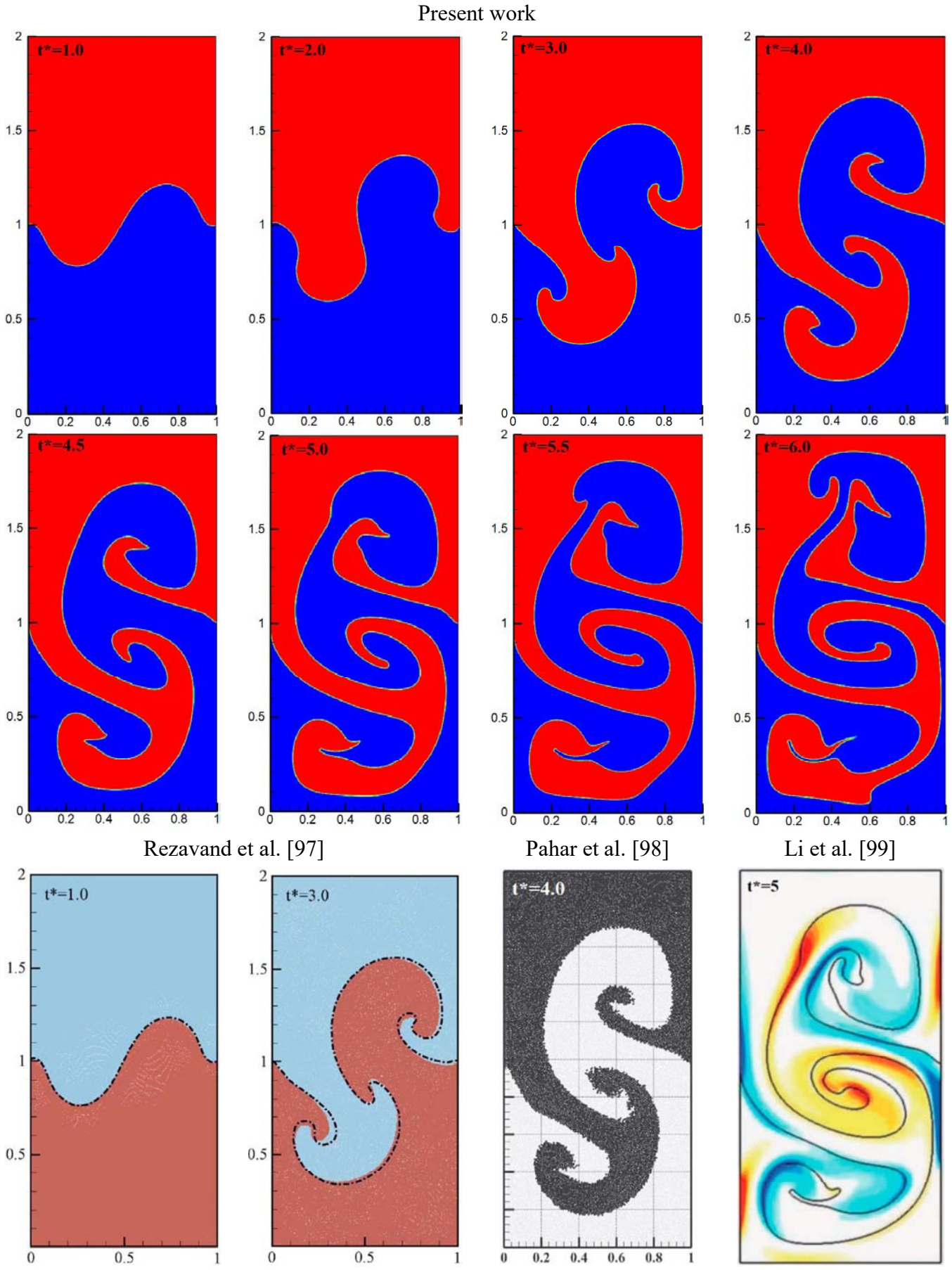

Fig. 7. Comparison of the predicted results with the numerical results of Rezavand et al. [97], Pahar et al. [98] and Li et al. [99] for the case of Rayleigh-Taylor instability problem (case 2) at different time instants.

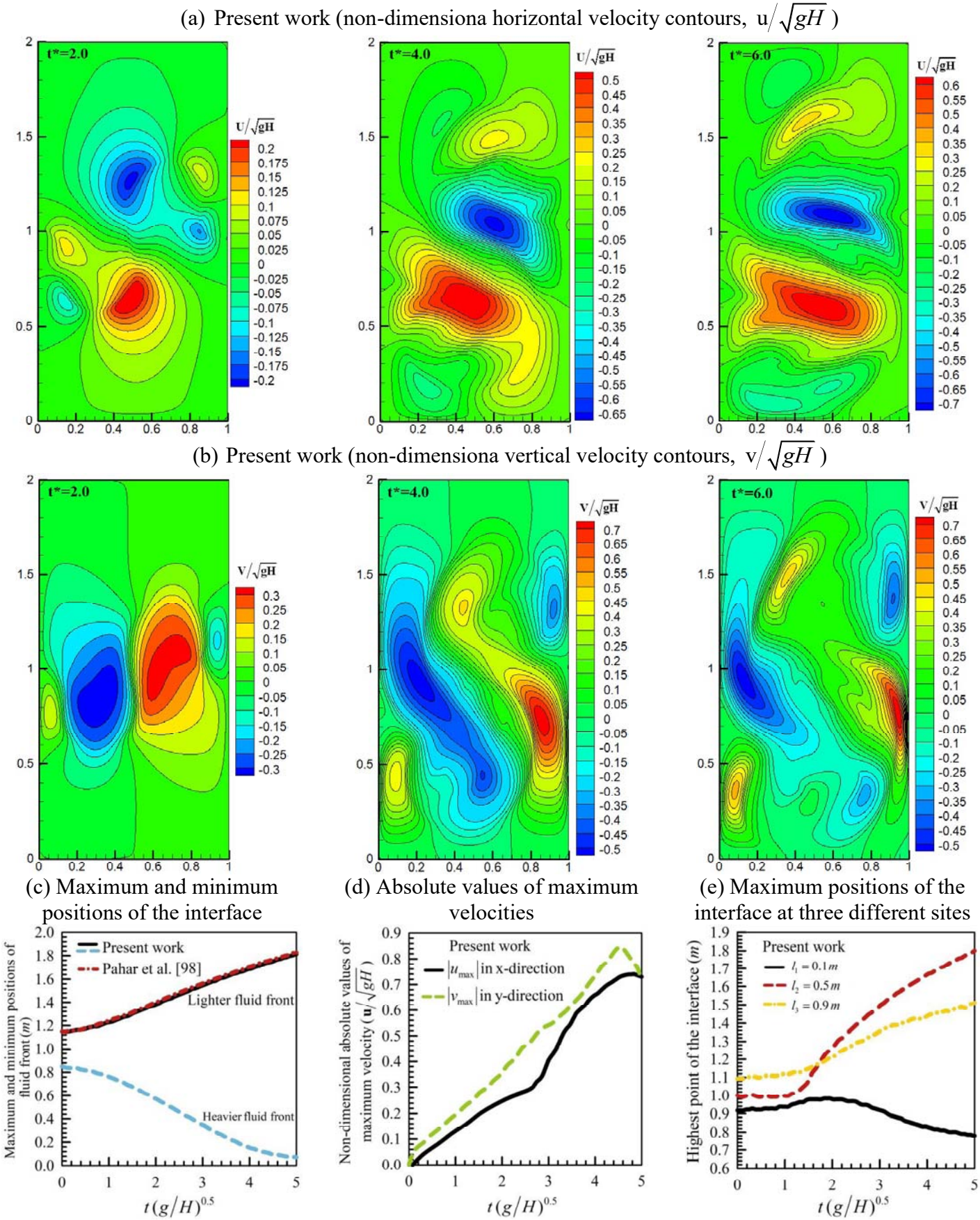

Fig. 8. (a) and (b) Contours of the velocity in the *x* and *y*-directions at different time instants. (c) Maximum and minimum positions of the interface within the computational domain, (d) time history of absolute values of maximum velocity components and (e) maximum positions of the interface at three different vertical sections.

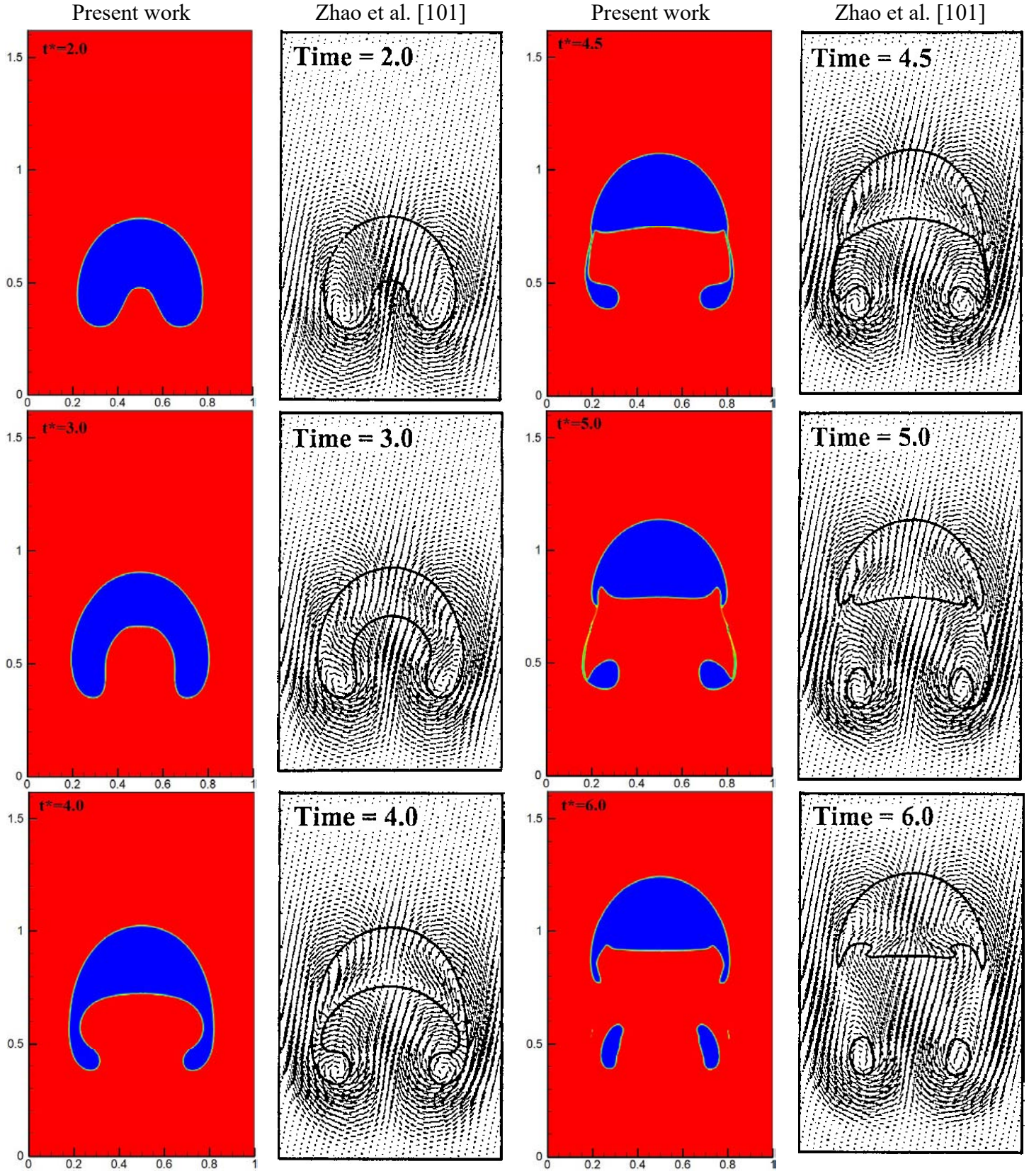

Fig. 9. Comparison of the simulated time evolution of a single rising bubble (case 3) in two-dimensional rectangular enclosure with the numerical results of Zhao et al. [101].

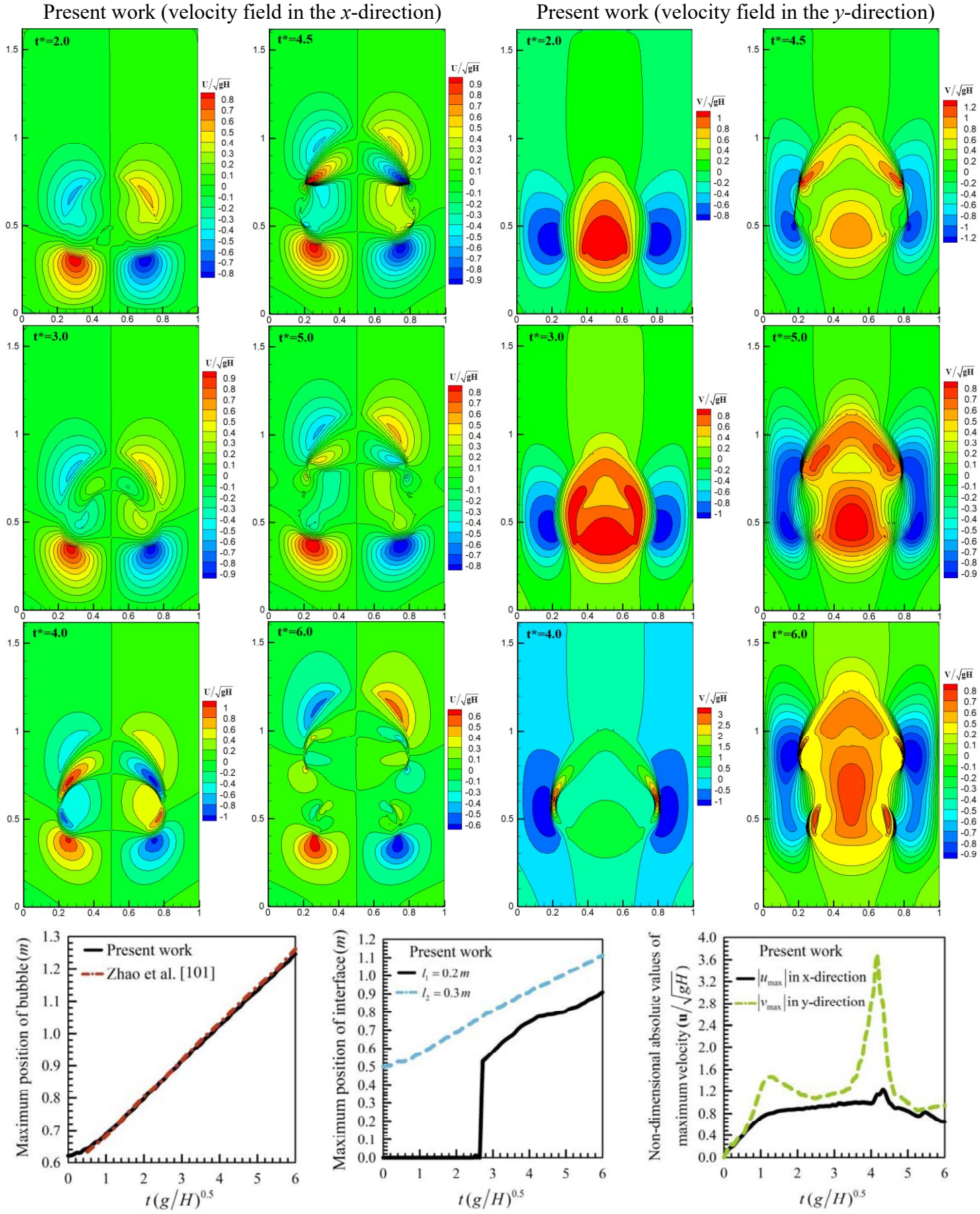

Fig. 10. Contours of the velocity field together with the time history of the bubble front, maximum position of the interface at two different sections, and maximum absolute values of velocity components in case 3.

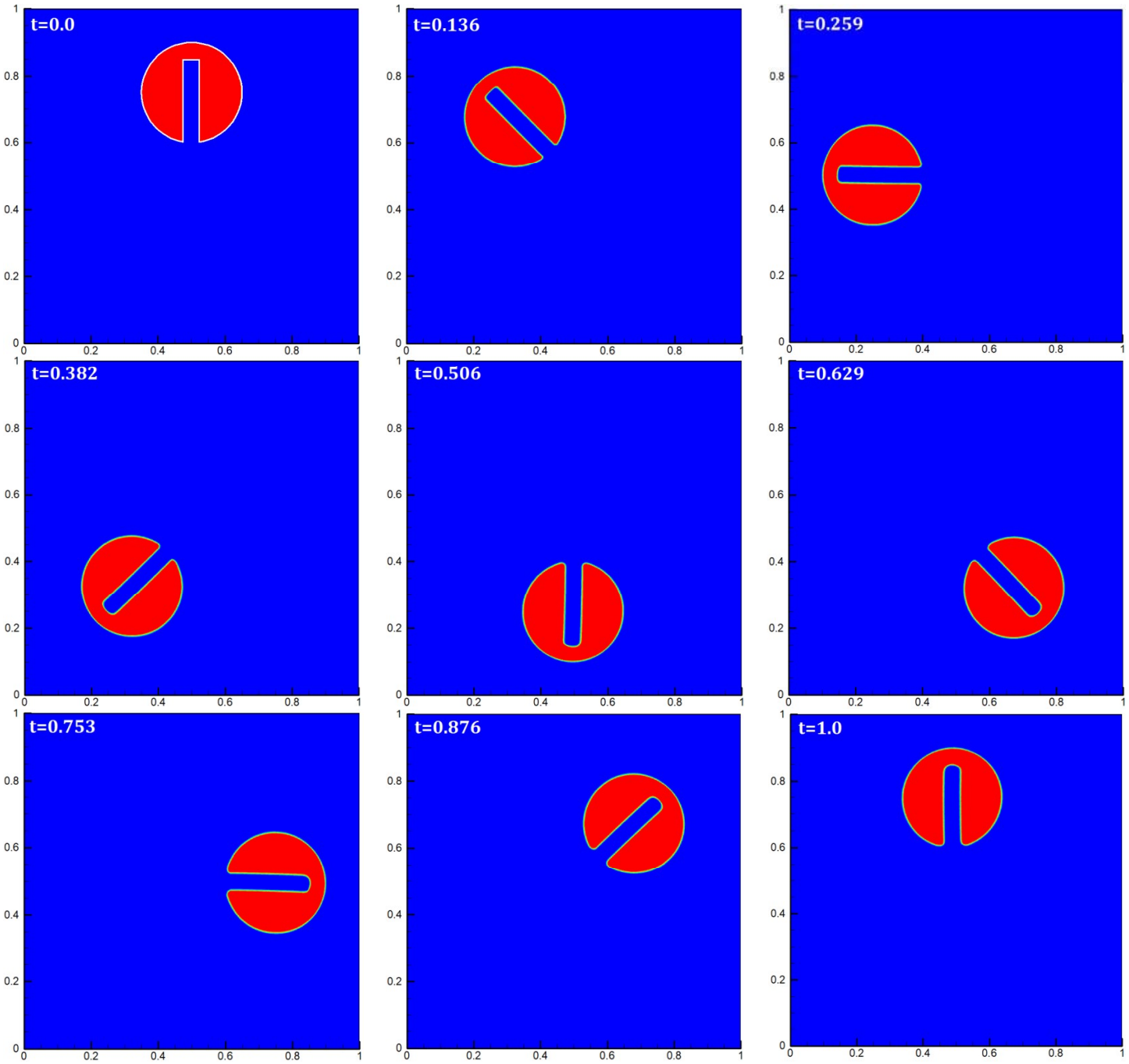

Fig. 11. Comparison between predicted results from the current work with the numerical data of Scardovelli et al. [93] and Owkes et al. [105] for case 4 (Zalesak's disk).

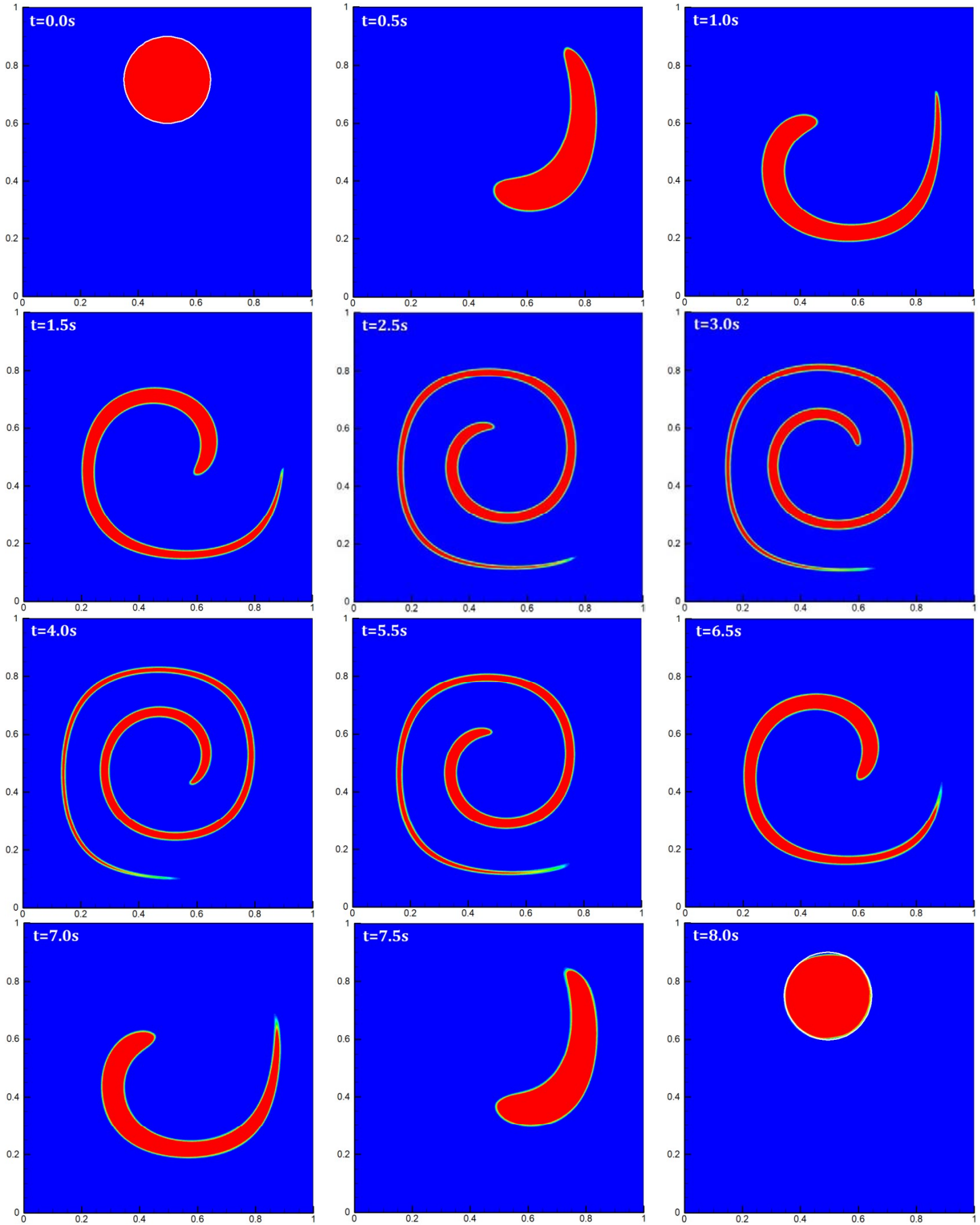

Fig. 12. Transient evolution of deformation of a 2D disk (case 5) in a vortex velocity field predicted by the proposed model at different time instants.

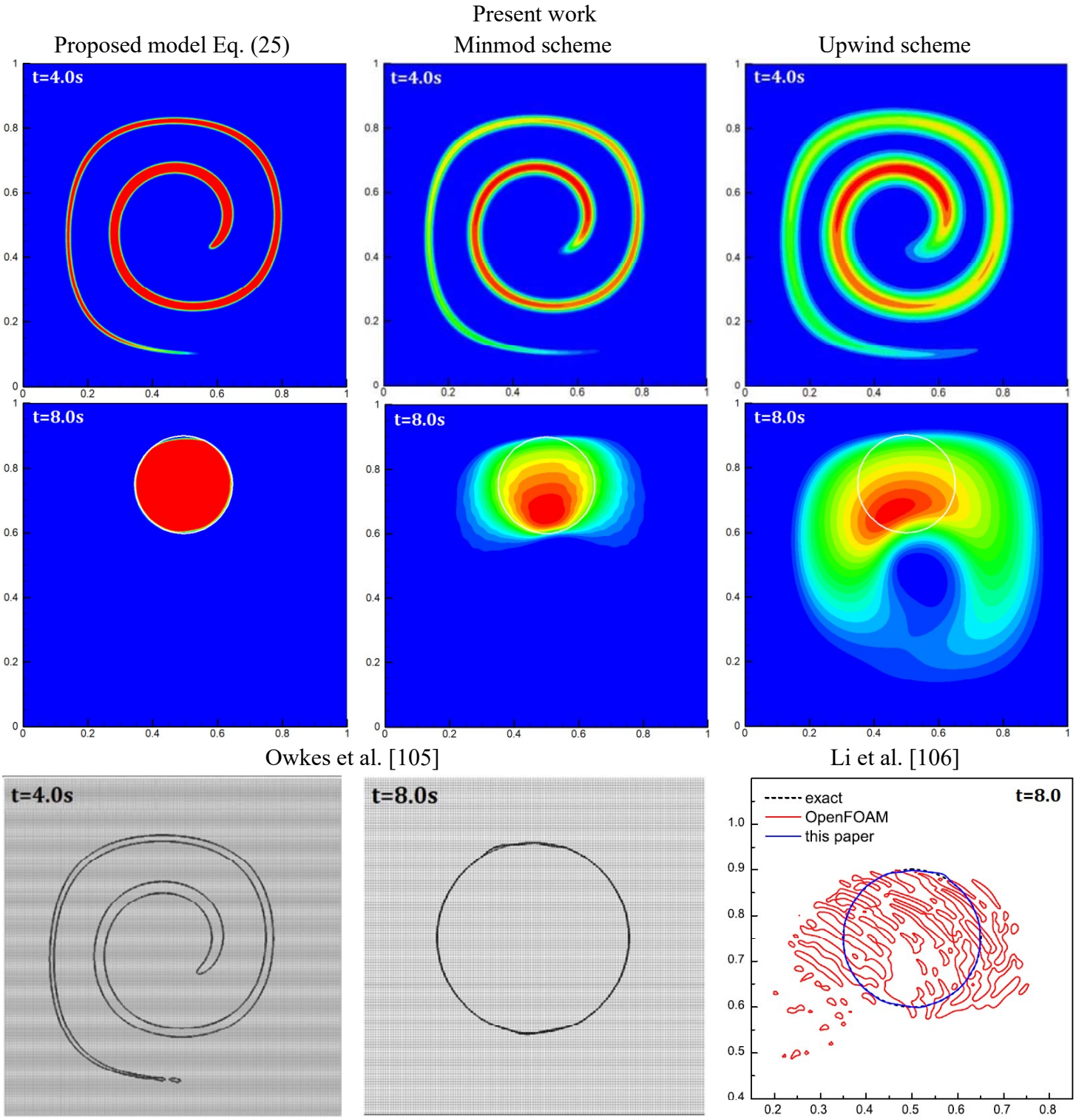

Fig. 13. Qualitative comparison of obtained results for case 5 with numerical data of Owkes et al. [105] Li et al. [106].

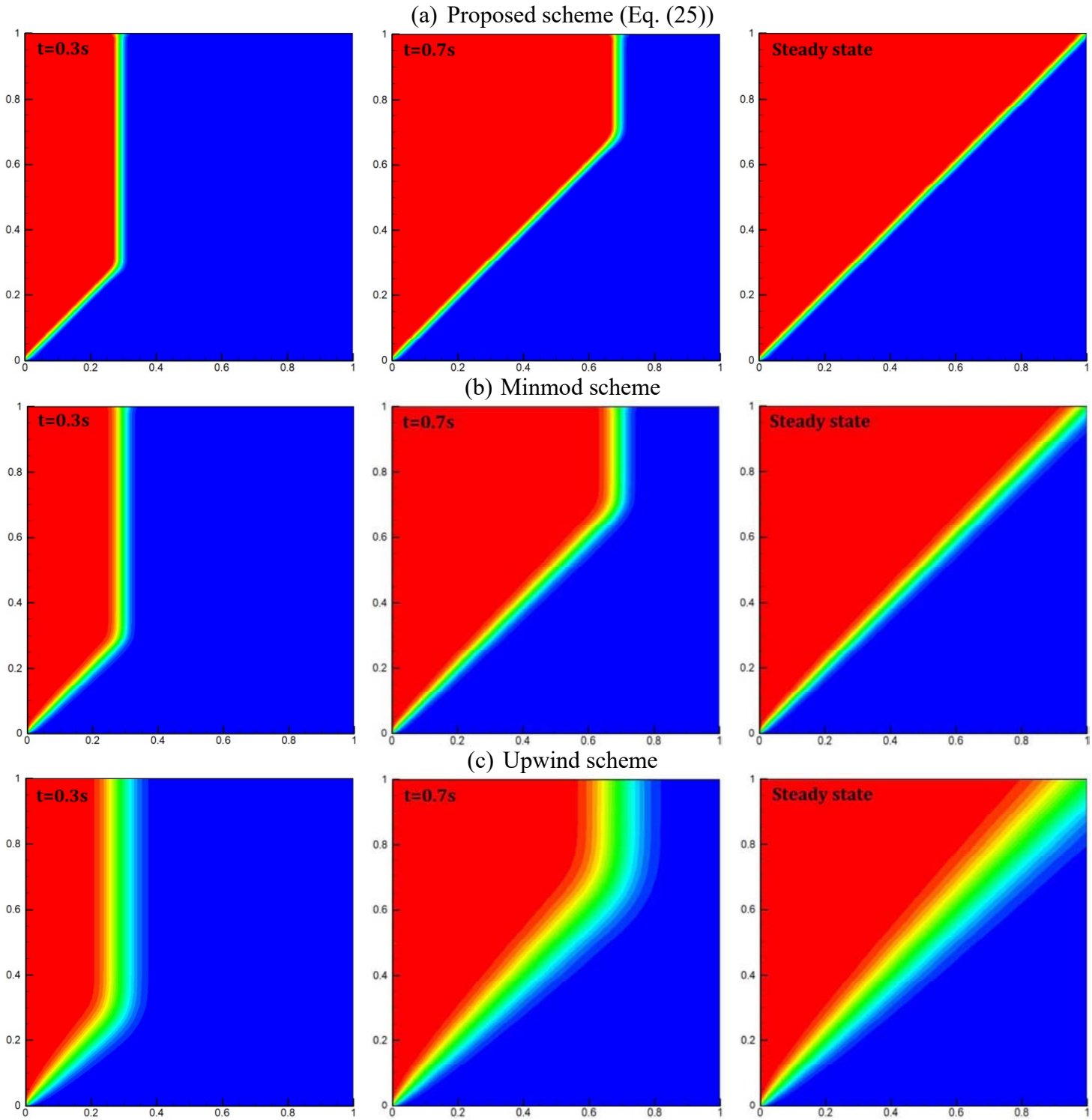

Fig. 14. Simulation of the pure convecttion of a step profile (case 6) using three different convection schemes (a) the newely developed third-order bounded convection scheme (Eq. (25)), (b) Minmod scheme and (c) the classical first-order Upwind scheme.

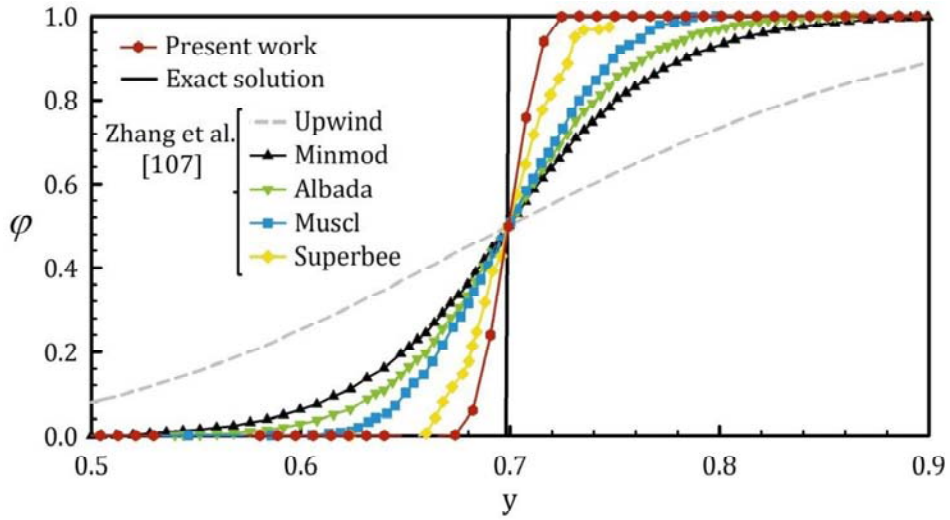

Fig. 15. Comparison of φ profiles along a vertical line ($x = 0.7m$) of the domain at steady state condition predicted by the proposed flux-limiter scheme with five existing TVD convection schemes [107].

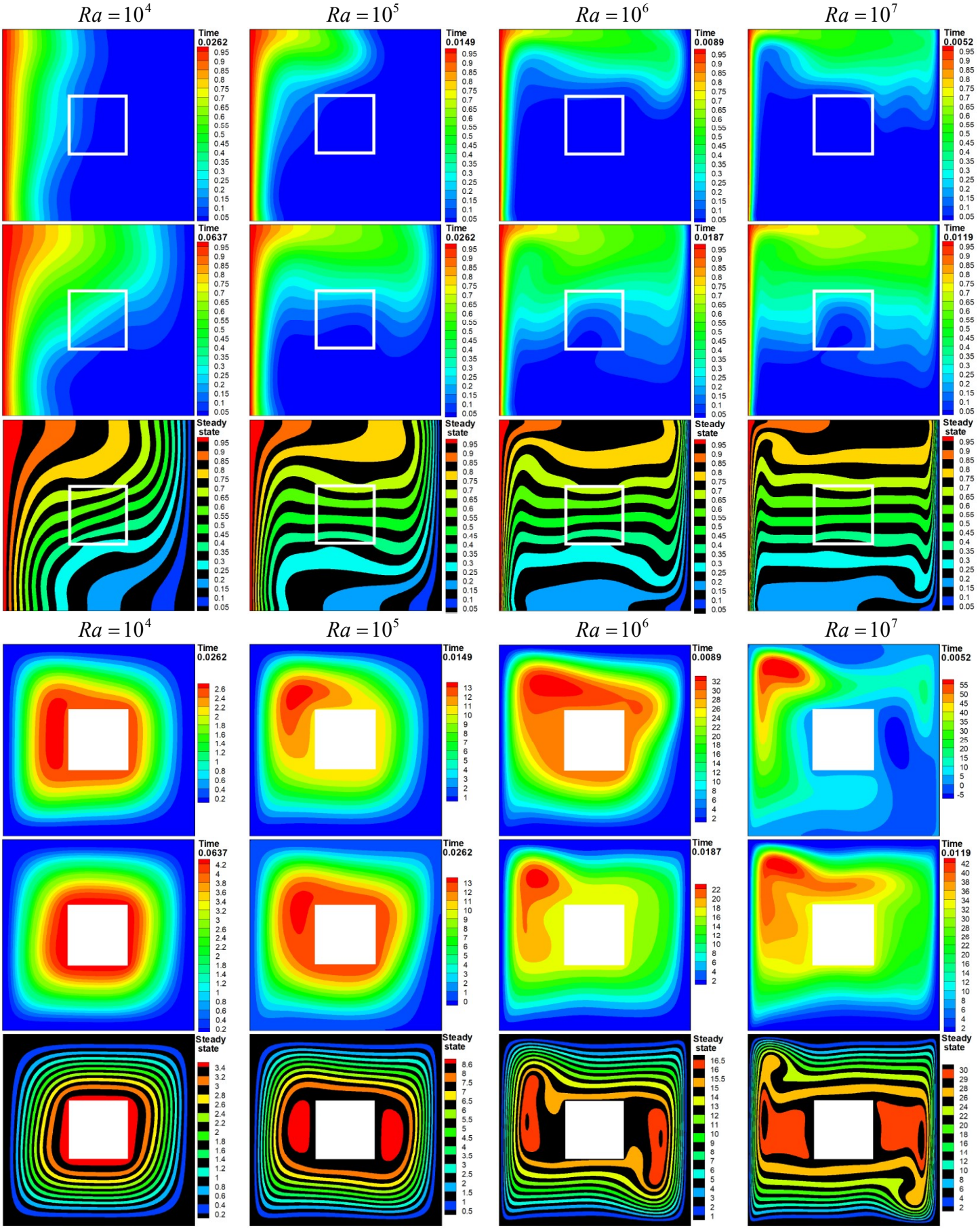

Fig. 16. Transient variation of isotherms and streamlines at different Rayleigh numbers for case 7. $\mathrm{Pr} = 0.71$.

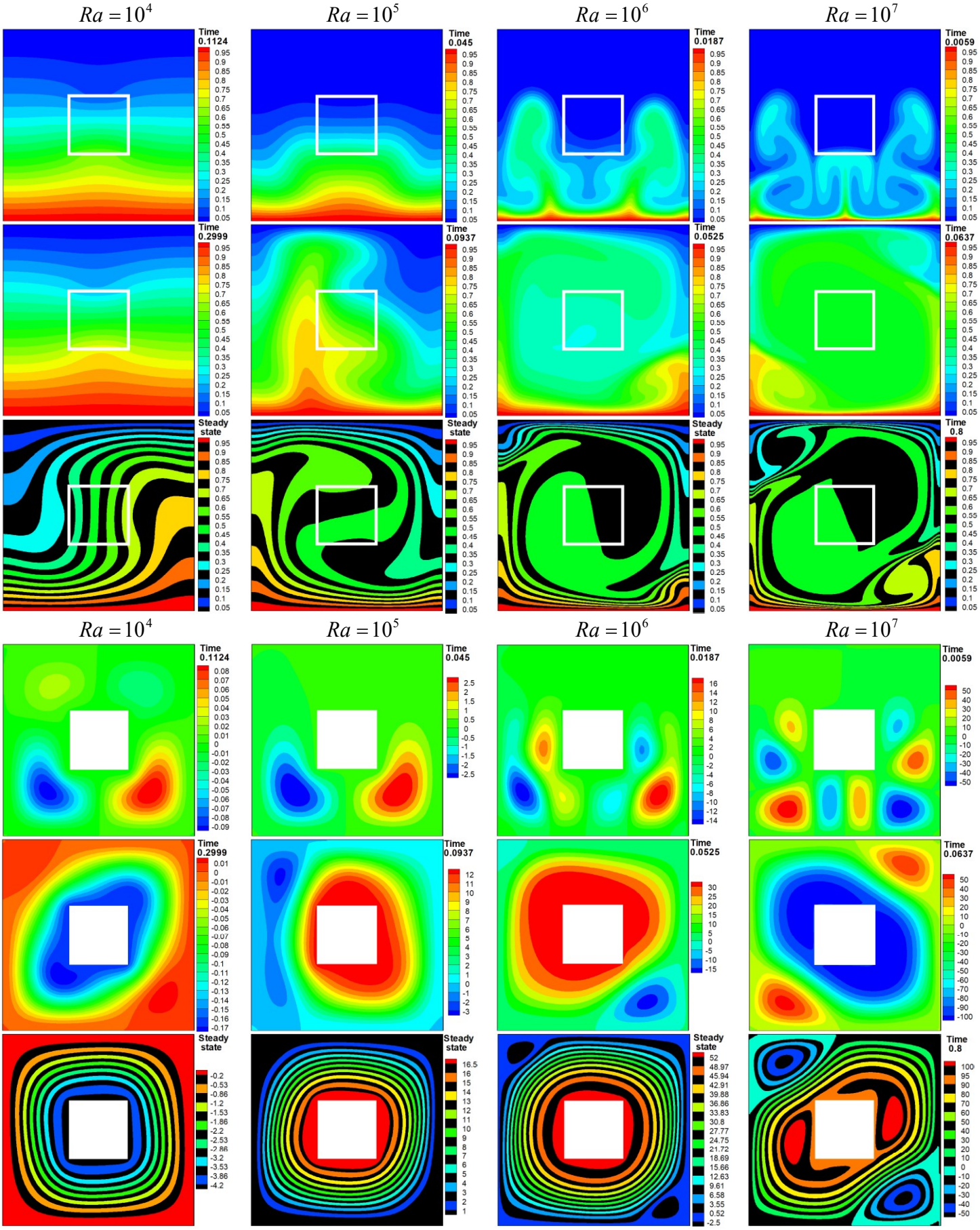

Fig. 17. Transient variation of isotherms and streamlines at different Rayleigh numbers in case 8. $\mathrm{Pr} = 0.71$.

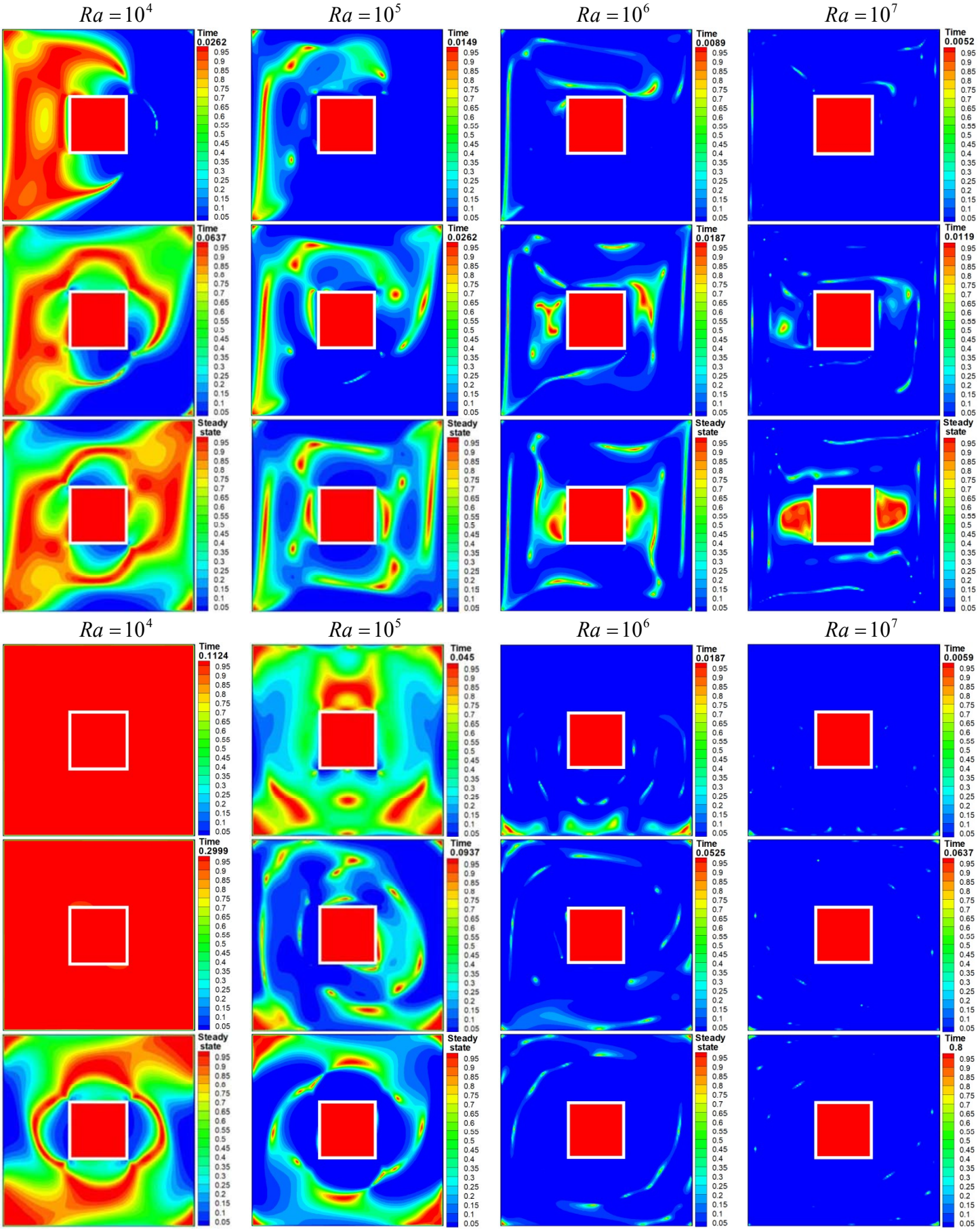

Fig. 18. Transient variation of local Bejan number at different Rayleigh numbers for cases 7 and 8. $\mathrm{Pr} = 0.71$.

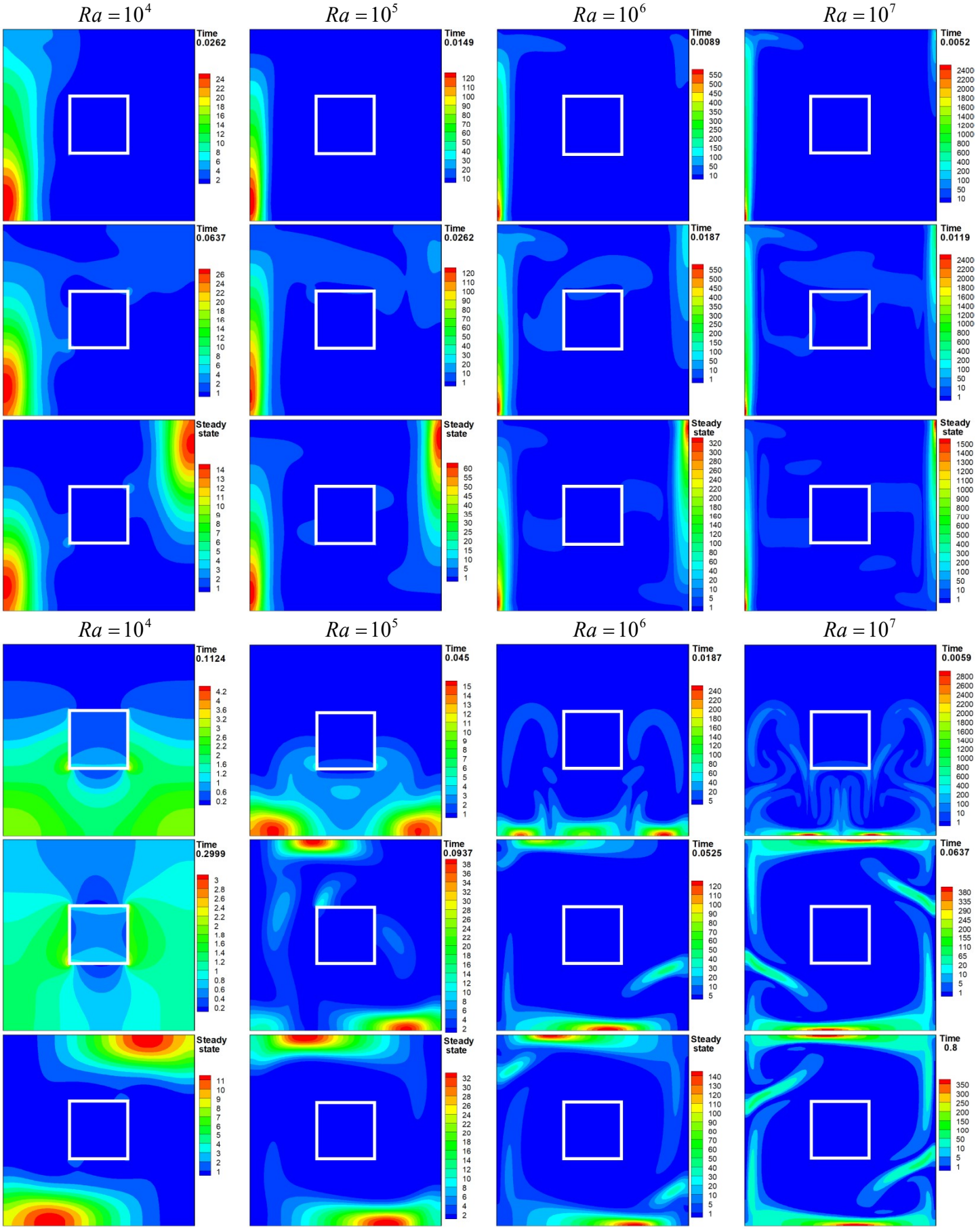

Fig. 19. Transient variation of local entropy generation due to heat transfer irriversibility (S_T) at different Rayleigh numbers for cases 7 and 8. $\mathrm{Pr} = 0.71$.

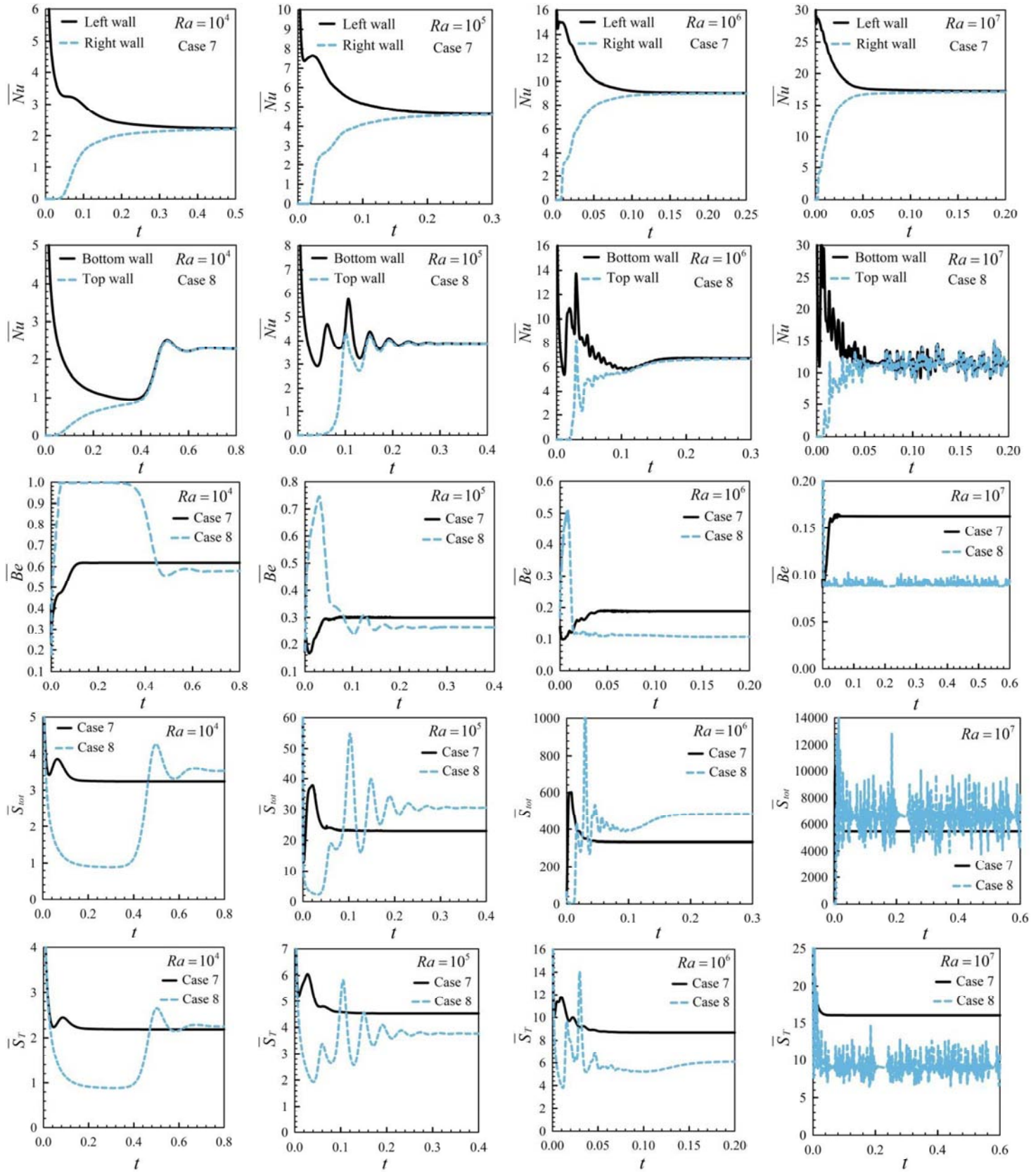

Fig. 20. Transient variations of average Nusselt number ($\overline{Nu}$), total entropy generation ($\overline{S}_{tot}$), average Bejan number ($\overline{Be}$), entropy generation due to thermal ($\overline{S}_T$) and viscous ($\overline{S}_F$) dissipations as function of the dimentional time at different Rayleigh numbers ($10^4 \le Ra \le 10^7$) for cases 7 and 8. ($\Pr = 0.71, L = 0.3H$, $K_r = 0.2$)

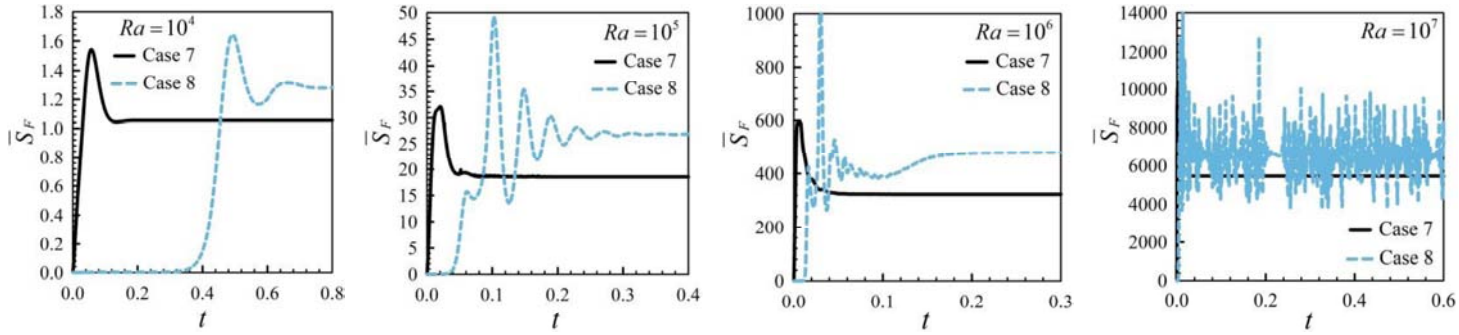

Fig. 20. Continued.

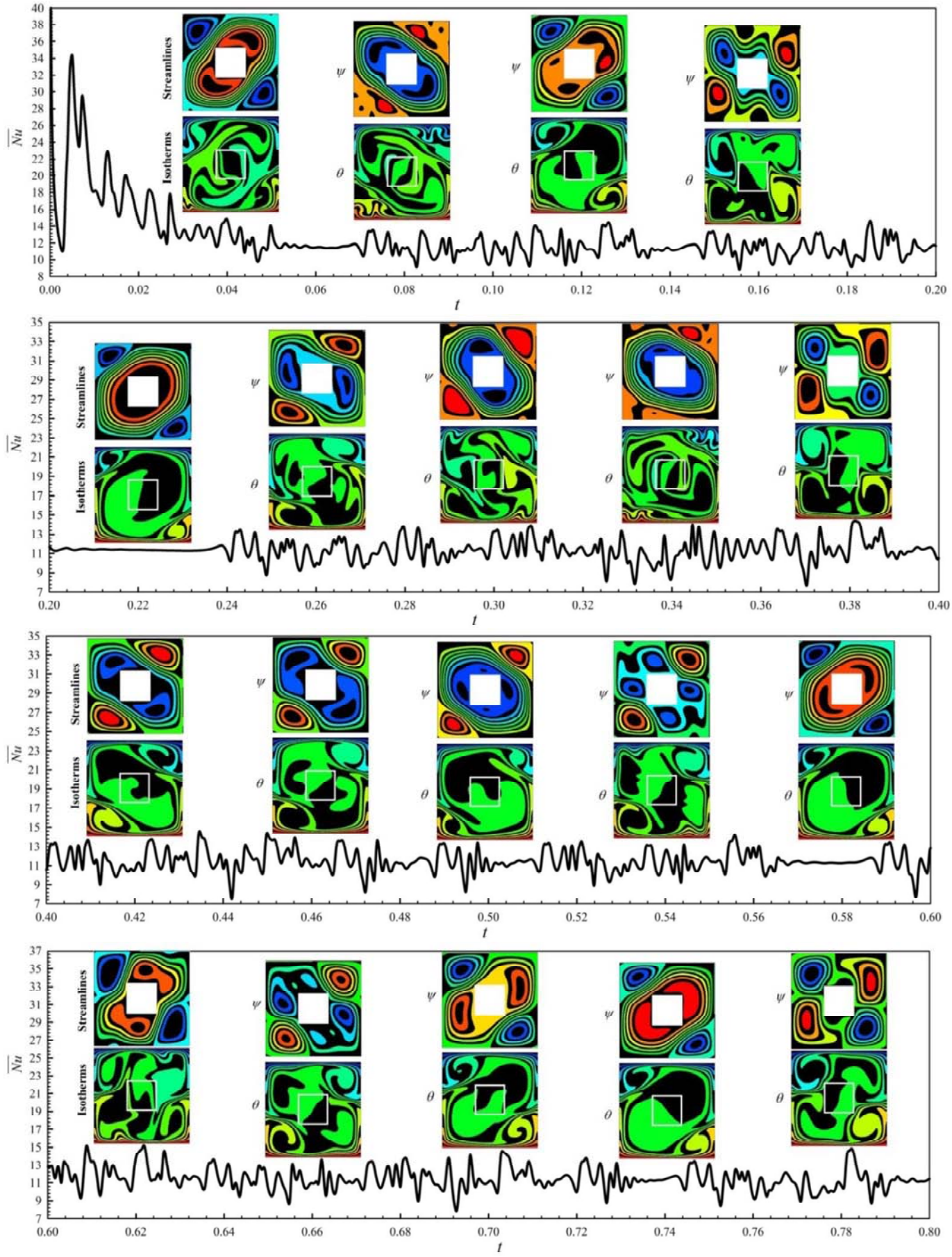

Fig. 21. Zoomed-in view of average Nusselt number with associated snapshots of isotherms and streamlines at Ra=10^7 for case 8 (conjugate Rayleigh-Bénard convection).

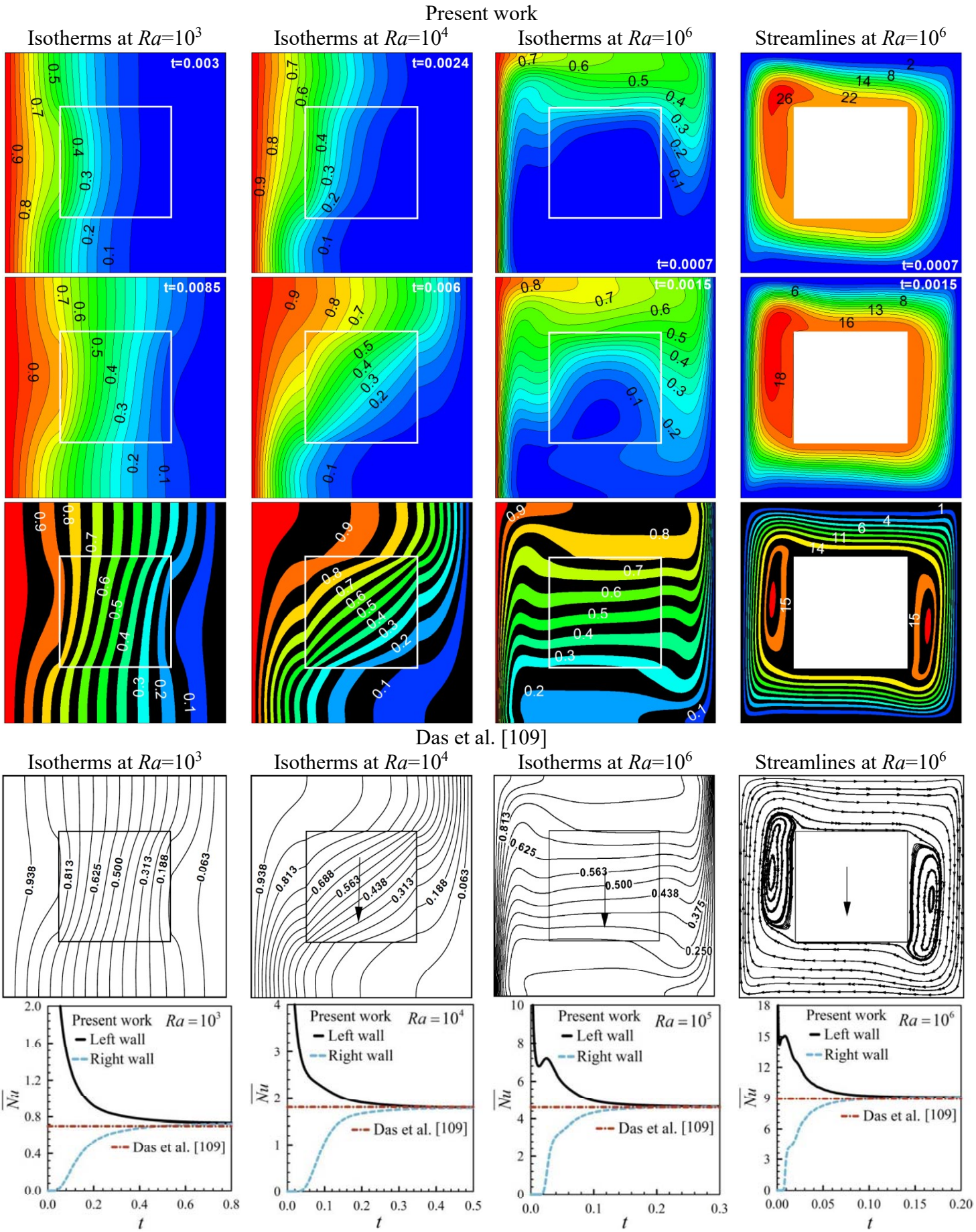

Fig. 22. Comparison of predicted results with the numerical data of Das et al. [109] for the case of Differentially Heated Cavity with an internal conductive body. K_r=0.2, Pr=0.71 and L=0.5H.

Table 1. Determination of the interface orientation and fluid position

variation rate of the color function in the *x*-direction	variation rate of the color function in the *y*-direction	Absolute value of the interface slop	Possible case of interface orientation
$n_x > 0$	$n_y < 0$	$\lvert m_i \rvert > 1$	A1
$n_x > 0$	$n_y < 0$	$\lvert m_i \rvert \le 1$	A2
$n_x > 0$	$n_y > 0$	$\lvert m_i \rvert > 1$	B1
$n_x > 0$	$n_y > 0$	$\lvert m_i \rvert \le 1$	B2
$n_x < 0$	$n_y > 0$	$\lvert m_i \rvert > 1$	C1
$n_x < 0$	$n_y > 0$	$\lvert m_i \rvert \le 1$	C2
$n_x < 0$	$n_y < 0$	$\lvert m_i \rvert > 1$	D1
$n_x < 0$	$n_y < 0$	$\lvert m_i \rvert \le 1$	D2
$n_x > 0$	$n_y \approx 0$	$\lvert m_i \rvert > 10^{20}$	V1
$n_x < 0$	$n_y \approx 0$	$\lvert m_i \rvert > 10^{20}$	V2
$n_x \approx 0$	$n_y < 0$	$\lvert m_i \rvert < 10^{-20}$	H1
$n_x \approx 0$	$n_y > 0$	$\lvert m_i \rvert < 10^{-20}$	H2

Table. 2. Zalesak's problem (case 4): comparison of accumulated error.

Advection algorithms	Error ($E = \sum_{i=1,j=1}^{N} \left\|\varphi_{i,j} - \bar{\varphi}_{i,j}\right\| \Big/ \sum_{i=1,j=1}^{N} \bar{\varphi}_{i,j}$)
Present model/Eulerian	5.72×10^{-3}
gVoFoam/Eulerian [63]	1.36×10^{-2}
interFoam/Eulerian [63]	6.61×10^{-2}
OpenFoam®/Eulerian [106]	7.03×10^{-2}
Puckett/Stream/Eulerian [93]	1.00×10^{-2}
Quadratic fit/Lagrangian [93]	5.47×10^{-3}
Quadratic fit+continuity/Lagrangian [93]	4.16×10^{-3}

Table. 3. Deformation of a 2D disk problem (case 5): comparison of accumulated error.

Advection algorithms	Error ($E = \sum_{i=1,j=1}^{N} (\varphi_{i,j} - \bar{\varphi}_{i,j}) \Big/ \sum_{i=1,j=1}^{N} \bar{\varphi}_{i,j}$)
Present model/Eulerian	6.13×10^{-4}
gVoFoam/Eulerian [63]	2.95×10^{-3}
interFoam/Eulerian [63]	5.58×10^{-2}

Table 4. Variations of $\overline{Nu}$ as a function of the grid size in cases 7 and 8 at low and high Rayleigh numbers.

Number of grids (Case 7)							
Ra	39×39	59×59	79×79	99×99	119×119	139×139	159×159
10^4	2.1675	2.1832	2.1966	2.2051	2.2134	2.2168	2.2177
10^7	17.1438	17.1944	17.2132	17.2225	17.2286	17.2307	17.2319
Number of grids (Case 8)							
Ra	39×39	59×59	79×79	99×99	119×119	139×139	159×159
10^4	2.2505	2.2601	2.2692	2.2784	2.2825	2.2846	2.2853
10^7	11.1563	11.3219	11.4134	11.4308	11.4392	11.4406	11.4417

Table. 5. The effects of the Rayleigh number on the flow intensity, average Nusselt number and entropy generation rate for cases 7 and 8 (steady-state condition). Note that, case 8 never reaches a steady state condition at $\boldsymbol{Ra}=\mathbf{10}^{\mathbf{7}}$.

Case 7										
Ra	$\overline{Nu}$	$\lvert U_{\max}\rvert$	$\lvert \psi_{\max}\rvert$	$\overline{Be}$	$\overline{S}_{tot}$	$S_{tot,\max}$	$\overline{S}_{T}$	$S_{T,\max}$	$\overline{S}_{F}$	$S_{F,\max}$
10^4	2.217	15.217	3.459	0.618	3.240	25.463	2.185	14.503	1.054	14.914
10^5	4.624	40.902	8.849	0.299	23.061	629.852	4.523	63.850	18.538	590.402
10^6	9.023	120.314	16.537	0.188	332.456	16362.64	8.687	325.676	323.768	16227.41
10^7	17.231	350.577	30.429	0.163	5465.67	373316.035	16.027	1553.121	5449.64	372930.16
Case 8										
Ra	$\overline{Nu}$	$\lvert U_{\max}\rvert$	$\lvert \psi_{\max}\rvert$	$\overline{Be}$	$\overline{S}_{tot}$	$S_{tot,\max}$	$\overline{S}_{T}$	$S_{T,\max}$	$\overline{S}_{F}$	$S_{F,\max}$
10^4	2.285	19.369	4.276	0.579	3.543	17.587	2.257	11.743	1.286	16.695
10^5	3.853	77.987	17.062	0.265	30.091	471.496	3.740	34.435	26.351	471.378
10^6	6.595	273.305	52.611	0.106	473.863	15582.646	6.027	147.585	467.836	15582.543
$\mathbf{10^7}$	11.441	785.986	105.237	0.088	6826.085	329040.76	9.196	398.455	6816.88	329040.51

Declaration of interests

☒ The authors declare that they have no known competing financial interests or personal relationships that could have appeared to influence the work reported in this paper.

☒The authors declare the following financial interests/personal relationships which may be considered as potential competing interests:

This work is financially supported by the Merit scholarship program for foreign students (PBEEE) of the Ministère de l'Éducation et de l'Enseignement supérieur du Québec (MEES) (Grant No. 263222), (Programme V1-Groupe: G2-20431).

Conflict of interest

The author declared that there is no conflict of interest.